Università degli Studi di Ferrara

DOTTORATO DI RICERCA IN
SCIENZE DELL'INGEGNERIA

CICLO XXIV

COORDINATORE Prof. Stefano Trillo

FAULT DETECTION IN HEAVY DUTY WHEELS BY ADVANCED VIBRATION PROCESSING TECHNIQUES AND NUMERICAL MODELLING

Settore Scientifico Disciplinare ING-IND / 13

Dottorando
Dott. Malagò Marco

Tutore
Prof. Dalpiaz Giorgio

Anni 2009/2011

Università degli Studi di Ferrara
Engineering Department in Ferrara

Dottorato di Ricerca in Scienze dell' Ingegneria
XXIV ciclo

Doctoral Program: Engineering
Curriculum: Industrial Engineering
Branch of study: Mechanics of Machines

Title: Fault detection in heavy duty wheels by advanced vibration processing techniques and numerical modelling

Author: Ing. Marco Malago'
Supervisor: Prof. Giorgio Dalpiaz
Printed: April 2012

PhD Coordinator
Prof. Stefano Trillo Università degli Studi di Ferrara

PhD Jury
Prof. Stefano Piva Università degli Studi di Ferrara, Italy
Prof. Prof Alessandro Rivola Università di Bologna
Prof Alessandro Corsini Dipartimento di Ingegneria Meccanica e Aerospaziale , Università di Roma 'La Sapienza'
Prof Timothy Waters Institute of Sound and Vibration Research (ISVR), University of Southampton

PhD International referees

Prof Timothy Waters Institute of Sound and Vibration Research (ISVR), University of Southampton

Prof David Moens, Department of Mechanical Engineering - K.U.Leuven, Leuven, Belgium,

Final exam

2012 April, 3rd

Contents

List of Figures

List of Tables

Chapter 1

Introduction

1.1 What is the thesis about?

This thesis deals with condition monitoring and diagnostics in heavy-duty wheels by means of vibration signature techniques and numerical modelling.

Different questions are posed:

- Is it possible to experimentally detect the presence of missing adherence defects and rust in the tread-hub interface?
- Is it possible to diagnose the nature of the defect?
- How can these defects cause a variation in the vibratory level?
- Do the wheel dynamics influence the measured response?
- Which are the characteristics of a multibody model able to reproduce a faulty wheel vibratory level?

The main thesis objectives are:

- defining a monitoring and diagnostics algorithm to be used in a work station at the end of the production line;
- realizing a multibody model for diagnostics purposes able to give a physical explanation of the defect effects.

1.2 Background

The thesis deals with the design of a monitoring and diagnostics algorithm based on vibrational signal to be applied at the end of the production line on wheels used for material handling in civil and industrial area, defined in the following as “heavy duty wheels”. These wheels are produced by the company Tellure Rota S.p.a in Formigine, Modena, Italy [1].

The company production philosophy is based on the “Lean production” approach, i.e. on an industrial philosophy inspired to Toyota production system, whose core concept is the production of a flow of activities originated by the Customer. The only activities to enforce are those closely related to accomplish what the customer requires at a specific time. In accordance with these principles, Tellure Rota production system is based on constant flows to be graduated, depending on Customers requirements, to always guarantee the quickest lead time.

The achievement of these objectives is accompanied by the proper control of the product quality made primarily through various highly automated production stages. This approach significantly reduces the presence of anomalies or the occurrence of defects due to operator actions not correct or simply not repeatable and controllable. However, due the wide variety of components produced, it may happen that certain stages of production can only be realized through an operator. Indeed, various wheel topology in terms of material, size and support are produced. Each produced wheel consists of the following components: the tread, the covering, the center, the bore and the rolling action, as depicted in Figure 1.1. Depending on the construction method and on the material, different processing phases are adopted.

The heavy duty wheel object of the analysis is a wheel composed by a polyurethane tread and a cast iron hub. For this product, the most delicate production phase is represented by the manual handling of the wheel component for the application of the adhesive layer, required to create a solid connection between tread and hub. A pollution of the interface or the presence of anoma-

lies in the hub such as rust, can cause a separation of the tread during working phase, with unpleasant consequences for the operator.

In order to avoid the selling of components presenting this kind of defects, a monitoring and diagnostics algorithm is required.

The algorithm has to :

- be applied in a test bench at the end of the the production line;
- give threshold pass-fail barriers, obtained through adapt processing techniques (monitoring skill);
- be able to recognize the type of anomaly (diagnostics skill);
- be consistent;
- be fast, i.e. it has to be applied to the maximum number of components without increasing significantly the production times.

Condition monitoring and fault detection are generally referred to as the evaluation of the state of a system through the selection of measurable parameters, which will change as the state of health of the system. On the other hand, fault diagnosis is a more rigorous action which requires the identification of the component that causes the deviation from the normal state [2–6].

Condition monitoring and diagnostics can be achieved by using different kinds of data as input (e.g. pressure, temperature, torque), nevertheless the vibration analysis can be considered extremely widespread due to the fact that mechanical faults in machines often show their presence through abnormal vibration signals. As a consequence, the purpose of condition monitoring is to use information extracted from the system signature in order to detect faults or to define its state of health: a change in the vibration signature not only indicates a change in the system conditions, but also directly points to the source of the signal alteration. Generally speaking, fault detection and diagnosis in mechanical systems can be carried out by using different strategies: processing experimental signals associated with system dynamic models.

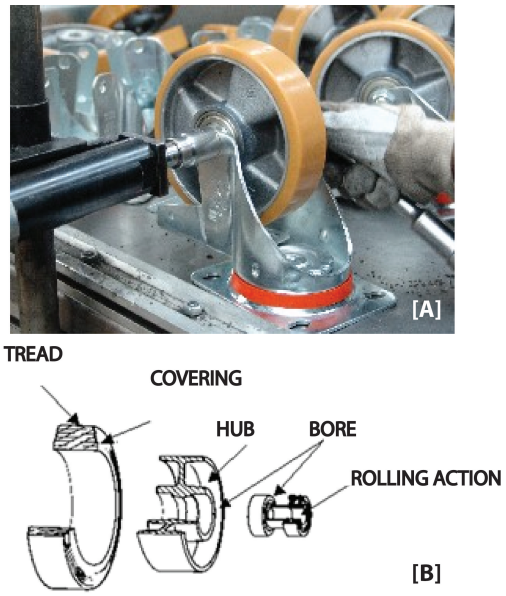

Figure 1.1: Heavy duty wheel: main structure [A] and components [B]

1.2.1 Monitoring and diagnostics based on signal processing techniques

The most used strategy is to adopt signal processing techniques on experimental data in order to obtain values, features or maps that can be used to detect the presence of defects. Many researchers have proposed the application of different vibration analysis techniques [2–6].

In general, a condition monitoring process based on experimental data is achieved by different steps: firstly a relevant number of healthy and faulty components are realized and analyzed in order to detect the most suitable sensor, the optimal position and the operational test able to emphasize the component changes. The subsequent step consists of measuring experimental data. Generally, the acquired signals need to be processed through appropriate techniques in order to extract the maximum number of information.

Eventually well suited indicators/coefficients are applied to the processed sig-

nal, objectifying the anomaly presences and defining pass-fail reference values. In this work, Synchronous Average (SA), Cyclostationary analysis and time-frequency distribution techniques have been applied. Concerning the time-domain analysis, the Synchronous Average of the vibration signal allows to attenuate the periodic events not synchronous with the rotating component of interest and to reduce the background noise [7, 8]. The resulting signal average is the ensemble average of the angle domain signal, synchronously sampled with respect to the component rotation. The main advantage of SA is to extract from a complex vibration signal, its deterministic part, i.e. the event that is repeated periodically with the rotation of interest.

A further advanced tool adopted for investigating the relationships between spectral components is the cyclostationary theory [6, 9]. More specifically, a signal is cyclostationary if some of its statistics present periodicities. As previously described, averaging can make it possible to extract the deterministic part of the signal. If the signal obtained after subtracting this deterministic part from the synchronized signal does not exhibit cyclostationarity, the signal is said to be cyclostationary at an order '1'. In general terms, a signal is cyclostationary at an order 'n' if its statistical properties at order 'n' are periodic.

If local faults produce impacts the signals have to be considered as non-stationary and characterized by a transient vibration signal. Time-frequency analysis such as continuous wavelet transform (CWT) [10–12] has been used for the characterization of short-duration transient events and to detect localized defects. This processing technique has the property of detecting sudden changes or transients in non-stationary signals through the application of variable time windows, in order to achieve fine time resolution at high frequencies and fine frequency resolution at low frequencies.

Due to the relative low computational effort needed by these processing techniques, it is possible to conceive a monitoring-diagnosis algorithm based on indicators extracted from these techniques.

1.2.2 Using system models in monitoring and diagnostics

In the context of monitoring and diagnostics, system modelling is generally realized in order to:

- estimate the influence of different component dimensions and materials on the vibration response [13];
- evaluate the defect nature and its effect on the vibration response (diagnostics purposes) [14, 15];
- produce simulation models, in which faults can be implemented under different operating conditions rather than waiting for these to occur naturally, or alternatively having them realized in a laboratory. Such fault simulation can be very valuable in machine diagnostics and prognostics in order to produce signals with well-defined characteristics [16, 17].

Generally, models have to be based on parameters estimated through dedicated experimental tests and have to present reasonable computation costs.

Different modelling approaches can be adopted:

- analytical model [16–19];
- finite element model [20, 21];
- multibody model [22, 23]

Each model has to be validated by fitting the numerical results with data collected experimentally. This information mainly regards the system frequency response function, i.e. natural frequencies and mode shapes. Indeed, in complex components a good understanding of the transfer functions between vibration sources and transducers can be complicated. Generally, vibration is picked up from the machine casing while the vibration sources originate from the moving mechanism, whose dynamic behaviour is the result of the interaction of numerous factors: kinematic and dynamic properties of the mechanism itself, external forces, parametric excitations, friction, backlash effects in joints and

faults, etc... Forces are then transmitted to the casing and excite the support structure, whose response is affected by its own dynamic properties too. The effect of the transfer function between mechanism components and casing may be very important [2].

Experimental identification of structural dynamics is usually based on the modal analysis approach, i.e. considering the measured response as the superposition of the system natural modes, differently excited by the input force that acts on the system. In the classical modal parameter estimation, known as Experimental modal analysis (EMA), the baseline data which are processed are frequency response functions measured under laboratory conditions [24, 25].

However, in many applications, the real operating conditions may differ significantly from those applied during the modal test. To this purpose, a system identification technique has been developed which is able to identify the modal model from the structure under operational conditions using output-only data. This technique, referred to as operational modal analysis (OMA) or output-only modal analysis, takes advantage of ambient excitation. This allows the identification of more realistic modal models for in-operation structures [26, 27].

If the system under analysis shows linear behaviour in both laboratory and operational conditions, it is possible to determine its dynamic properties using the previously described modal analysis techniques. However, linearity is an exception in real systems and non-linearity is the normality [28]. Totally unexpected phenomena sometimes occur, phenomena that are not predicted or even hinted at by linear theory. Typical sources of nonlinearities are:

- geometric nonlinearity when a structure undergoes displacement and arises from potential energy;

- inertia nonlinearity taking its source in the kinetic energy of the system;

- nonlinear material behaviour observed when constitutive laws relating stresses and strains are nonlinear (hysteretic effect);

- boundary conditions or certain non linear body forces.

In this thesis, characterized by the presence of a wheel tread composed of polyurethane viscoelastic material, non-linear material behaviour will be analyzed in detail [29, 30].

Young's Modulus and damping properties in the case of viscoelastic materials are dependent on different factors, such as static load, temperature, deformation amplitude and frequency [31–34, 34–38]. This multiple dependency inevitably affects the modal analysis results. Nevertheless, since non-linearity is still largely non understood, the tendency is to study the system under the linearity hypothesis. In order to assume this hypothesis without introducing several inaccuracies in the results, it is necessary to have previously studied the material non-linearity level. The material has to be studied, statically and dynamically, extracting information about both elastic and damping properties at different conditions of preload, temperature, frequency and deformation. The result of this analysis consists of the evaluation of the so defined "material characterization matrix", i.e. a matrix containing the material complex moduli, at a various preload and dynamic amplitudes.

The complex modulus concept is a powerful, widely used tool for characterising the dynamic elastic and damping properties in the frequency domain. Knowledge of the complex moduli, their components (the dynamic modulus, the loss modulus and the loss factor) and their frequency dependencies have been of interest to scientists and engineers for a long time [34, 37].

1.3 Research objectives

The first part of the research aims at defining a monitoring and diagnostics algorithm able to recognize possible anomalies on heavy-duty wheels at the end of the production line. The algorithm has to be fast and efficient in order to be applied to a large number of components.

This work presents the application of different signal processing techniques on experimental data coming from a large number of components realized ad hoc with different known defects. Moreover, the most appropriate sensor, its

position and the operational conditions that best highlights the defect presence needs to be determined.

The second part of the research concerns the realization of a multibody model of the component in rotation on a moving drum. The model aims at reproducing the phenomena that cause a variation of the vibratory level in case of defect, representing a powerful instrument for monitoring and diagnostics purposes. Different analyses have to be covered to reach this goal. First of all, wheel dynamic characterization is required in order to determine its dynamic effect on the measured response. Due to the viscoelastic nature of the tread material, this activity needs accurate research. Subsequently, a complete explanation of the defect manifestation and of the operational condition influences on the acquired signal is reported.

The main objective of this second activity phase is the use of the multibody model in order to give a detailed explanation of the different technique efficiencies through a review of the experimental campaign results.

1.4 Overview of the thesis

Chapter 2 introduces the essential signal processing theoretical background utilized to detect faults from experimental data. Synchronous average, cyclostationarity and wavelet time-frequency techniques are explained as are statistical coefficient and cyclostationary indicators. Moreover the method adopted to define pass-fail value decisions, called Tukey's method, based on a non-statistical approach, is explained.

Chapter 3 presents the application of the different processing techniques to the heavy-duty wheel case. The set up is described and the sensor which is best able to detect the fault presence in the initial operating phases is determined. Concerning the experimental condition monitoring phase, synchronous average is calculated over the wheel rotation in order to highlight the phenomena that have wheel rotation as periodicity (e.g. the contact between defect and test bench drum). Moreover, Kurtosis and Root Mean Square parameters

are utilized as statistical coefficients in order to define the state of health of a wheel and to obtain upper thresholds for the pass/fail decision. Successively, cyclostationary theory is applied to extract information from the frequency/order domain of the processed signal. Then, the Continuous Wavelet Technique is applied over one wheel revolution obtaining spectral results in terms of wheel orders, which are useful for the diagnostics. Finally, a monitoring-diagnostic algorithm is proposed, ready to be implemented in a work station at the end of the production line.

Chapter 4 presents the dynamic characterization of the heavy-duty wheel, based on experimental modal analysis and numerical finite element models. Due to the viscoelastic nature of the wheel tread, the effect of static preload, dynamic load amplitude and frequency are taken into account through a dedicated material test campaign.

Afterwards in Chapter 5, the phenomena behind the measured anomaly vibratory level in case of tread/hub connection defects are described, modifying the 'Brush model' formulated by Pacejka. This approach enables an explanation of the operational conditions and defect size influences on the vibration signal to be given.

A heavy-duty wheel multibody model is described. The contact algorithm utilised, based on non linear Hertzian theory is reported. Furthermore, the missing adherence defect is simulated and the obtained acceleration signals are compared with the experimental data. In conclusion, in Chapter 6, a review of the experimental campaign results is presented, giving an explanation of the various technique efficiencies, based on the diagnostics information given by the model results. In Appendix 1, a multibody model of a ball bearing is reported, comparing the same contact algorithm adopted in the wheel model with other contact techniques.

Chapter 2

Signal processing techniques

2.1 What is the chapter about?

This chapter gives a theoretical background concerning essential signal processing techniques adopted for the determination of anomalies in rotating mechanical components. In particular this chapter focuses on:

- classification between stationary and non stationary signal;
- time domain analysis techniques: Synchronous average and statistical parameters;
- frequency domain analysis techniques;
- cyclostationary techniques and relative parameters;
- time-frequency techniques: Continuous wavelet transform.

The reader is referred to [39, 40] for more detailed theoretical background.

2.2 Introduction

The major challenge of condition monitoring is to find the technique that is able to emphasize the defect presence considering a reasonable computation time. As a matter of fact, the type of signal to be analyzed has an influence on the

type of analysis to be carried out, and also on the choice of analysis parameters. That is why it is a pivotal step to examine the various types of signals that are encountered in practice. The typical classification of signals considers [41, 42]:

- Stationary signals;

- Non stationary signals

The **stationary signals** are characterized by time-invariant averaged properties and thus independent of the particular sample record used to determine them. This applies to both $deterministic$ and $random$ signals. In particular, a random signal $x(t)$ is called wide-sense stationary if the first order (i.e. mean) and second order (i.e. covariance) statistics of its PDF (i.e. Probability Density Function) are time-independent. If all moments (or cumulants) of the PDF are time-independent, then the random signal $x(t)$ is strict-sense stationary.

Since a **non-stationary random signal** is a signal the statistical structure of which changes as a function of time, it can be defined as a signal which satisfies a non-property, the property of non-stationarity. Non-stationary signals may be divided into continuous non-stationary signals and transient signals which may be defined as those which start and finish at zero. It is interesting to look at another particular class of non-stationary signals that includes the so-called **cyclostationary** signals, recently investigated by Antoni in the area of condition monitoring of rotating machinery [6, 9]. Analysis of stationary signals has largely been based on time domain techniques and on the Fourier Transform, which identifies the constituent frequency components within the signals. Sections 2.3 and 2.4 treat some concepts concerning the time and frequency domain analysis respectively.

Although the Fourier Transform can be used in analysing signals with periodic impulses (giving rise to uniformly spaced harmonics and sidebands), the time-averaging approach adopted in the Fourier Transform is ineffective in evaluating the time-dependent behaviour of the frequency components.

In contrast, time-frequency techniques decompose a one-dimensional time-series signal into a two-dimensional plane by exposing the time-dependent

variations of characteristic frequencies within the signal, thus presenting a valid and more effective tool for non-stationary signal analysis than the Fourier Transform. In this work the Continuous Wavelet Transform (CWT) is described, being adopted in the diagnostics methodology. The capabilities and the drawbacks of this techniques are explained in Section 2.5. Eventually, the properties of the cyclostationary techniques are exploited in Section 2.6.

2.3 Time domain analysis

2.3.1 Time-domain statistical parameters

The time series of a signal can yield a big amount of information. A visual inspection of the portions of the time domain waveform can reveal the nature of the signal (i.e. stationary or non-stationary) and the presence of some intrinsic periodicities. Simple signal metrics applied to the measured time domain signal can give some useful information which cannot be extracted from other domain analyses. Moreover, time domain metrics are cheap and simple to implement and they can be determined through the Probability Density Function (PDF). It is worth noting that they cannot be used to directly indicate the locations of the defect. Hence, for fault detection purposes, we can refer to:

- energy parameters;

- peakedness parameters.

The Root Mean Square value (RMS) is an energy dimensional parameter reflecting the overall level of the signal while the Kurtosis parameter is a non-dimensional parameter that indicates the peakedness of a signal.

The Kurtosis is a measure of the peakedness of the PDF of a real-valued random variable. The kurtosis value is useful in identifying transients and spontaneous events within vibration signals and it is typically normalized by

the square of the second moment as follows:

$$K = \frac{1}{N}\sum_{i=1}^{N}\frac{(s(i)-\bar{s})^4}{\sigma^4} \tag{2.1}$$

where $s(i)$ is the instantaneous amplitude of the vibration signal, $\bar{s}$ is the average amplitude, σ^2 is the variance of the signal and N is the number of samples. The K value is constant irrespective of the signal amplitude or frequency. As depicted in defining A the amplitude of a peak and B the amplitude of the uniformly distributed background noise, the higher is the ratio A/B the larger is the K value. Increasing the number of such peaks introduced in the signal, while keeping the ratio A/B constant, reduces the kurtosis value.

2.3.2 Synchronous Average

The Synchronous Average $m_x(\vartheta)$ of a measured signal $x(\vartheta)$, synchronized with the rotational element in the angle domain ϑ, is evaluated as the ensemble average over a number of rotations M, each corresponding to one angular period Θ, as follows:

$$m_x(\vartheta) = \frac{1}{M}\sum\nolimits_{l=0}^{M-1} x(\vartheta + l\Theta), \quad \text{with } 0 \leq \vartheta < \Theta \tag{2.2}$$

where $M\Theta$ is the whole length of the signal. Synchronous Averaging (SA) is a well adopted signal processing technique which enables periodic waveforms to be extracted from noisy signals.

Synchronous Averaging is a rather common method for the early detection of failure in rotational elements as gears, bearings and wheels and is basically obtained by synchronizing the samplings of the measured signal with the rotational element of interest and evaluating the ensemble average over many revolutions [7, 8]. Hence, a Synchronous Average contains only the components synchronized with the revolution of the rotational element being studied. If sufficient averages are taken, the Synchronous Average closely approximates a truly periodic signal with periodicity corresponding to one revolution of the

selected rotational element [2, 3]. This process strongly reduces the effects of all the vibration sources non-synchronous with the reference, including other rotational elements and the background noise. Classically, this has been accomplished using a tachometer signal which delivers one pulse per revolution [43, 44]. However an optical encoder (with multiple pulses per revolution) can also be used for a better angular resolution.

Particular techniques have also been proposed for angular resampling of the vibration signal without the need of a speed sensor [7]. This method is carried out by means of a keyphasor signal that is typically a once per shaft revolution event. This signal is used to measure the shaft speed and represents the reference for measuring the vibration phase angle. To determine the resample times, normally it is assumed that the rotating component is undergoing constant angular acceleration. The corresponding amplitudes are calculated by interpolating between the sampled data using a linear interpolation method.

2.4 Frequency domain analysis

The theoretical frequency spectrum of a signal $x(t)$ is usually described by its Fourier Transform given by:

$$X(f) = \int_{-\infty}^{+\infty} x(t) e^{-j2\pi ft} dt \tag{2.3}$$

with f is the frequency variable. When implemented by DSP, the Fourier spectrum is usually approximated by the Discrete Fourier Transform (DFT). The differences from the theoretical definition expressed by the Equation 2.3 are the following:

- the use of time-discrete sampled signals;

- the observation and summation over a finite time interval;

- the discrete nature of the frequency spectrum.

The FFT [45] is the fast algorithm for calculating the DFT of a block g(n) of N samples of data giving a spectrum $G(k)$ of N frequency lines, using the formula:

$$G(k) = 1/N \sum_{n=0}^{N-1} g(n) \exp(-j2\pi kn/N) \tag{2.4}$$

Equation 2.4 assumes that $g(n)$ is one period of a periodic signal, so that the spectrum is that of the corresponding Fourier series. The sample index number n represents the time $n\Delta t$, where Δt is the reciprocal of the sampling frequency f_s. Similarly, the frequency index k represents the frequency $k\Delta f$, where Δf is the spectral line spacing, the reciprocal of the record length ($= N\Delta t$).

Because the time signal is sampled, the spectrum $G(k)$ is also periodic, with a period equal to the sampling frequency f_s. When the signal $g(n)$ is real, the negative frequency components are the complex conjugates of the positive frequency components, and there are thus only $N/2$ independent complex spectrum values. Because of the periodicity of the spectrum, the second half (from $f_s/2$ to f_s) represents the negative frequency components (from $-f_s/2$ to zero). This explains why all frequencies in the original signal outside this range ($-f_s/2$ to $f_s/2$) must be removed by a low pass filter before digitization, as they would otherwise mix with the true components within this range causing " aliasing". As reported by Randall in [45] the FFT is a powerful tool when it is used with a harmonic and sidebands cursor in order to evaluate some amplitude/phase modulation effects.

2.5 Time-frequency analysis

As said before the problem of analysing measured signals in the frequency domain is solved by applying a DFT on the signals. The main characteristics of this approach are that:

- only spectral results, which are an average for the duration T of the observation interval, are obtained;
- the frequency resolution Δf of the signal is limited by the length of the observation window.

When the nature of the signal is varying with time, a repeated Fourier analysis for consequent time segments tries to describe the temporal variation of the signal spectrum. This well known technique is called *Short Time Fourier Transform* (STFT). The principal limitations of this approach are:

- for each analysed time segment, only average results are obtained, requiring short analysis segments for a good time resolution;
- the shorter the analysed time segment is, the coarser the resulting frequency resolution will be.

A more rigorous explanation of the latter is the Uncertainty Principle or Bandwidth-Time product that is easily proved in [46] using the Parseval theorem and the Schwartz's inequality . This principle states that:

$$\Delta f \cdot \Delta t \geq \frac{1}{4\pi} \tag{2.5}$$

where Δf is the frequency resolution expressed in Hertz and Δt is the time resolution expressed in seconds. It is not so difficult to understand that Equation 2.5 points out a limitations of the STFT analysis methods: a fine resolution in both time and frequency domains at the same time cannot be obtained.

Several techniques have been developed [47, 48] to overcome this problem and to analyse different types of non-stationary signals. As well reported in [48], one can distinguish three important classes of non-stationary signals:

- Evolutionary Harmonic Signals related to a periodic phenomenon (i.e. rotation) of varying frequency;
- Evolutionary Broadband Signals with a broadband spectrum but with spectral content evolving with time (i.e. road noise);

- Transient Signals which show a very short time segment totally evolving in nature (i.e. door-slam acoustic response and diesel engine irregularity inside one combustion cycle).

Since this work deals with Transient and Cyclostationary signals, Continuous Wavelet analysis has been proposed as proper analysis tools.

2.5.1 Continuous Wavelet Transform (CWT)

When referring to the definition of the Fourier Transform (Equation 2.3), it can be seen that this formulation describes the signal $x(t)$ by means of a set of functions $e^{j\omega t}$ forming a basis for signal expansion. These functions are continuous and of infinite duration. The spectrum corresponds to the expansion coefficients.

An alternative approach consists of decomposing the data in time-localized waveforms. Such waveforms are usually referred to as wavelets. In the last decades the theoretical background of the wavelet transform has been extensively reported [10, 49, 50]. The Continuous Wavelet Transform (CWT) of the time signal $x(t)$ is defined as:

$$CWT(a,b) = \frac{1}{\sqrt{a}} \int_{-\infty}^{+\infty} x(t)\psi^* \left(\frac{t-b}{a} \right) dt \tag{2.6}$$

with

$$a \in R^+ - \{0\}, b \in R \tag{2.7}$$

and with

$$\psi^* \left(\frac{t-b}{a} \right) \tag{2.8}$$

called $'$mother (analyzing) wavelet$'$.

This is a linear transformation decomposing the original signal into elemen-

tary functions $\psi_{a,b}$:

$$\psi_{a,b}(t) = \frac{1}{\sqrt{a}}\psi\left(\frac{t-b}{a}\right) \tag{2.9}$$

which are determined by the translation (parameter b) and the dilation (parameter a) of a ′mother wavelet′ $\psi(t)$. The translation parameter b describes the time localization of the wavelet, while the dilation a determines the width or scale of the wavelet. It is worth noting that, by decreasing the scale parameter a, the oscillation frequency of the wavelet increases, but the duration of the oscillation decreases, so it can be noted that exactly the same number of cycles is contained within each wavelet. Therefore, an important difference with classical Fourier Analysis, in which the time window remains constant, is that the time and frequency resolution now becomes dependent on the scale factor a. For the CWT, in fact, the width of the window in the time domain is proportional to a, while the bandwidth in the frequency domain is proportional to $1/a$. Thus, in the frequency domain, the CWT has a good resolution for low frequencies and, in the time domain, good resolution for high frequencies; the latter property makes the CWT suitable for the detection of transient signals. One of the most interesting forms of wavelets is the Morlet wavelet defined as:

$$\psi(t)_{morlet} = \frac{1}{\pi^{-1/4}}e^{-t^2/2}e^{j2\pi f_0 t} \tag{2.10}$$

wheref_0 is the central frequency of the mother wavelet. The term $1/\pi^{-1/4}$ is a normalization factor which ensures that the wavelet has unit energy; the Gaussian envelope $e^{-t^2/2}$ modulates the complex sinusoidal waveform. In this work the impulse mother wavelet is used. The impulse mother wavelet is defined as follows:

$$\psi(t)_{impulse} = \sqrt{2\pi}e^{2\pi j f_0 t - |2\pi t|} \tag{2.11}$$

where f_0 is the central frequency of the mother wavelet and j throughout is the imaginary unit. Since both Morlet and Impulse wavelets are complex mother

wavelets, we can separate the phase and amplitude components within any signal. Usually, the result of the CWT is graphically represented in the time-scale plane or in the time-frequency domain, using the relationship $f = f_0/a$ between the central frequency of the analyzing wavelet f_0 and the scale a. Moreover, when complex analyzing wavelets have been used, only the amplitude will be considered and represented using a linear scale. Concerning the CWT implementation, the algorithm proposed by Wang and McFadden [11] has been applied taking the advantages of the FFT algorithm.

Figure 2.1 plots the Morlet and Impulse mother wavelets for different values of the scale parameter a. The values of f_0 are taken from [51], equal to 0.8125 Hz for Morlet mother wavelet and 20 Hz for Impulse one. The figure highlights the different qualities of the two mother wavelets: a remarkable feature of the Morlet wavelet is that its Fourier spectrum is Gaussian, whilst the Impulse one is taken into account due to its capability for the analysis of impulses in vibration signals.

Figure 2.2, taken from [40] and [39], depicts an illustrative example in order to show the effectiveness of the two mother wavelets. The simulated signal simulates typical machine signals containing sinusoids and impulse responses. Comparing the Morlet and Impulses wavelet capabilities, the superiority of the latter in distinguishing close frequency components it is clear. Moreover the Impulse wavelet is able to detect continuous frequency components as well as transient components.

2.6 Cyclostationary analysis and indicators

A signal is cyclostationary if some of its statistics present periodicities. Averaging can make it possible to extract the deterministic part of the signal. If the signal obtained after subtracting this deterministic part from the synchronized signal does not exhibit cyclostationarity, the signal is said to be cyclostationary at an order '1'. In general terms, a signal is cyclostationary at an order 'n' if its statistical properties at order 'n' are periodic . It has to be noted that if local

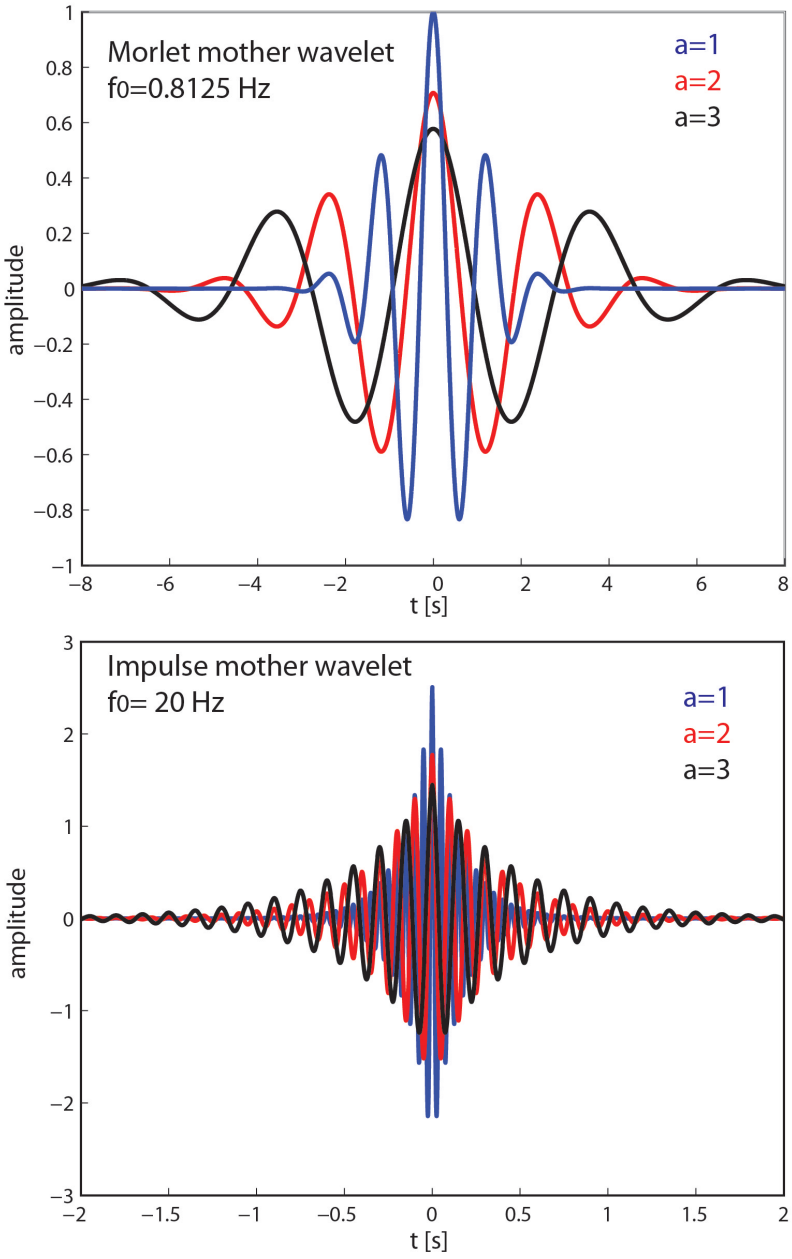

Figure 2.1: Comparison of Morlet and Impulse mother wavelet

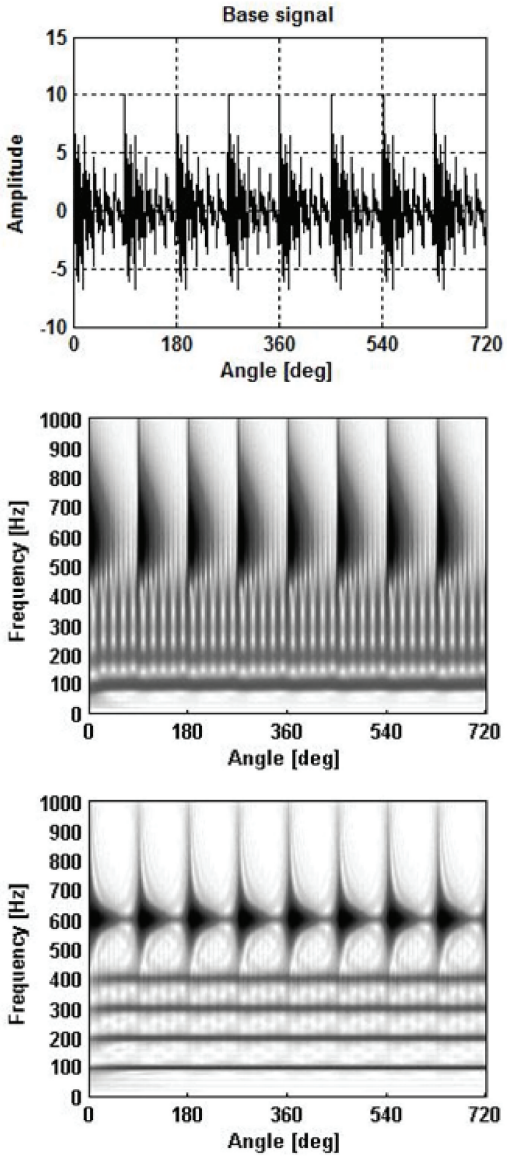

Figure 2.2: Comparison of two different CWT obtained through Morlet mother wavelet (B) and Impulse mother wavelet (C) in case of a simulated signal (A).

faults produce impacts the signals have to be considered as non-stationary and characterized by a transient vibration signal.
The cyclostationary approach has been used for the estimation of indicators of (nth-order) cyclostationarity (ICS_{nx}). The reader is referred to [6, 9] for a full explanation and definition of cyclostationarity. Hereafter a brief overview of the used indicators is given. In order to define ICS_{nx}, two possible approaches can be used, based on moments or cumulants, respectively. According to [9], the use of cumulants is more advantageous, as the nth-order cumulant provides only new information, which is not included in lower-order cumulants. The first order cyclostationarity content has been computed as the Discrete Fourier Transform (DFT) of the sampled signal $x[n]$, called the first order cyclic cumulant ($\hat{C}^{\alpha}_{1x}$), Equation 2.12. The second order cyclostationarity content of the signal has been evaluated through the second order cyclic cumulant ($\hat{C}^{\alpha}_{2x}$) estimated as the Discrete Fourier Transform of the squared residual signal $r^2[n]$ as in Equation 2.13.

$$\hat{C}^{\alpha}_{1x} = N^{-1} DFT\left\{x\left[n\right]\right\}(\alpha) \tag{2.12}$$

$$\hat{C}^{\alpha}_{2x}(\varphi = 0) = N^{-1} DFT\left\{r^2\left[n\right]\right\}(\alpha) \tag{2.13}$$

Where $DFT\left\{z\left[n\right]\right\}(\alpha)$ refers to the Discrete Fourier Transform of the generic sampled signal $z[n]$ of length N calculated at an order α. Moreover, the first and second order cyclic cumulants can be conveniently used to summarize the information related to first- and second-order cyclostationary contents by defining the following indicators of cyclostationarity:

$$ICS_{1x} = \frac{\sum\limits_{\alpha \neq 0} \left|\hat{C}^{\alpha}_{1x}\right|^2}{\left|\hat{C}^{0}_{2x}(0)\right|} \tag{2.14}$$

$$ICS_{2x} = \frac{\sum_{\alpha \neq 0} \left| \hat{C}^{\alpha}_{2x}(0) \right|^2}{\left| \hat{C}^{0}_{2x}(0) \right|^2} \tag{2.15}$$

Equations 2.14 and 2.15 are consistent estimators of the cyclic cumulants at the zero angle lag ($\varphi = 0$) for a sampled signal. It is worth noting that indicators ICS_{1x} and ICS_{2x} are without dimension, as they are normalized by the energy of the residual signal $\hat{C}^{0}_{2x}(0)$;

2.7 Definition of pass-fail decision value: Tukey's method

The pass/fail thresholds are generally defined starting from the analysis of a large group of healthy components applying statistical techniques with the a-priori knowledge of the real data distribution. However, in case of a small number of samples, it is advisable to use non statistical techniques. This is the case adopted in this research activity in which Tukey's non statistical method has been applied to a group of 15 healthy wheels.

The Tukey's method [52] is a simple but effective procedure for the identification of anomalies in a distribution of data. Unlike common statistical procedures,Tukey's method is a non-parametric technique that does not consider any distributional assumptions about the statistical behavior of the data.

Let $x_1, x_2, ..., x_n$ be a series of observations such as statistical parameter values or cyclostatonarity indicators. These data are arranged in ascending order and then ordered into four quarters. The boundary of each quarter is defined by Q_1, Q_2 and Q_3, called the $1st$ quartile, $2nd$quartile and $3rd$ quartile, respectively. The difference $|Q_3 - Q_1|$is called the inter-quartile range. The Tukey's threshold for anomalies is defined at $Q_3 + 3\,|Q_3 - Q_1|$. Observations falling beyond this limit are called serious anomalies and any observations x_i such that $Q_3 + 1.5\,|Q_3 - Q_1| \leq x_i \leq Q_3 + 3\,|Q_3 - Q_1|$ are called possible anomalies. Figure 2.3 reports a schematic representation of Tukey's method procedure.

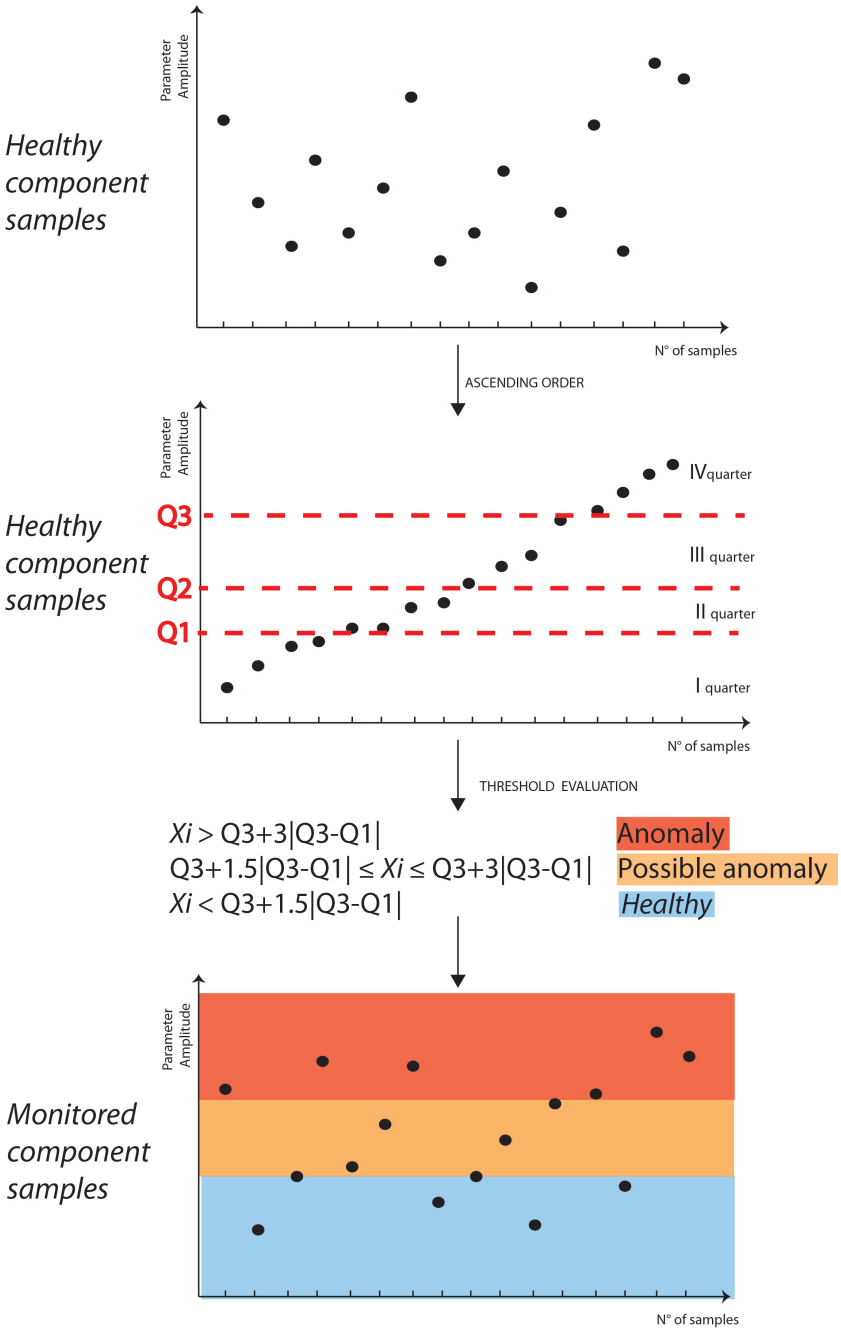

Figure 2.3: Simplified representation of Tukey's procedure

Chapter 3

Heavy-duty wheel monitoring and diagnostics analysis

3.1 What is the chapter about?

This chapter aims at formulating a monitoring and diagnostics algorithm able to detect fault presence in a heavy-duty wheel after a limited testing time. In this chapter, the questions that have to be solved are:

- Is it possible to detect a fault presence in the wheel after a limited testing time?
- Which is the best sensor and the best operational condition able to detect anomalies?
- Is the rust causing an anomalous vibratory level?
- Is it possible to determine the defect nature from the signal signature?

3.2 Introduction

Heavy-duty wheels are components mainly used in applications as automatic vehicles and motor trucks mainly.

In the wheels object of analysis, the polyurethane coating is made from an elastomer obtained exclusively from raw materials for synthesis. The

polyurethanes are chemical compounds obtained by a polymerization reaction that is triggered and takes place with the mixing of two components belonging to two different families of compounds, previously heated to temperatures such as to keep them in the liquid state and with relatively low viscosity. The reactive mixture is cast or injected into molds heated in which are housed the metallic cores previously cleaned using special chemical processes. The temperature of the mold allows the completion of the polymerization reaction inside of the polyurethane and the chemical anchoring of the polyurethane adhesive possibly present on the surface of the core.

The cleaning is a very important phase in the production process of the wheels, since the impurities that remain on the surface of the core, such as sand casting or other substances, can interfere with bonding of the adhesive and the polyurethane. On the hub, after cleaning, it is sprayed an adhesive in the form of thin films. The hub of the wheel must be subjected to machining of ”roughing surface” in order to remove the sand from the foundry process or the surface oxides which can be formed. If this processing phase is not done properly some problems can arise:

- non-uniform adhesion of the adhesive on the metal surface;
- no complete wettability of the metal surface;
- extended defect.

Moreover the thickness of the film of adhesive must not exceed 10-20 microns thick in order to not affect the mechanical characteristics. The wheels in their final form can not be immediately packaged and delivered to the customers since the polyurethane requires a certain period of time to acquire the desired properties. Compared to the cleaning phases, in which the hub is not moved manually, in the subsequent operations of application of the adhesive and the positioning of the mold, the manipulation of the pieces by an operator is present. The operator has to be particularly careful to not touch the surface of the adhesive in order to prevent contamination with impurities that would lead a failure of the

polyurethane-hub adherence. In this activity, different experimental tests have been carried out in order to identify defects that can occur during the manufacturing process. Results are presented for numerous defects in a large variety of operational conditions.
The main goal activity is the identification of adapt processing techniques based on vibration signal able to identify a missing adherence anomaly at the end of the production line. For this purpose different test configurations (speed and load) have been evaluated trying to highlight at the best the fault presence.
Concerning the condition monitoring phase, the Synchronous Average has been calculated over the wheel rotation (namely SAw) in order to highlight the phenomena that have the wheel rotation as periodicity (e.g. the contact between defect and drum of the test bench). Moreover, the Kurtosis and Root Mean Square (RMS) parameters applied on the SAw have been utilized as statistical coefficients in order to define the state of health of a wheel and to obtain upper thresholds for the pass/fail decision. In the mean time, the cyclostationarity theory has been applied for the extraction of information from the frequency/order domain of the processed signal. Eventually, the Continuous Wavelet Technique (CWT) has been applied over one wheel revolution obtaining spectral results in terms of wheel orders, useful for the diagnosis phase.
The originality of this activity consists of the attempt to study the presence of anomalies in a heavy-duty wheel comparing the detection and diagnostic capability of different processing techniques as Synchronous Average and cyclostationarity using well-suited indicators. Furthermore, these indicators are adopted to determine threshold pass/fail decision values through the Tukey's non statistical method. As the authors are aware, it is the first time this component is considered from a monitoring- diagnosis standpoint.

3.3 Test set up

3.3.1 Faulty wheel types

The wheels being studied are composed of a polyurethane tread and a cast iron hub, with 100 mm radius, 50 mm of width and 1200 kg of maximum load. Wheels with different types of faults have been manufactured “ad hoc”with anomalies similar to real ones. Such anomalies consist of incorrectly adherence zones between tread and hub and localized and distributed rust presences in the hub surface. Figure 3.1 depicts the artificial faults’ dimension in the tangential direction (B) and in the horizontal direction (L).

In this work, localized faults of:

- missing adherence (namely MA) of about 0.3 cm dimensions in the horizontal and tangential directions;
- localized rust (namely LR) of about 5 cm dimension in horizontal and 2 cm in tangential direction and distributed rust on the entire hub (namely DR)

have been analyzed.

Furthermore, four kinds of extended missing adherence localized faults have been considered:

- A1 (B=1cm and L=5cm);
- A2 (B=2cm and L=5cm);
- A3 (B=1cm and L=2 cm);
- A4 (B=2cm and L=2cm).

The main objective is to verify the effectiveness of the processing techniques and to study operational condition and size defect influences on the measured signals. Every kind of defect has been reproduced on three different wheels in order to have a good repeatability of the results.

Eventually, a set of 15 wheels without any defect has been analyzed for the estimation of a reliable reference pattern representative of the normal condition. The vibration parameters relative to these 15 wheels are referred to the following as healthy wheels (HW)

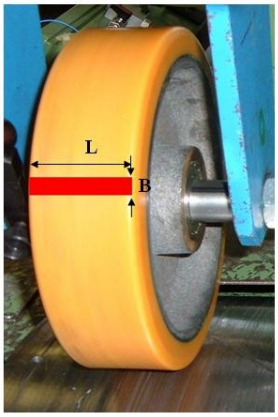

Figure 3.1: Defect dimensions

3.3.2 Experimental apparatus and test conditions

A wide experimental investigation is carried out on heavy-duty wheels in a test bench available at the company's laboratory. The test bench consists of a bottom support, including a drum driven by an electric motor controlled by an inverter and an upper part composed by two hydraulic pistons that apply the load to the wheel under test, as depicted in Figure 3.2.

Tests are carried out at two different drum speeds (4 and 10 km/h) and three different loads (350, 700 and 1000 kg), representing the real range of operational conditions. The results in terms of raw time data and frequency analysis have shown that the operational condition of 4 km/h and 1000 kg is the best compromise (referred hereafter as "best" condition) of rotational speed and applied load in order to give a clear and meaningful response signal.

During tests, the vibration signal is acquired by means of a piezoelectric tri-

axial accelerometer (PCB 356A01, frequency range 1-10000Hz), as shown in Figure 3.2 (position A) and a condenser microphone (1/2" prepolarized) is utilized to measure the sound emission (C). Moreover an acoustic emission (AE) sensor has been used in order to capture the transient elastic waves generated from a rapid release of strain energy caused by a deformation or damage (B). In particular since the acoustic emission sensor is specifically manufactured for measuring the elastic waves - having high frequency content - such a sensor is negligibly affected by mechanical components - having a low frequency content, less than 20 kHz [53, 54]. Finally four load cells (LAUMAS FTO Kg 5000) have been used to measure the global force in the vertical direction (D).

The signals are acquired with a sample frequency of 12800 Hz for a duration of about 23s by using LMS hardware and software instrumentation [55]. Simultaneously with the acquisition at constant sample frequency, an on-line order tracking analysis has been also performed since the number of time samples varies every rotation of the wheel due to fluctuation of instantaneous speed. This technique requires the measurement of a "trigger" signal, i.e. a signal phase-locked with the angular position of one rotating element in the system, that gives a synchronized signal with the wheel and a synchronized signal with the drum revolution. For these reasons two optical tachometer sensors (KEYENCE- LVS series) both positioned near the wheel-drum contact are used in order to produce one pulse per revolution of the wheel and the driving drum (E). This kind of tachometer gives a pulse when a reflecting strip crosses the optical sensor of the tachometer.

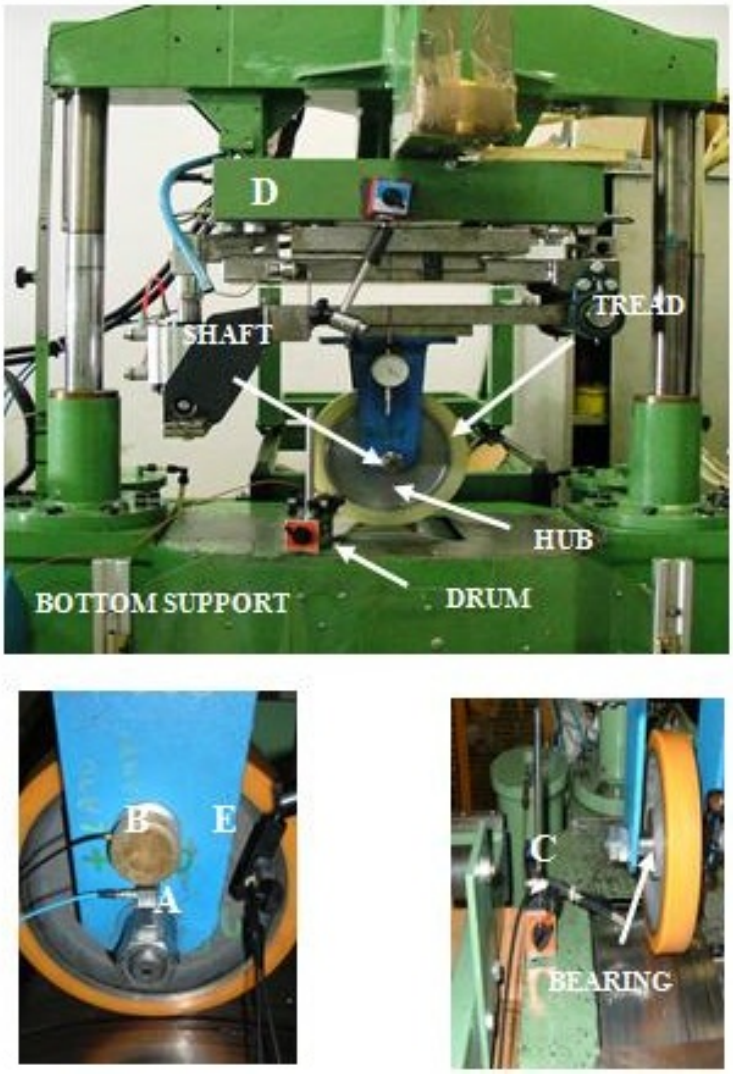

Figure 3.2: Test bench: A) accelerometer ; B) acoustic emission sensor; C) microphone; D) load cells; E) optical tachometer sensor

3.3.3 Synchronous average procedure

The Synchronous Average technique has been applied on the measured signals in order to highlight the phenomena that are linked to the presence of faulty wheels.

Two different Synchronous Averages have been computed. Firstly, the Synchronous Average of the acceleration signal over the drum revolution (called SAd) has been performed starting from the synchronized acceleration signal, by using the tachometer signal of the drum as a reference. Then, the "purified signal" has been calculated as the difference between the synchronized signal and the SAd , obtaining a new signal with reduced periodicities related to the driving drum and increased information concerning the manufactured faults linked to the wheel periodicities. Consequently, the "purified signal" has been synchronized (by using the tachometer of the wheel) and averaged over the wheel rotation obtaining the Synchronous Average of the acceleration signal over the wheel revolution (namely SAw). Eventually, the residual signal was determined as the difference between the above purified signal and SAw.

As an example of the result of such a procedure, Figure 3.3 depicts the raw acceleration signal measured at the operational condition of 4km/h (speed) and 1000 kg (load) in the case of a missing adherence localized defect and the further processing phases. This purification process gives a strong reduction of the components related to the driving drum rotation and the possibility of analyzing the residual signal depurated from all the known periodicities of the system.

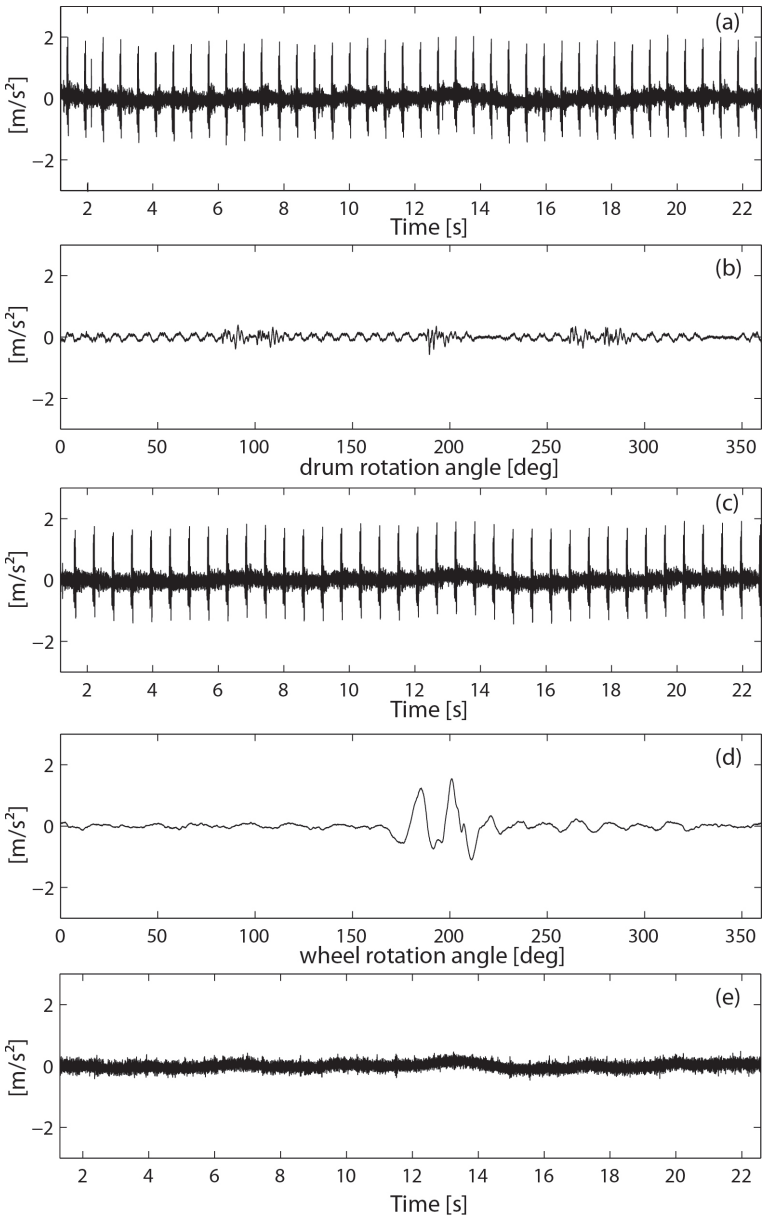

Figure 3.3: Processing procedure: a) raw acceleration signal, b) SAd, c) purified signal, d) SAw and e) residual signal at the operational condition of 4km/h and 1000kg

3.3.4 Determination of the best sensor device

Subsequently, analyses have been carried out in order to detect which sensor among those used is best able to identify the non-stationary phenomena related to the presence of the defect.

Figure 3.4 shows the SAw for all the sensors at the same test condition (the "best" condition) and for the same defect type. This comparison leads to the conclusion that the accelerometer signal is the best compromise between simplicity in the mounting and clear response to an impulsive event. In fact, the acceleration signal consists of impulsive events linked to the wheel rotation and which occur when the artificial fault of the wheel comes into contact with the drum.

On the other hand, the load cells embedded in the test bench have a very slow dynamic response to an impulsive event and they are not able to precisely capture the presence of the defect.

Concerning the acoustic emission it exhibits quite good signals allowing a clear defect localization. The acoustic emission (AE) transducer adopted during the measurement campaign is a resonant type transducer. It means that every time the system realises elastic waves, the AE transducer is excited at its resonance frequency, generating a signal composed of a carrier component characterized by the resonance frequency, modulated by the physical phenomenon that causes the elastic waves, called the amplitude modulation component. The latter is the meaningful part of the AE signal because the carrier component contains only the information of the sensor resonance frequency. The demodulated signal is obtained purifying the signal of the AE sensor from the carrier component in order to analyse only the amplitude modulation. The demodulated AE signal has a frequency content in the field of the common frequencies of the mechanical phenomena, and so it can be analyzed with a traditional signal analyzer. The main drawbacks linked to the use of this transducer are that it requires a continuous control of the silicon grease, essential to realize good adherence between sensor and measured surface, and the high sensitivity to electrical interferences.

Microphone signals are not suitable for this kind of measurement due to the high environmental noise in the laboratory. In the following, only the results obtained by the accelerometer are shown.

During the entire test campaign, the wheel being tested has been subjected to a warm up procedure: it has been found that 30 seconds are enough in order to stabilize the tread temperature and to avoid the effect of localized tread deformation that can rise during the mounting phase. Figure 3.5 depicts the Synchronous Average of the acceleration signal for the A3 type of defect in the first minute of acquisition (black line) and in the second minute of acquisition (red line). As it can be noted the local deformation of the tread causes the presence of a peak in the SAw that vanished after the warm up procedure.

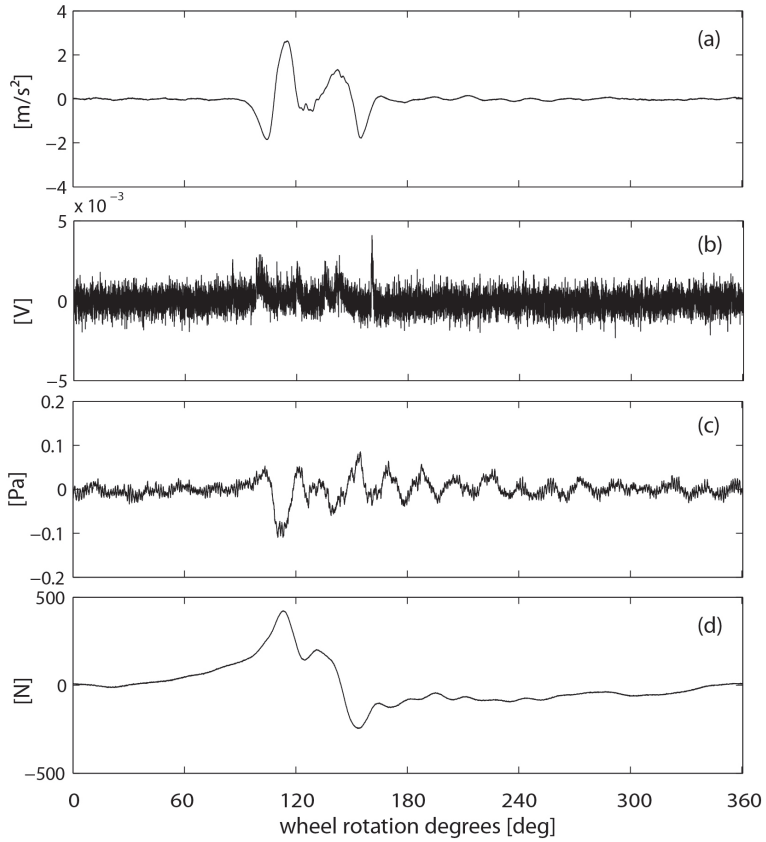

Figure 3.4: Synchronous Average of a) accelerometer signal, b) AE signal, c) microphone signal, d) load cell signal for the same defect type A2 at the “best” test condition

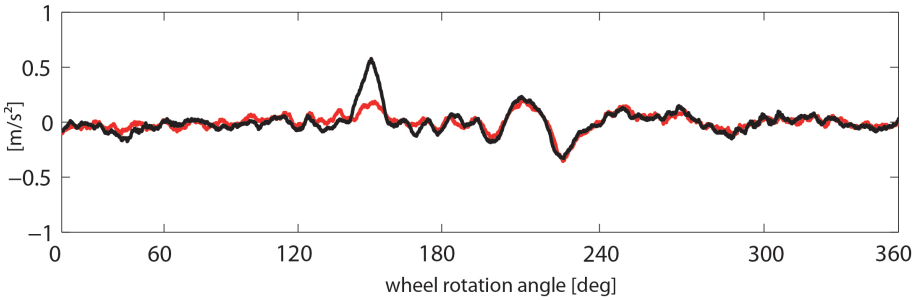

Figure 3.5: Synchronous Average of the acceleration signal for A3 defect in the first minute acquisition (black line) and in the second minute acquisition (red line).

3.4 Condition monitoring

The condition monitoring phase consists of the application of different techniques able to identify the presence of possible anomalies in the component. In the mean time the different processing techniques have to be objectified through well suited indicators, i.e. quantitative values able to estimate the healthiness level of a component.

3.4.1 Synchronous average: Kurtosis and RMS statistical parameter

The Kurtosis parameter, as previously described in Chapter 2, can be considered as a monitoring feature for faults producing impulsive excitations and it can be used to obtain a reliable upper threshold. To this purpose, Table 3.1 puts in evidence the Kurtosis values for the A1, A2, A3 and A4 defect types evaluated at the operational condition of 4 km/h and 1000 kg (the ìbestî condition). The values in the table represent the mean values over the three tested wheels having the same fault. As one can clearly see, the Kurtosis parameter assumes the highest values for the faulty wheels, whilst for healthy wheels it presents small values, less than 4.

Test conditions have a large influence on Kurtosis values, in fact in Table 3.2

the Kurtosis parameters at the test condition of 10 km/h and 350 kg (low load) present a smaller value with respect to those at 4 km/h and 1000 kg (high load), collected in Table 1. Furthermore, at the test condition considered in Table 3.2 the faulty wheels can not be clearly identified by using the Kurtosis parameter only (defect A3 exhibits a Kurtosis value smaller than the healthy wheels).

Table 3.3 shows the Kurtosis values evaluated for the same faulty wheel (type A2) at different test conditions. Again the test condition at 4 km/h and 1000 kg presents the highest Kurtosis values due to the presence in the signal of high amplitude peaks in the zone where the defect exists and very low elsewhere, see Figure 3.6. Furthermore the Kurtosis parameter has been applied to the SAw of the above mentioned 15 healthy wheels (Table 3.4 second column) and to 8 wheels with defect of MA, LR and DR type (Table 3.6, second column). Although this parameter is well suited for the recognition of extended missing adherence localized faults (A1, A2, A3 and A4), it is not really sensitive to small localized defect (MA) and to rust presence (LR and DR), as it shows almost the same value as healthy wheels.

As a consequence, a further statistical parameter, the root mean square (RMS) has been considered and compared to the previous one. The RMS is a statistical measure able to recognize the degree of irregularities of a signal and for this reason it appears well-suited for the recognition of defects such as rust or small localized defect that do not produce significant localized peaks. The RMS values computed on the SAw for the group of 15 healthy wheels and for the group of 8 faulty wheels are collected in the third column of Table 3.4 and Table 3.6, respectively.

Eventually, Tukey's method has been applied to the Kurtosis and RMS parameters evaluated for the group of healthy wheels (Table 3.4) in order to identify the pass/fail threshold value. With this approach the threshold value that discriminates healthy wheel from a possible faulty wheel has Kurtosis of 4.55 and RMS of 0.033 m/s^2 (accordingly to the method). The thresholds that give the certainty of faultiness are 5.48 and 0.039 for the Kurtosis and the RMS, respectively, as reported in Table 3.5. The comparison of the pass/fail thresh-

old value (Table 3.5) with the results reported in Table 3.6 enable to draw the following conclusions, as highlighted in Figure 3.7:

- the Kurtosis parameter was able to certainly identify only a wheel with LR fault (LR1) and a wheel with DR fault (DR3) as a possible fault. This low monitoring skill can be ascribed to the fact that the SAw signals do not contain high localized peaks, in case of MA, LR and DR defects.

- The RMS parameter was able to certainly identify two wheels with LR fault (LR1, LR2) and the three wheels with DR fault (DR2, DR3, DR4). Moreover, one wheel with MA fault (MA2) was recognized as possibly faulty. As result the RMS can be considered as a good monitoring parameter due to the fact that it is sensitive to missing adherence localized defect or localized-distributed rust. Nevertheless this parameter is not able to recognize all the defects giving the possibility of undesirable alarms.

Table 3.1: Kurtosis values at the operational condition of 4 km/h and 1000 kg for A1, A2, A3 and A4 defect types and for the healthy wheels (HW)

	A1	A2	A3	A4	HW
Kurtosis	16.01	13.17	12.01	13.26	3.27

Table 3.2: Kurtosis values at the test condition of 10 km/h and 350 kg for A1, A2, A3 and A4 defect types and for the healthy wheels (HW).

	A1	A2	A3	A4	HW
Kurtosis	6.03	7.12	3.25	4.12	3.27

Table 3.3: Kurtosis values for different test conditions concerning the A2 defect type.

	350 kg	700 kg	1000 kg
4km/h	9.76	13.03	13.07
10km/h	7.12	6.53	7.83

Table 3.4: Kurtosis and RMS values for the group of 15 healthy wheels at the "best" test conditions

Healthy wheels (HW)	Kurtosis	RMS$[m/s^2]$
HW1	3.12	0.02
HW2	3.15	0.027
HW3	3.08	0.023
HW4	3.67	0.03
HW5	2.96	0.026
HW6	3.57	0.024
HW7	2.56	0.017
HW8	3	0.033
HW9	3.31	0.026
HW10	3.33	0.027
HW11	2.89	0.022
HW12	3.17	0.024
HW13	3.62	0.026
HW14	3.81	0.025
HW15	4.03	0.025

Table 3.5: Kurtosis and RMS threshold values obtained using the Tukey's method at the "best" test conditions

Healthy wheels (HW)	Kurtosis	RMS$[m/s^2]$
Q1	3	0.23
Q2	3.17	0.025
Q3	3.62	0.027
$Q3 + 1.5\|Q3 - Q1\|$	4.55	0.033
$Q3 + 3\|Q3 - Q1\|$	5.48	0.039

Table 3.6: Kurtosis and RMS values for the group of 8 different faulty wheels at the "best" test conditions.

Faulty wheels	Kurtosis	RMS$[m/s^2]$
MA1	3.31	0.03
MA2	2.91	0.033
LR1	6.4	0.12
LR2	3.32	0.059
LR3	2.95	0.025
DR1	4.12	0.057
DR2	4.93	0.062
DR3	3.54	0.041

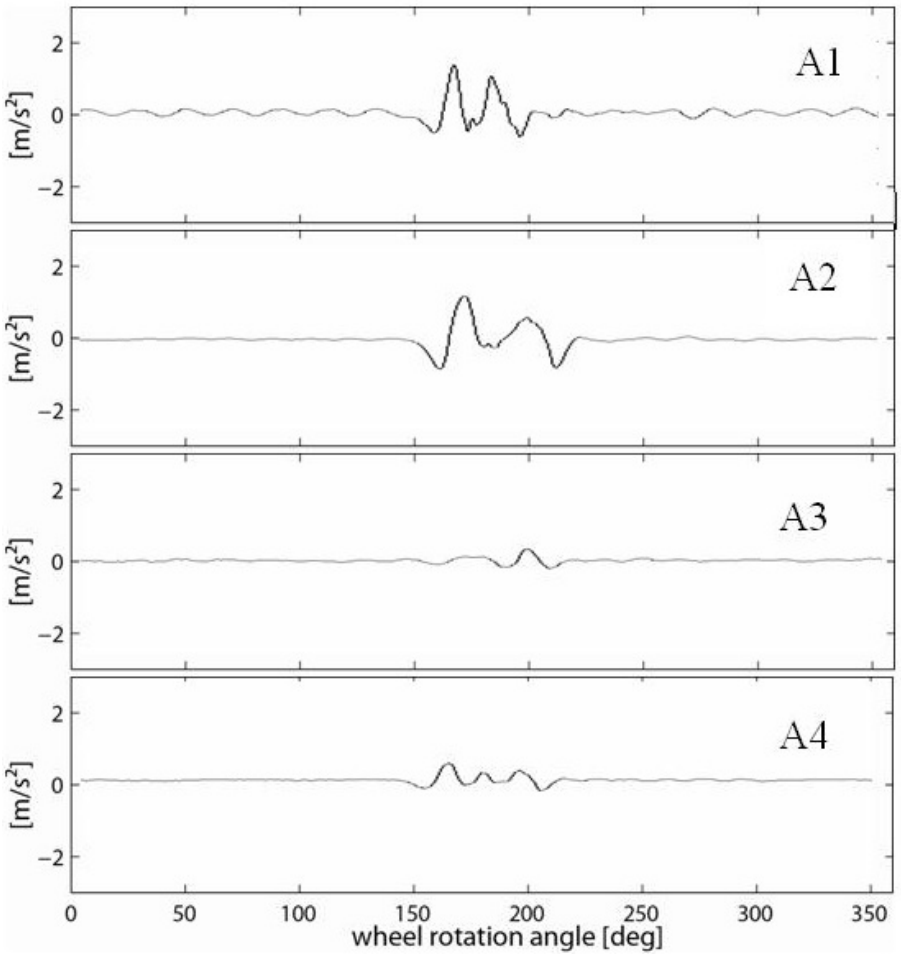

Figure 3.6: Synchronous Average of the acceleration signal for A1, A2, A3 and A4 defects at the “best” test condition

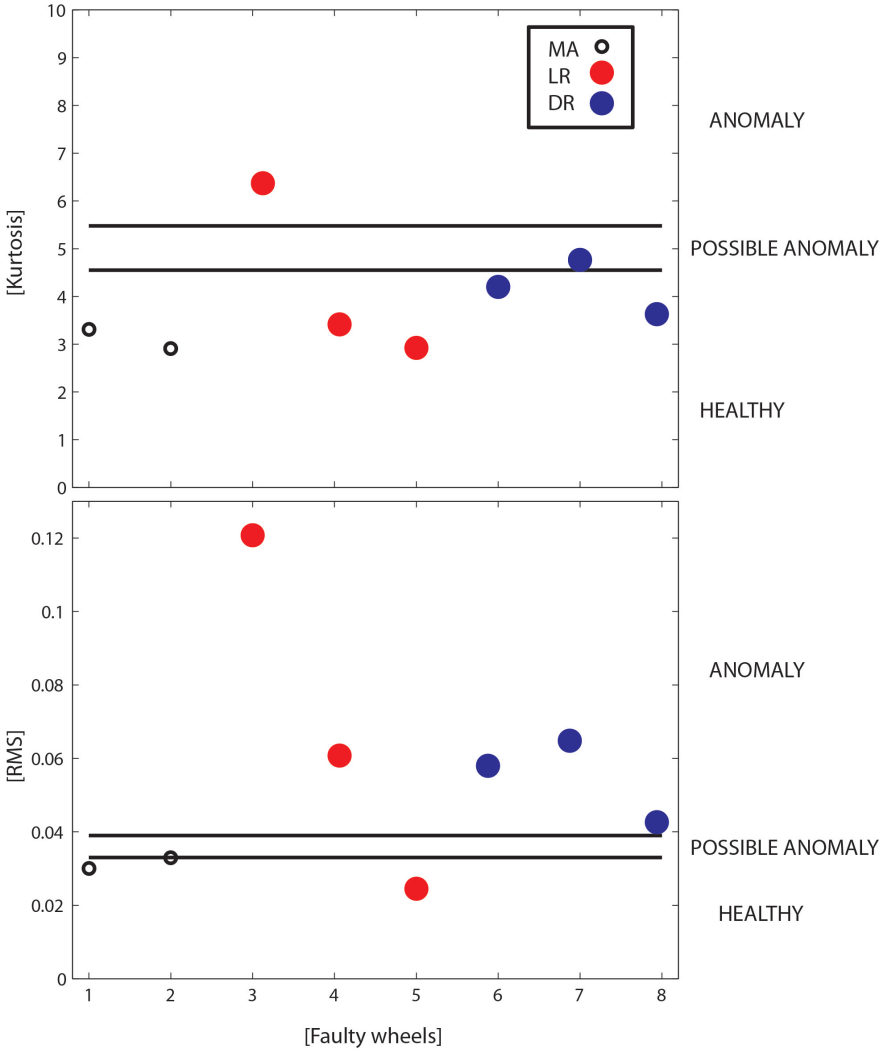

Figure 3.7: Kurtosis and RMS pass-fail distributions in case of MA, LR and DR defects

3.4.2 Application of Cyclostationarity: first and second order indicators

Since the processing techniques described above do not give a sufficient confidence in the identification of the faulty wheels, a further investigation has been carried out based on the study of the cyclostationarity properties of the signal. The first order cyclostationarity content has been computed as the Discrete Fourier Transform (DFT) of the sampled purified signal synchronized with the wheel rotation $x[n]$, called first order cyclic cumulant ($\hat{C}_{1x}^{\alpha}$):

$$\hat{C}_{1x}^{\alpha} = N^{-1} DFT\left\{x\left[n\right]\right\}\left(\alpha\right) \tag{3.1}$$

The second order cyclostationarity content of the signal has been evaluated through the second order cyclic cumulant ($\hat{C}_{2x}^{\alpha}$) estimated as the Discrete Fourier Transform of the squared residual signal $r^2[n]$:

$$\hat{C}_{2x}^{\alpha}(\varphi = 0) = N^{-1} DFT\left\{r^2\left[n\right]\right\}\left(\alpha\right) \tag{3.2}$$

It has to be noted that Equations 3.1 and 3.2 are consistent estimators of the cyclic cumulants at the zero angle lag ($\varphi = 0$) for a sampled signal. Moreover, the first and second order cyclic cumulants can be conveniently used to summarize the information related to first- and second-order cyclostationary contents by defining the following indicators of cyclostationarity:

$$ICS_{1x} = \frac{\sum\limits_{\alpha \neq 0} \left|\hat{C}_{1x}^{\alpha}\right|^2}{\left|\hat{C}_{2x}^{0}(0)\right|} \tag{3.3}$$

$$ICS_{2x} = \frac{\sum\limits_{\alpha \neq 0} \left|\hat{C}_{2x}^{\alpha}(0)\right|^2}{\left|\hat{C}_{2x}^{0}(0)\right|^2} \tag{3.4}$$

where $\alpha \in \bar{A}$ and $\overline{\mathcal{A}}$ is the set of wheel orders α presenting non-zero Fourier series coefficients. It is worth noting that indicators ICS_{1x} and ICS_{2x} are without dimension, as they are normalized by the energy of residual signal $\hat{C}^0_{2x}(0)$; they quantify the presence of first and second-order cyclostationary components within the signal, respectively. In the particular case α has been considered in the range 1st - 100th order since the higher spectrum amplitudes lie in this order range.

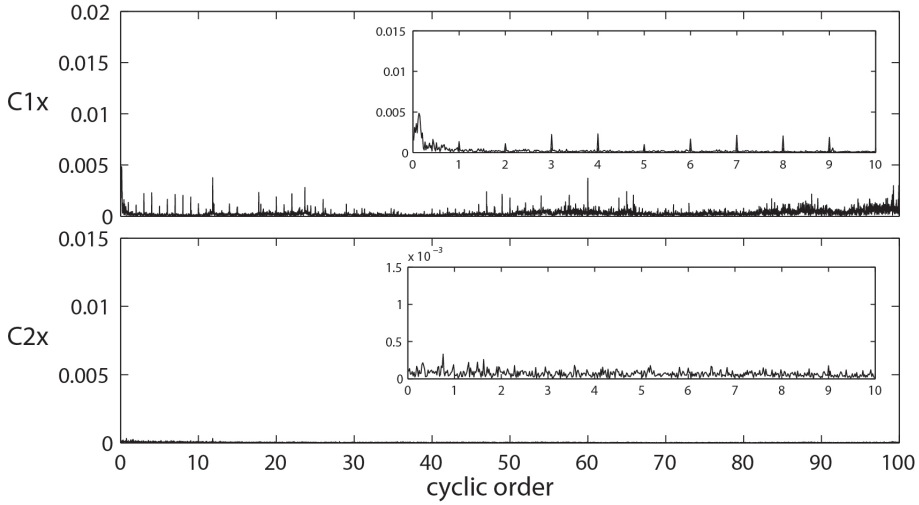

Figure 3.8: $\hat{C}^{\alpha}_{1x}$ and $\hat{C}^{\alpha}_{2x}$ of depurated acceleration signal in case of Healthy wheel at 10 km/h for a load condition of 1000kg

Figure 3.8 reports the first and second order cyclic cumulants in case of healthy wheels while Figure 3.9 for a MA faulty wheel. Moreover Figure 3.10 reports the first and second order cyclic cumulants for a LR faulty wheel and Figure 3.11 for a DR faulty wheel. For each figure a zoom in the first 10 orders is also given representing the most significant signal contents range. Moreover, Tables 3.7 and 3.9 report the cyclostationarity indicator values in the case of healthy and faulty wheels, respectively.

Regarding the first cyclic order cumulant, it is interesting to note the presence of a high first order component and subsequent harmonics in the case of

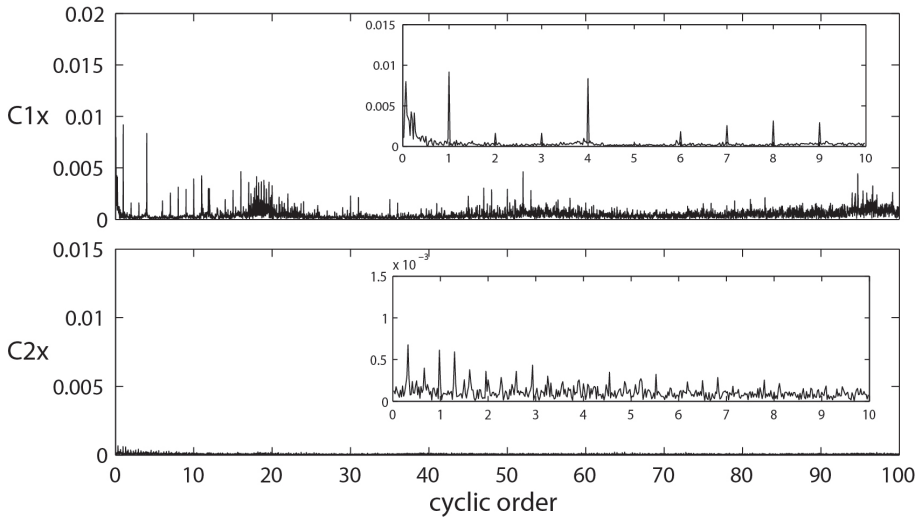

Figure 3.9: $\hat{C}^{\alpha}_{1x}$ and $\hat{C}^{\alpha}_{2x}$ of depurated acceleration signal in case of MA faulty wheel at 10 km/h for a load condition of 1000kg

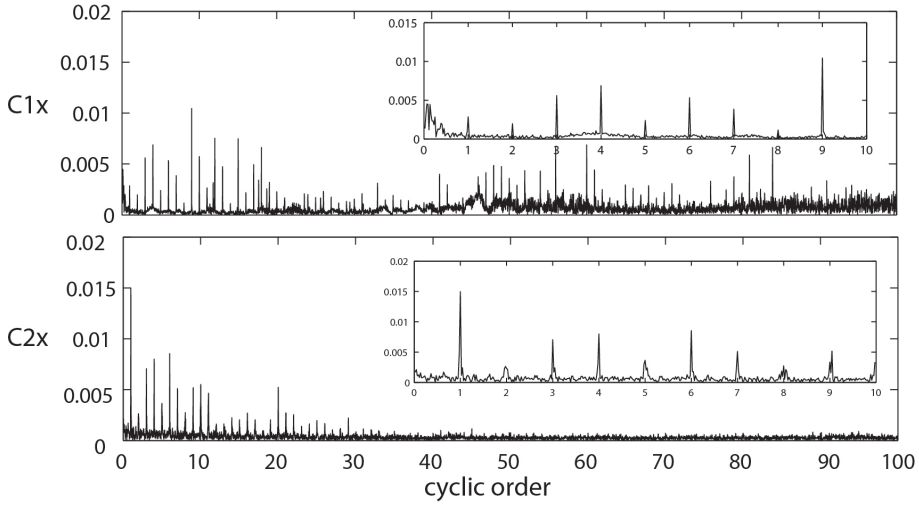

Figure 3.10: $\hat{C}^{\alpha}_{1x}$ and $\hat{C}^{\alpha}_{2x}$ of depurated acceleration signal in case of LR faulty wheel at 10 km/h for a load condition of 1000kg

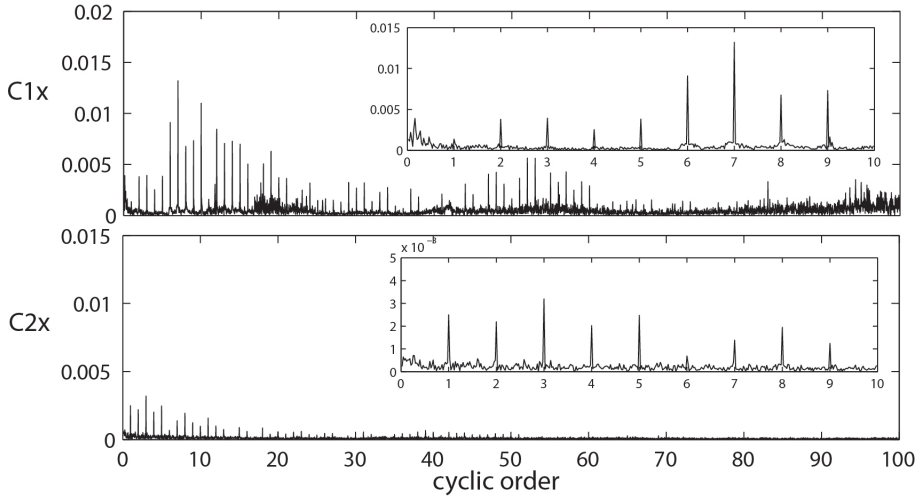

Figure 3.11: $\hat{C}^{\alpha}_{1x}$ and $\hat{C}^{\alpha}_{2x}$ of depurated acceleration signal in case DR faulty wheel at 10 km/h for a load condition of 1000kg.

a localized defect of missing adherence (MA) with respect to the healthy condition. In the case of localized and distributed rust defects (LR and DR) the main differences from the healthy case are registered in both the first and in the second order cyclic cumulant. First-order cyclostationary components characterise the deterministic behaviour of a system which are usually linked with macro-phenomena that perfectly repeat themselves on a cyclic basis. This is typically the case of vibrations due to unbalance, misalignment, eccentricity, run-out, meshing, etc.

On the other hand, pure second-order cyclostationarity components characterise the random behaviour of a system which are usually linked with hardly predictable micro-phenomena. This is typically the case of vibrations due to fluid flows, frictions, rubs, etc. It will be possible to understand in detailed the reason of the second order ciclostationary nature of the signal in Chapter 5, through the modelling diagnostics support.

As done for the statistical parameters, the Tukey's method has been applied to the $ICS1x$ and $ICS2x$ metrics evaluated for the group of 15 healthy wheels

(Table 3.8) in order to identify the threshold pass/fail values. Possible faults can occur for values between 0.0893 and 0.1226 in the case of $ICS1x$ and for values between 0.0167 and 0.208 for $ICS2x$ metrics. Moreover assured faults can occur for values exceeding to 0.1226 and 0.0208 for $ICS1x$ and $ICS2x$, respectively. The comparison between the results in Tables 3.9 and 3.8 leads the following remarks, highlighted in Figure 3.12:

- the $ICS1x$ parameter is able to detect only two certain faults ($LR1$ and $DR2$). Nevertheless this low monitoring skill is not really representative for the real differences between healthy and faulty wheels, as it clearly appears looking at the first order cumulants of Figures 3.9, 3.10 and 3.11. The main reason of this apparent discrepancy between the monitoring capability of the first cyclic order cumulant and its indicator is due to the large value of dispersion characterizing the healthy wheel, which causes a large increase of the threshold level.

- the $ICS2x$ is able to recognize the presence of anomalies or of possible anomalies for all the known faulty wheels, in the case of both missing adherence and rust defect. In case of healthy components, the $ICS2x$ values do not present this dispersion effect so, as a result, the $ICS2x$ monitoring skill is particularly sensitive to fault recognition.

Table 3.7: $ICS1x$ and $ICS2x$ values for the 15 healthy wheels at the "best" test conditions

Healthy wheels (HW)	ICS_{1x}	ICS_{2x}
HW1	0.0282	0.0105
HW2	0.054	0.01
HW3	0.047	0.0123
HW4	0.0338	0.0044
HW5	0.054	0.0092
HW6	0.0382	0.0072
HW7	0.027	0.0127
HW8	0.1	0.0126
HW9	0.062	0.0135
HW10	0.048	0.014
HW11	0.0328	0.015
HW12	0.0557	0.0103
HW13	0.062	0.012
HW14	0.056	0.01
HW15	0.046	0.0122

Table 3.8: $ICS1x$ and $ICS2x$ threshold values obtained using the Tukey method at the "best" test conditions

Healthy wheels (HW)	ICS_{2x}	ICS_{2x}
Q1	0.0338	0.01
Q2	0.0480	0.012
Q3	0.056	0.0127
$Q3 + 1.5\|Q3 - Q1\|$	0.0893	0.0167
$Q3 + 3\|Q3 - Q1\|$	0.1226	0.0208

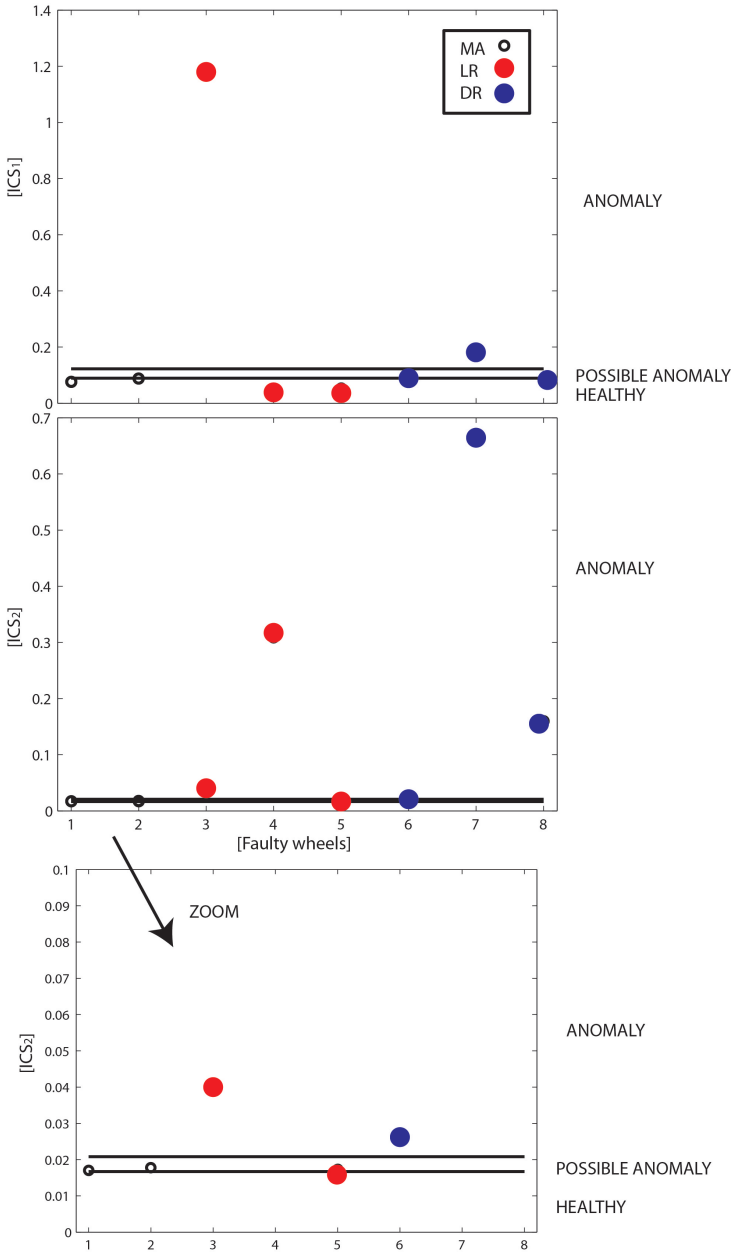

Figure 3.12: $\hat{C}^{\alpha}_{1x}$ and $\hat{C}^{\alpha}_{2x}$ pass-fail distributions in case of MA, LR and DR defects

Table 3.9: $ICS1x$ and $ICS2x$ values for a group of 8 different faulty wheels at the "best" test conditions.

Faulty wheels	ICS_{1x}	ICS_{2x}
MA1	0.076	0.017
MA2	0.0884	0.0178
LR1	1.175	0.04
LR2	0.0257	0.3088
LR3	0.052	0.0173
DR1	0.0869	0.026
DR2	0.168	0.671
DR3	0.083	0.16

3.5 Diagnostics

The CWT has been applied to signal $SAw(\theta)$ in the angle domain, where $\theta = tf_r$ with the wheel rotation frequency f_r. Thus the CWT is computed as:

$$CWT(a,b) = \frac{1}{\sqrt{a}} \int_{-\infty}^{+\infty} SAw(tf_r)\psi^* \left(\frac{t-b}{a}\right) dt \tag{3.5}$$

In this work the impulse mother wavelet is used due to the impulsive peculiarity of the signal:

$$\psi(t)_{impulse} = \sqrt{2\pi} e^{2\pi j f_0 t - |2\pi t|} \tag{3.6}$$

where f_0, the central frequency of the mother wavelet, is taken equal to 20 Hz. The result of the CWT is graphically represented in the time-scale plane, while in this thesis the maps have been displayed in the rotation angle-order domain, using the relationship $ord = f_0/(af_r)$ between the central frequency of the analyzing wavelet f_0, the scale a and the rotational frequency f_r; the rotation angle is equal to bf_r. Moreover, when complex analyzing wavelets have been used,

only the amplitude will be considered and represented using a linear scale Figure 3.13 reports the Wavelet Transform for each faulty wheel type (MR, LR and DR) and for an healthy wheel at the "best" test condition. This latter does not exhibit any particular order contents in the order range of interest. On the contrary, the localized defect of missing adherence produces peaks mainly characterized by an order contents between 10 and 20 depending on the dimension of the defect. Localized and distributed rust are characterized by a further order contents between 45 and 80 orders. The reason for the different order contents depending on the defect type will be described in Chapter 5 through the model diagnostics support.

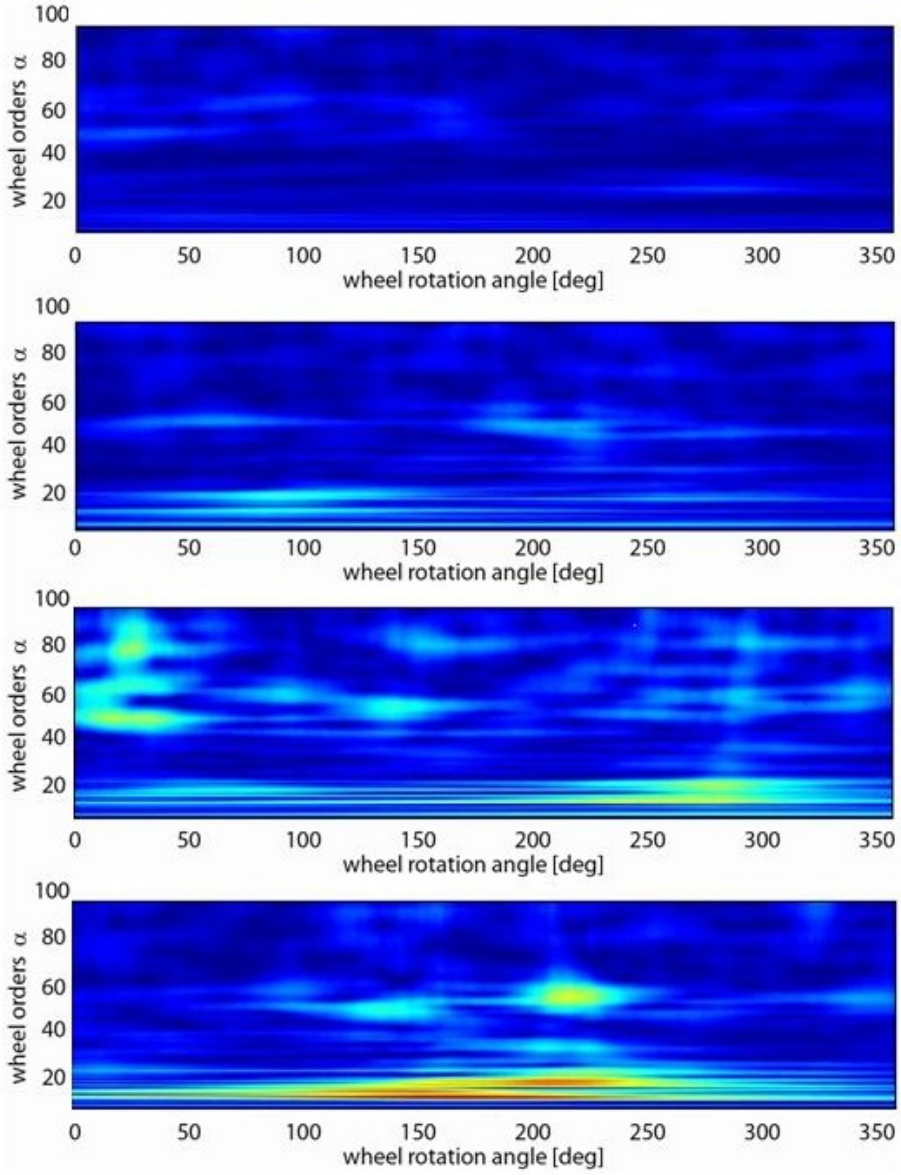

Figure 3.13: Wavelet Transform of acceleration signal at the “best” test condition for a) Healthy wheel, b) MA faulty wheel, c) LR faulty wheel and d) DR faulty wheel

3.6 Proposed algorithm for on-line monitoring and diagnostics

A schematic algorithm of a possible procedure to be implemented in a condition monitoring and diagnostics station at the end of the production line is here presented and discussed.

The proposed algorithm (see Figure 3.14) takes advantage of the monitoring capacity of the different metrics, the threshold values estimated by the Tukey's method and the dagnostics skill of the wavelet technique. In particular, starting from a raw acceleration signal, firstly the Kurtosis parameter of the SAw is estimated and compared with the threshold values of Tukey's method in order to recognize the presence of defects with large dimensions. It has been discussed in Section 3.4 that only quite large defects can be found by such a comparison. The RMS values of the SAw signal and the relative thresholds should be used in order to detect other defects.

If both the Kurtosis and RMS values are smaller than the relative threshold values, then the second order cumulant of the residual signal and its indicator should be introduced. If the ICS_{2x} values are lower than the thresholds, the wheel can be considered definitely healthy.

The proposed algorithms is able to detect all the adherence anomalies due to missing glue or rust presences of the tested wheel. However, before implementing the algorithm in a test station, it will be validate on additional wheels, extracted directly from the production lines.

If during the monitoring phase, a defect is detected, the defect type is recognized through the analysis of the wavelet calculated on the SAw signal, in the diagnosis phase. The presence in the wavelets of order contents of about 10-20 orders is addressed to localized missing adherence defects, while for rust defects there should be a further order contents around 60-80.

In Chapter 6, the reason for the different techniques's efficiency will be described more in detail.

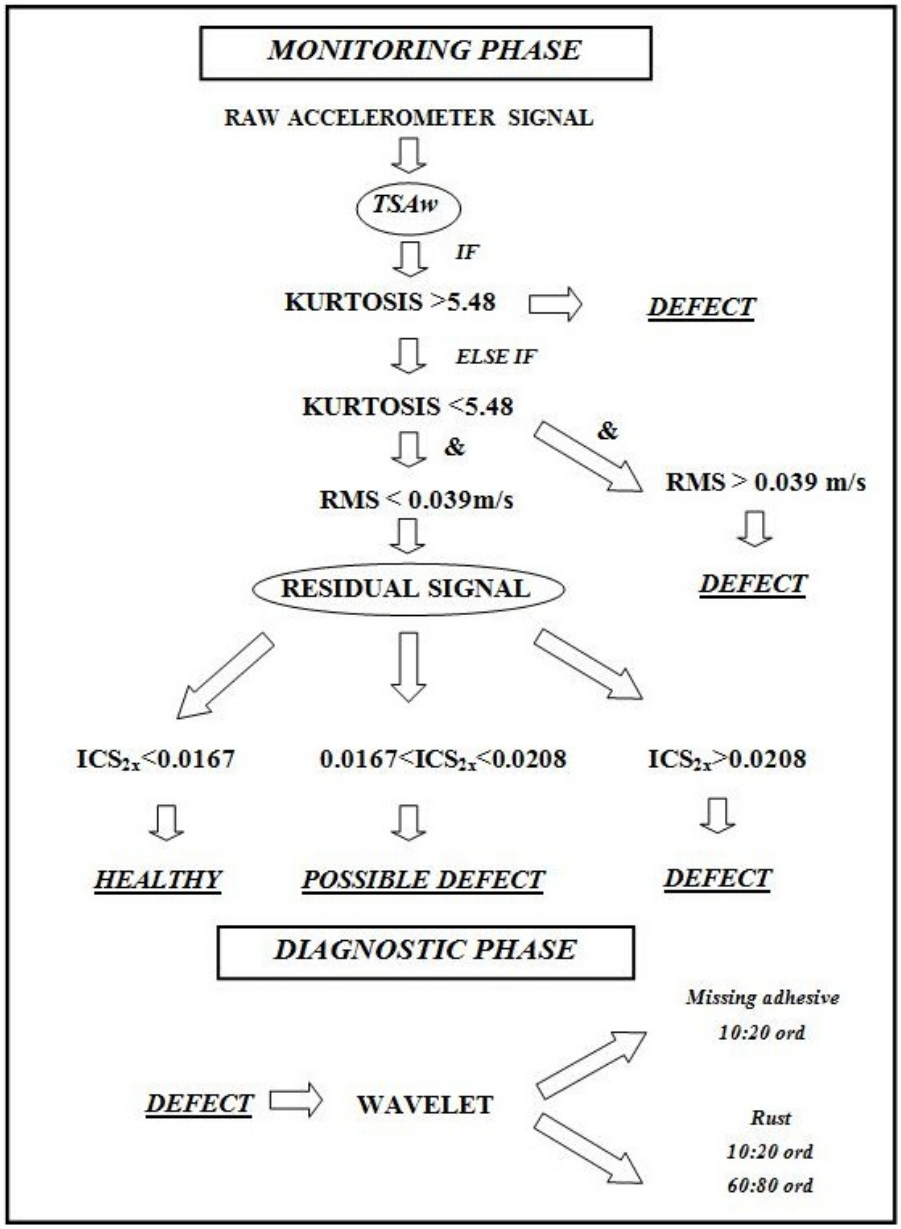

Figure 3.14: Proposed monitoring and diagnostic algorithm for heavy-duty wheel

3.7 Intermediate results

This activity has brought to draw the following conclusions:

- the acceleration signal gives the clearest response in case of anomalies localized in the tread-hub interface;
- the operational test condition of 4km/h (low speed) and 1000kg (high load) best highlights the fault presence;
- the Kurtosis and RMS coefficients estimated on the SAw, in cooperation with ICS1x and ICS2x indicators applied to the residual signal are useful metrics for the definition of the state of health of the wheel, i.e. detection of missing adherence and localized-distributed rust defects;
- The Continuous Wavelet Transform makes it possible to identify common order contents for similar defect types.

Chapter 4

System dynamic characterization

4.1 What is the chapter about?

This chapter aims at evaluating the effect of the wheel dynamics on the measured acceleration signal.

It has been found that all the acceleration signals analyzed in Chapter 3 present a main spectrum content in the frequency range between 0-100 Hz. Figure 4.1 reports the case of a typical missing adherence defect spectrum.

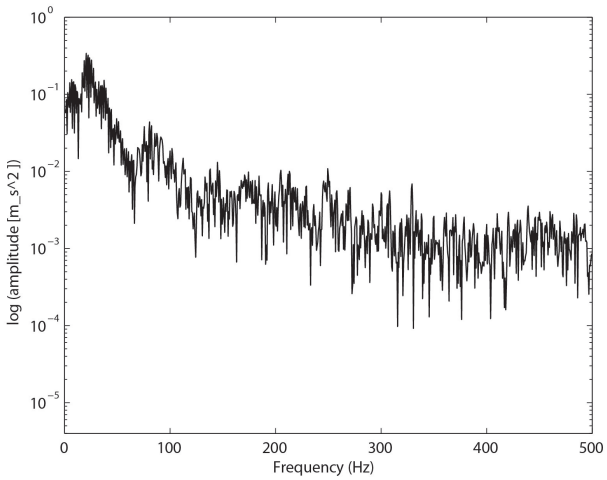

Figure 4.1: Acceleration spectrum in the case of missing adherence defect

The main question that needs to be solved is:

- Can a heavy-duty wheel be considered as a rigid body in this frequency range?

4.2 Introduction

The knowledge of the system dynamic characteristics in the real operating condition represents a fundamental but in the main complicated task: the most popular approach adopted under the hypothesis of system linear behavior is given by the modal analysis theory. The linearity assumption entails that the frequency response functions should be independent of the excitation level. This is normally true for low energy excitations. As a result, the system dynamics can be described by a set of linear, second order differential equations. However, linear analysis can be insufficient to describe the behavior of the physical system since totally unexpected phenomena sometimes occur, phenomena that are not predicted or even hinted at linear theory [31]. In structural dynamics a classical source of non linearity is represented by non-linear material behavior: viscoelastic material is a typical example [56–58].

Young's Modulus and damping properties in the case of viscoelastic materials are dependent on several factors such static load, temperature, deformation amplitude and frequency. Consequently, the dynamics of a component made of viscoelastic material can vary depending on the applied operational conditions.

The pertinence of the linearity hypothesis has to be established through a characterization of the material linearity level. This analysis consists of the measurement of the material complex moduli (the dynamic modulus, the loss modulus and the loss factor, frequency dependent) through a so called "Direct method" [34, 38] .

The complex modulus concept is a powerful, widely used tool for characterizing the dynamic elastic and damping properties in the frequency domain [31, 33–35] . In case the test campaign highlights a slight material non linearity in the operational condition range, it is possible to adopt modal analysis

techniques for the system dynamic characterization.

Furthermore, the material test campaign allows to determine the well suited material model to be adopted in system modelling.

In section 4.3, a theoretical procedure to dynamically characterize a mechanical component made of viscoelastic material is described. Moreover, an overview of the theory behind the experimental techniques adopted in the material dynamic characterization is presented. Furthermore in section 4.4 the different phases related to the heavy-duty wheel dynamic characterization are described.

4.3 A procedure to dynamically characterize a viscoelastic material component

In general, viscoelastic material properties are mainly dependent on frequency, static load, dynamic deformation and temperature. In order to establish the material dependency on these factors, it is necessary to experimentally analyze a material sample through laboratory tests. As a result, it is possible to evaluate the material characteristics, obtaining a so-called "material characterization matrix".
Each matrix element is composed of the complex modulus, (the dynamic modulus, the loss modulus and the loss factor, frequency variable), evaluated at a well-defined static load and deformation amplitude. These values can be adopted in different viscoelastic material models, able to represent the material behavior. Indeed, for a successful prediction of the dynamic behavior of a component made of viscoelastic material, it is important to have an accurate mathematical model of the material itself. The "Kelvin-Voigt model" [36] which is a spring and damper in parallel, frequency dependent, is often used for modelling viscoelastic components, defined as follows:

$$\sigma = E' \cdot \varepsilon + E'' \cdot \frac{d}{dt}(\varepsilon) \tag{4.1}$$

where E' is the Young's modulus and E" is the complex modulus representing the viscoelastic material damping properties. The frequency-dependent complex modulus model is an approach which allows the complex modulus to vary as a function of the excitation frequency.

First of all the sample is tested statically: the different load-deformation ranges expressed by a constant stiffness value are defined. Afterwards, the sample is tested dynamically, imposing different static preloads and applying defined deformations, at variable frequencies. The final goal is to obtain a matrix able to cover the deformation range reached by the material component in the normal operational conditions. However, most of the times, due to limitations on the set-up, the entries of the "material characterization matrix" cannot be estimated exactly. Information given by the "material characterization matrix" can be used to:

- verify the material linear behavior at the system operational conditions;

- determine an appropriate material model to be applied in a component finite element model.

If the linearity hypothesis is assured, the finite element model can be verified though modal analysis techniques. Figure 4.2 describes the different steps that should be ideally followed to dynamically characterize a system composed of viscoelastic material, referring to [59].

A first characterization of the static material properties is needed in order to establish the linear deformation ranges [31]. This information will be taken as a reference during the dynamic test in order to avoid the application of static and dynamic load in the thresholds of these ranges. The static methods are normally based on tensile, compression, shear, torsion or indentation tests. A convenient sample is loaded with a prescribed force or deformation, the load (F)/deformation (l) ratio is called stiffness k while the corresponding modulus is yielded by multiplying the stiffness with the ratio of the specimen height h to

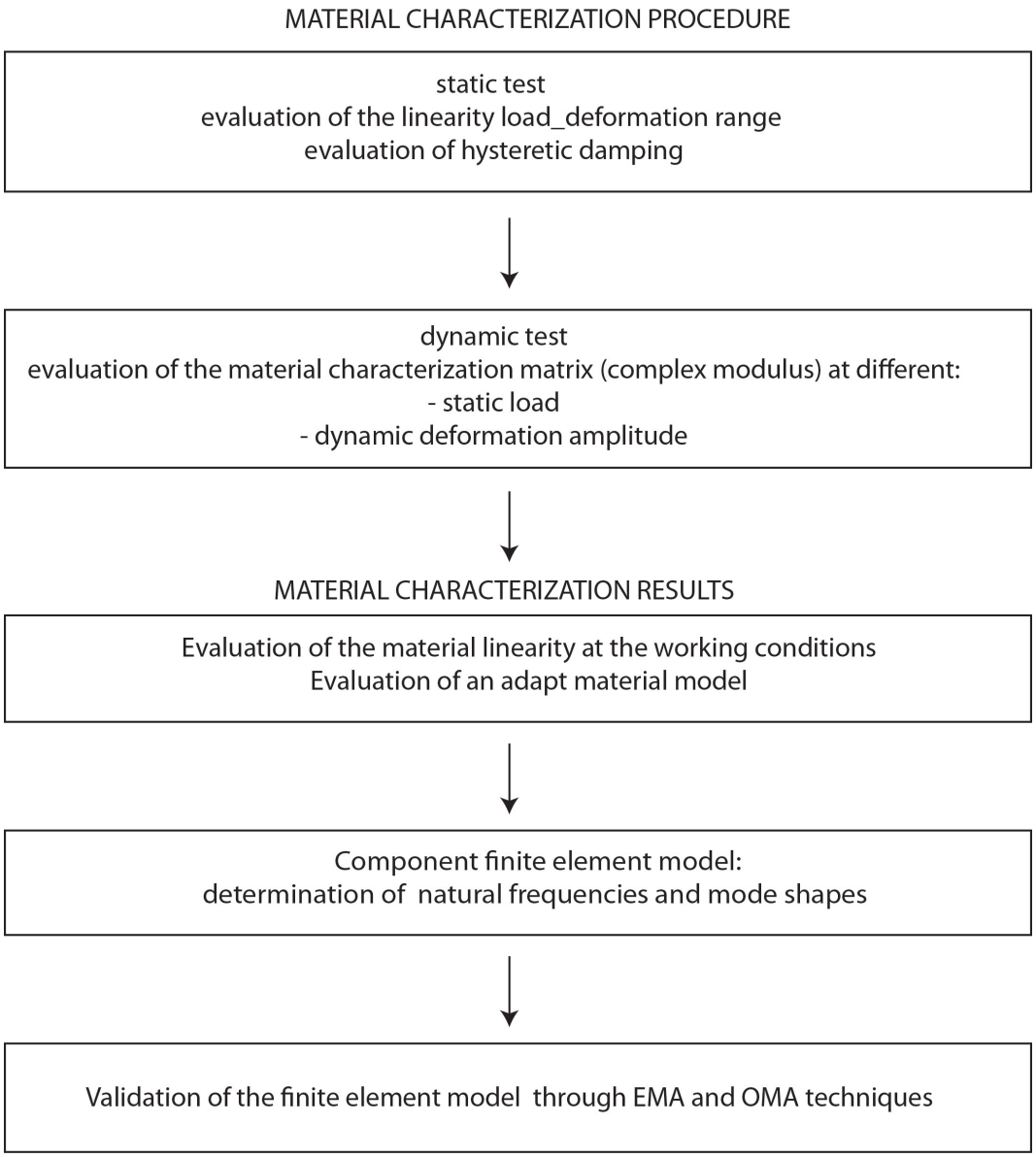

Figure 4.2: Procedure to dynamically characterize a system made of viscoelastic material

its loaded area A:

$$E_a = \frac{\sigma}{\varepsilon} = \frac{F/A}{l/h} = k\frac{h}{A} \tag{4.2}$$

However these values, although used in technical applications, are only mutually consistent when introducing empirical factors for boundary conditions and shape.

In general, the limited dimensions of the samples and the clamping adhesion along the anvils can contribute to introduce further uncertainties. The true modulus is defined as [31]:

$$E_t^{'} = \frac{\sigma_t}{\varepsilon_t} = \frac{\sigma}{\varepsilon} \cdot \frac{(1+\varepsilon)}{\ln(1+\varepsilon)} = E_a \cdot \frac{(1+\varepsilon)}{\ln(1+\varepsilon)} \tag{4.3}$$

The shape factor is the ratio between the loaded surface and the surface which is free to deform:

$$S = \frac{\pi r^2}{2\pi r h} = \frac{r}{2h} \tag{4.4}$$

Many authors have theoretically shown that the ratio between the apparent Young's modulus $E_g^{'}$ measured with end faces glued on the anvils and measured with free gliding and faces $E_f^{'}$ is a function of the shape factor S:

$$E_g^{'} = E_f^{'}\left(1 + 2S^2\right) \tag{4.5}$$

Once the linearity load-deformation ranges are detected, it is possible to dynamically characterize the viscoelastic material: the methodology adopted to study the characteristic of a test sample in laboratory environment is called 'Direct method' [32–34, 34–38]. This technique needs the knowledge of the input force (given by an electro/hydraulic shaker or an hammer) and of the output response given by an accelerometer positioned close to the element under study. In particular, measuring the force $F_u(\omega)$ transmitted over the element for an input

deformation $x_i(\omega)$ at a certain frequency, the transfer function is:

$$\frac{F_u(\omega)}{x_i(\omega)} = (k + jc\omega) \tag{4.6}$$

From this following equalities results:

$$k = \mathrm{Re}\left[\frac{F_u(\omega)}{x_i(\omega)}\right] \tag{4.7}$$

$$cw = \mathrm{Im}\left[\frac{F_u(\omega)}{x_i(\omega)}\right] \tag{4.8}$$

where Re and Im represent respectively the real and the imaginary component of the transfer function . In case the tests are conducted on a material sample of simple geometry of height h and section A, it is possible to directly detect the complex dynamic modulus of the material defined as:

$$E^* = E' + jE'' \tag{4.9}$$

where E' is the Young's modulus defined as:

$$E' = \frac{\sigma}{\varepsilon} = \frac{F/A}{x/h} = \frac{F}{x}\frac{h}{A} = k\frac{h}{A} \tag{4.10}$$

while the loss modulus E" is defined as:

$$E'' = cw\frac{h}{A} \tag{4.11}$$

Generally, the experimental accelerometer signal is used as the response. As a consequence the complex stiffness and the complex modulus are obtained through the frequency response function $\frac{\ddot{x}(w)}{F(w)}$ as:

$$\left(E'(w) + jE''(w)\right) = \frac{h \cdot w^2}{A}\left(\frac{1}{\left(\frac{\ddot{x}(w)}{F(w)}\right)} + m\right) \tag{4.12}$$

Where w is the radial frequency and m is the dynamic mass of the impedance head sensor adopted to measure the acceleration and the force applied.

Once the static and dynamic material properties are detected, it is possible to define an appropriate material model to be used, for example, in a finite element model of the component. The model gives information concerning natural frequencies and mode shapes in free-free and constrained conditions.

A further outcome of material dynamic characterization is the possibility of evaluating the material linearity and consequently its effect on the whole component linearity, at different working conditions. If material linearity is assured, it is possible to experimentally validate the finite element model of the component through modal analysis techniques.

4.4 Heavy-duty wheel dynamic analysis

The heavy-duty wheel, previously analyzed focusing on the diagnostics in Chapter 3, has been dynamically studied. This activity aims at detecting the possible presence of wheel natural frequencies in the frequency range between 0-100 Hz. The obtained results will be used for modelling purposes.
The adopted procedure is summarized in Figure 4.3.

Stage 1

First of all, the polyurethane of the wheel's tread has been statically analyzed. During the test, an oil film has been applied on the sample surfaces in order to reduce the clamping adhesion effect. Different material samples have been statically analyzed, obtaining various load-strain hysteretic curves. Figure 4.4 reports the result of a cylindric sample of 9 mm height and 20 mm diameter. The linearity deformation ranges have been detected, as reported in Tables 4.1 and Table 4.2. These data represent the basis of the successive dynamic material analyses: the preload and deformation amplitudes have been set referring to these linearity ranges.

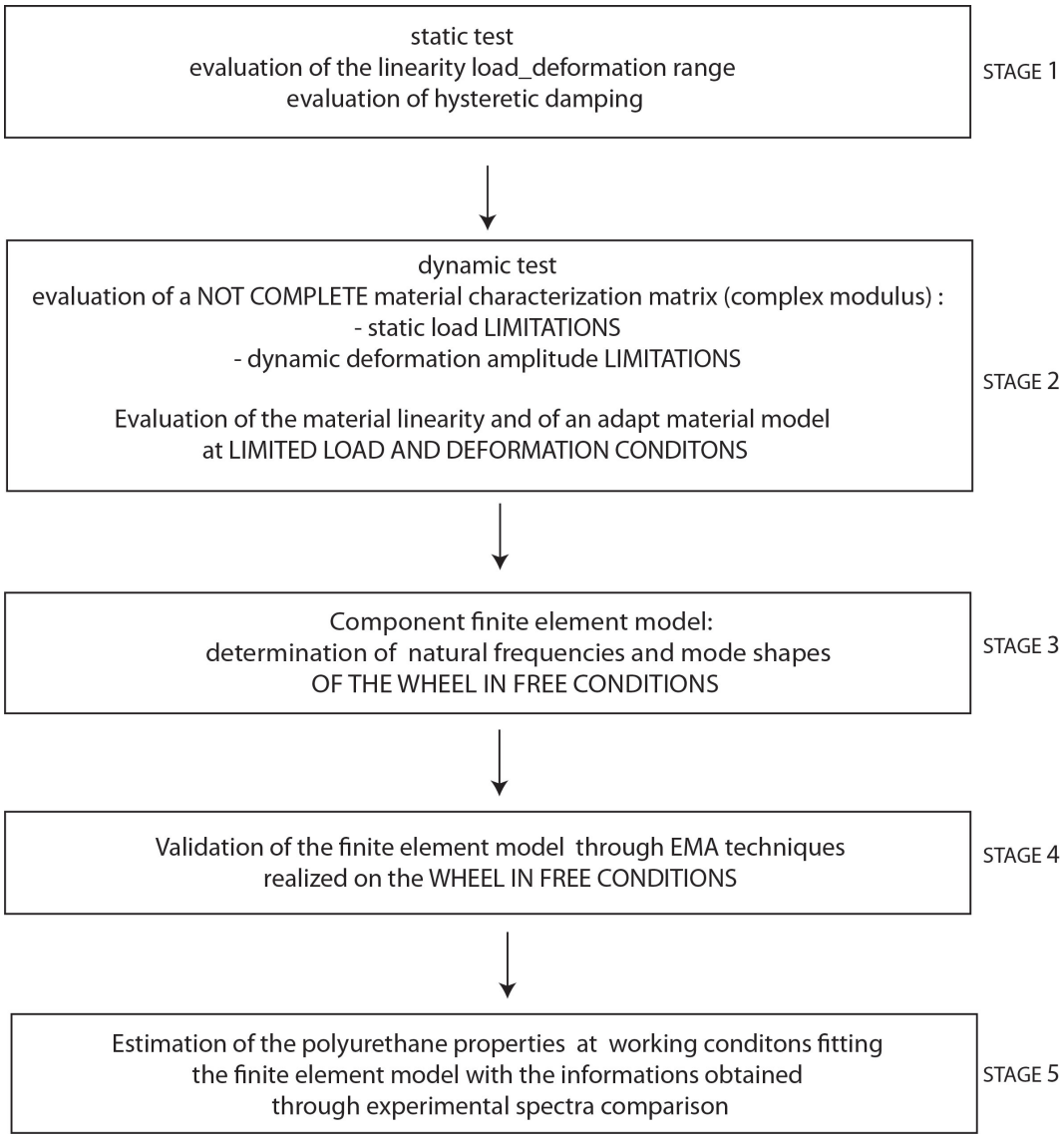

Figure 4.3: Procedure to dynamically characterize the heavy-duty wheel

Stage 2

Once the static characteristic of the material and in particular the linear deformation ranges are determined, test samples have been dynamically ana-

lyzed. The objective is the material complex moduli evaluation at different static preload and dynamic deformations. Two different setups have been used: Figure 4.5 and Figure 4.8.

The first measurement campaign has been conducted at KUL department using a set up already adopted in a previous work [59]. This set up is not able to apply significant preload on the sample. It consists of an electro-dynamic shaker and an impedance head on which the elastomer sample is mounted. The other end of the elastomer sample is clamped to the ground. It is placed as a vertical (hollow) cylinder between the two place holders. The electro-dynamic shaker gives a swept-sine signal varying continuously the frequency in an established range. Acceleration as well as force are processed by means of a Fast Fourier transform while the transfer function is computed through a so called harmonic estimator [60].

Since the impedance sensor is mounted on the shaker, the dynamic mass of the impedance sensor should be compensated for in the force measurement. A test in which no sample is mounted yields the dynamic mass of the impedance sensor. The dynamic mass of the impedance sensor m_{dyn} is measured at 6.10 10^{-3} kg. Figures 4.6 and 4.7 report the Young's modulus and the loss modulus values for a small preload and different dynamic deformations amplitude, obtained through equation 4.12. The measured curves do not cover the same frequency range. The upper frequency for each excitation level is constrained due to the limited power of the shaker. The higher the vibration amplitude, the more power is needed at the same frequency. The lower frequency limit is related to the sensitivity of the impedance sensor. There is a lower limit for the acceleration and force measurement below which the signal to noise ratio becomes too low. These considerations can be simply verified variating the values of A and of $\frac{\ddot{x}(w)}{F(w)}$ in Equation 4.12.

A further set up composed of an electro hydraulic shaker has been used, as shown in Figure 4.8. This force actuator can give a dynamic load and a defined static load. The maximum static load reachable by the test set-up is 160 kg while the maximum displacement is 55 mm peak to peak. Different material

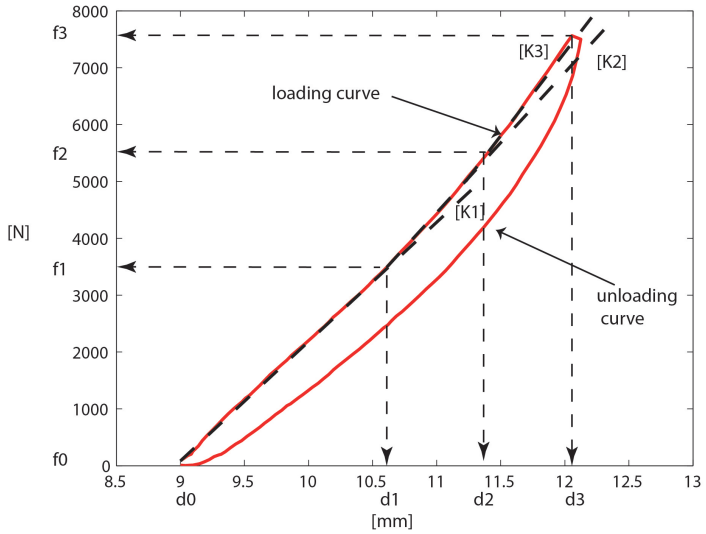

Figure 4.4: Loading-Unloading curve of the sample static test

Table 4.1: Load/deformation discrete curve points

n	dn[mm]	fn [N]
0	9	0
1	10.6	3500
2	11.36	5500
3	12.05	7500

Table 4.2: Variable stiffness

n	δn (mm)	δf (N)	K (N/mm)	E (MPa)
1	1.6	3500	2187	8.57
2	0.75	2000	2631	10.31
3	0.69	2000	2898	11.36

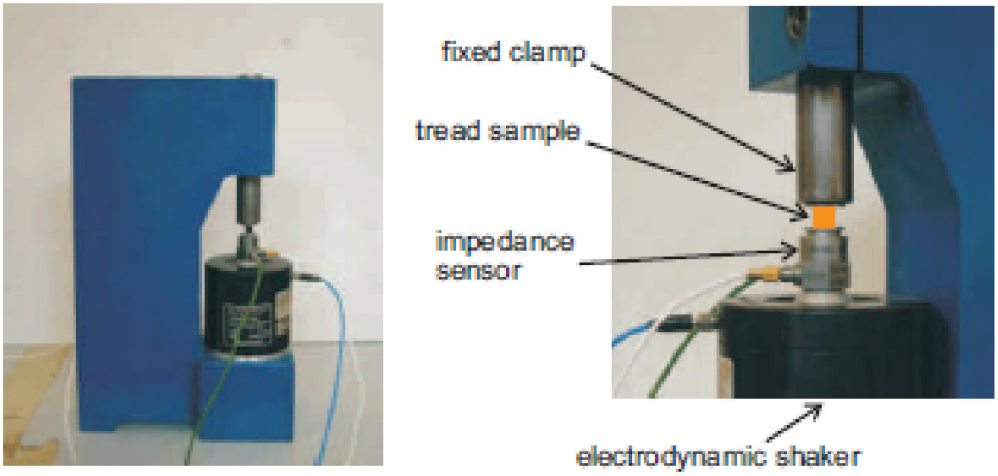

Figure 4.5: Test set up used to dynamically characterize the material behaviour:limited static preload

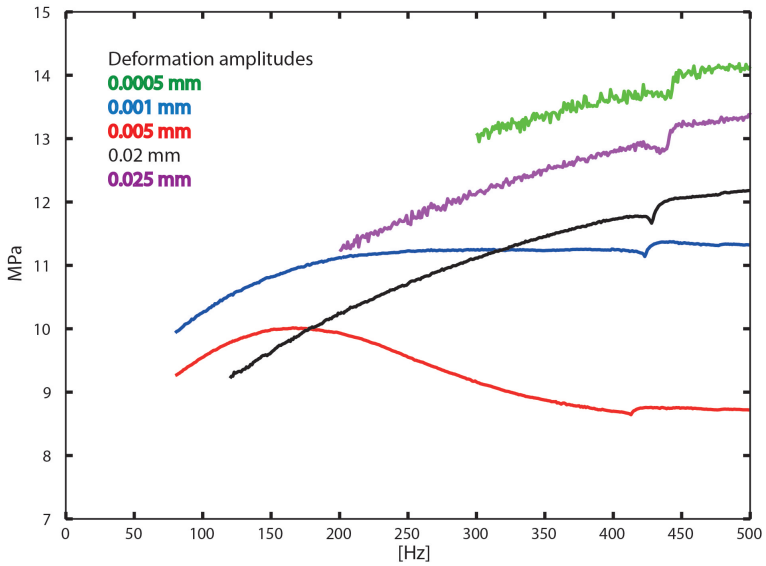

Figure 4.6: Young's modulus for different dynamic deformation amplitudes at a constant small preload

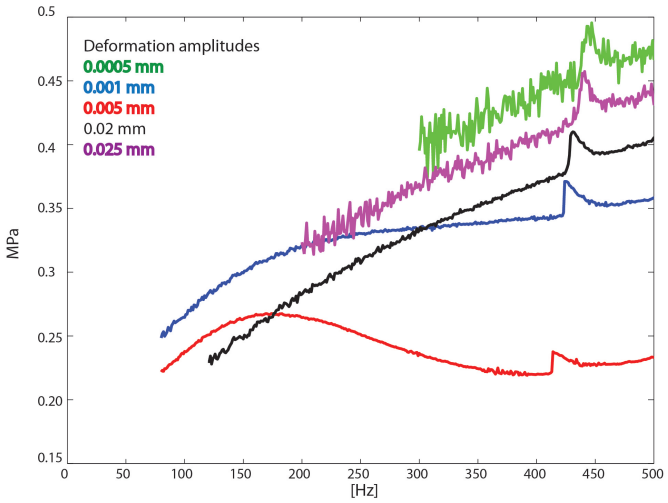

Figure 4.7: Loss modulus for different dynamic deformation amplitudes at a constant small preload

samples have been tested at different preloads, reaching a maximum dynamic deformation of 0.5 mm peak to peak at 200 Hz for a static preload of 590 N.

The results are similar to the ones obtained with the first test set-up, with Young's modulus values varying between 10 and 15 MPa. As highlighted in Figure 4.6, in the case of limited deformations and static loads, the material shows a slight dependency on frequency, preload and deformation amplitude. At these conditions the polyurethane material can be represented through a linear isotropic material model, with a Young's modulus of 12.5 MPa and a Poisson coefficient of 0.49.

Stage 3

Finite element models of the hub and of the complete heavy-duty wheel have been realized, using commercial software. The goal of this stage is the determination of the natural frequency and normal modes of the system in free-free conditions. First of all, a model of the hub has been realized, adopting cast iron property values given by the company. This modelling activity was needed in

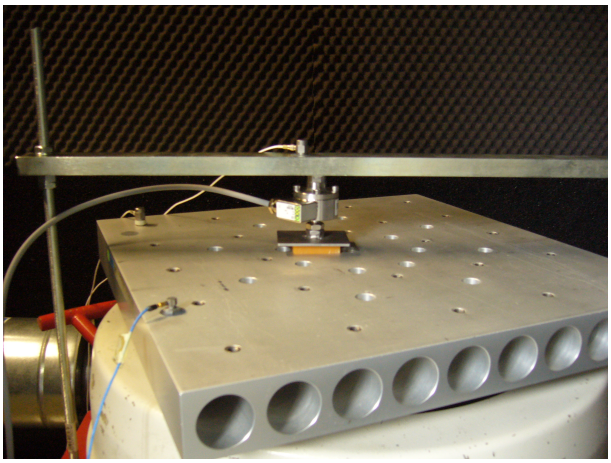

Figure 4.8: Test set up used to dynamically characterize the material behaviour: maximum static preload of 600 N

Table 4.3: Cast iron hub and polyurethane characteristics of the element in free-free conditions

	Material	Young's Modulus [MPa]	Poisson coefficient	Density $[m/s^2]$
Hub	Cast iron	210000	0.25	7200
Heavy-duty wheel	Polyurethane	12.5	0.49	1220

order to reduce the presence of inaccuracies in the whole wheel model. Results are sketched in Figure 4.9. Afterwards, a complete wheel model has been realized. The model is composed of the hub attached rigidly to the tread element. The polyurethane properties evaluated in Stages 2 and 3 have been introduced in the finite element model, as reported in Table 4.3. Results are sketched in Figure 4.10 concerning the three first natural frequencies and normal modes.

Stage 4

The finite element models have been validated experimentally through modal analysis. Experimental modal analysis of the hub and of the wheel in free-free condition has been conducted. The components have been suspended by using

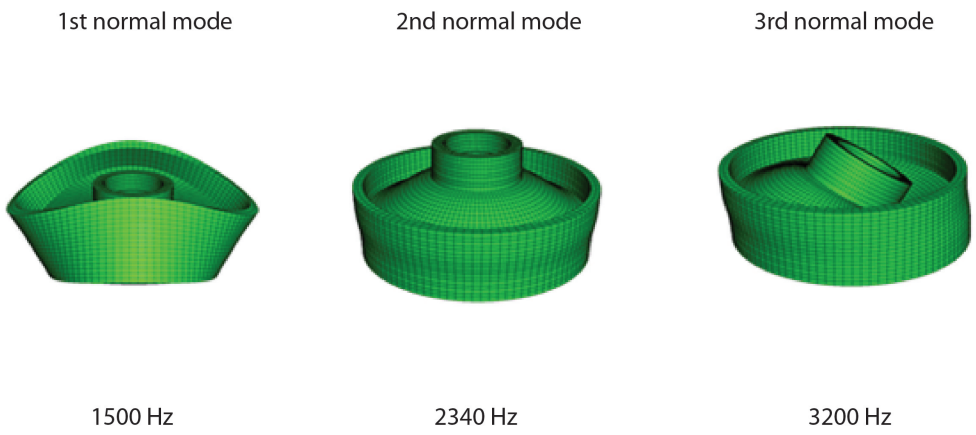

Figure 4.9: Numerical normal modes and natural frequencies of the hub

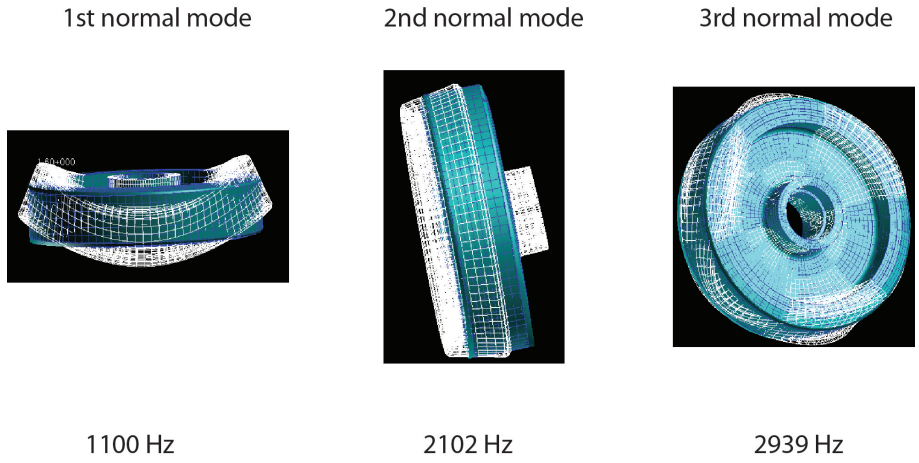

Figure 4.10: Numerical normal modes and natural frequencies of the heavy-duty wheel

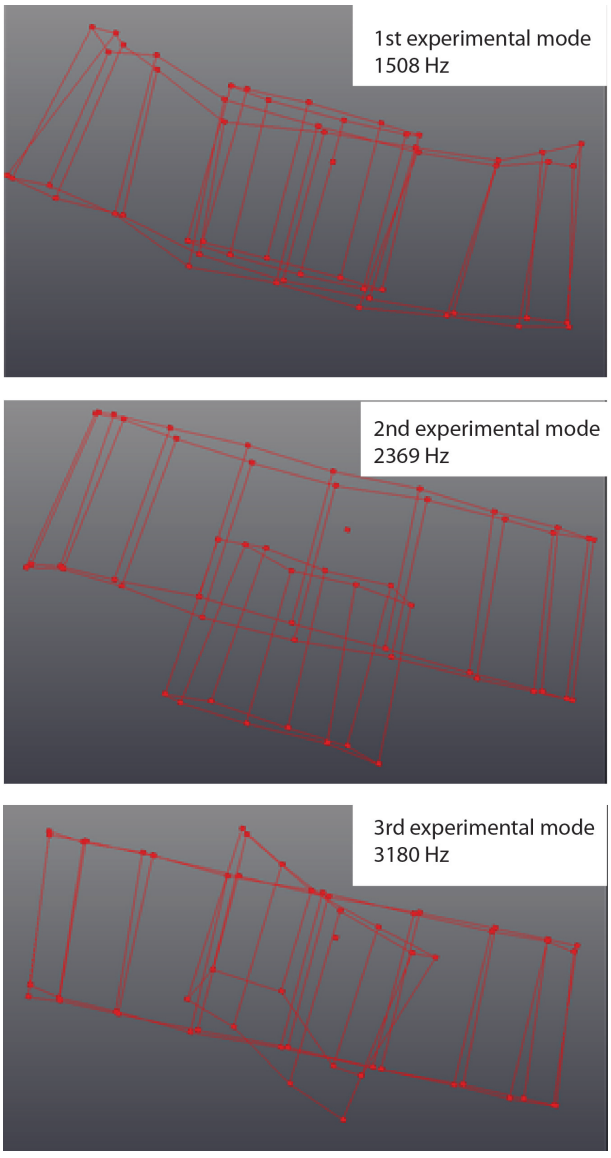

Figure 4.11: Experimental normal modes and natural frequencies of the hub

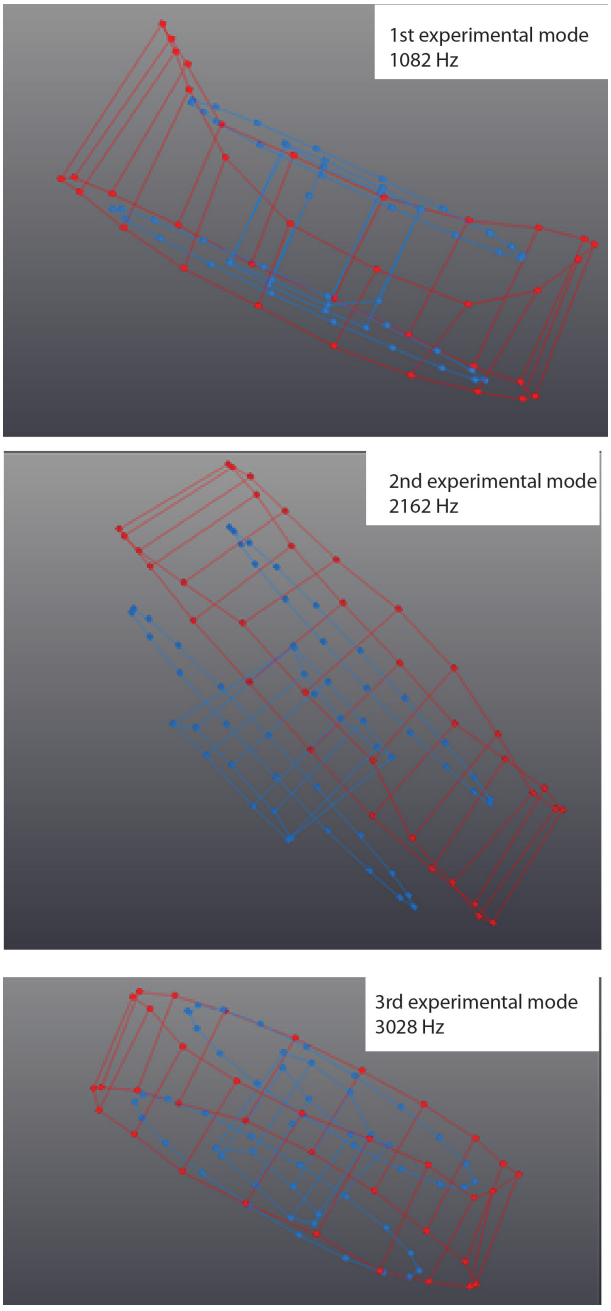

Figure 4.12: Experimental normal modes and natural frequencies of the heavy-duty wheel

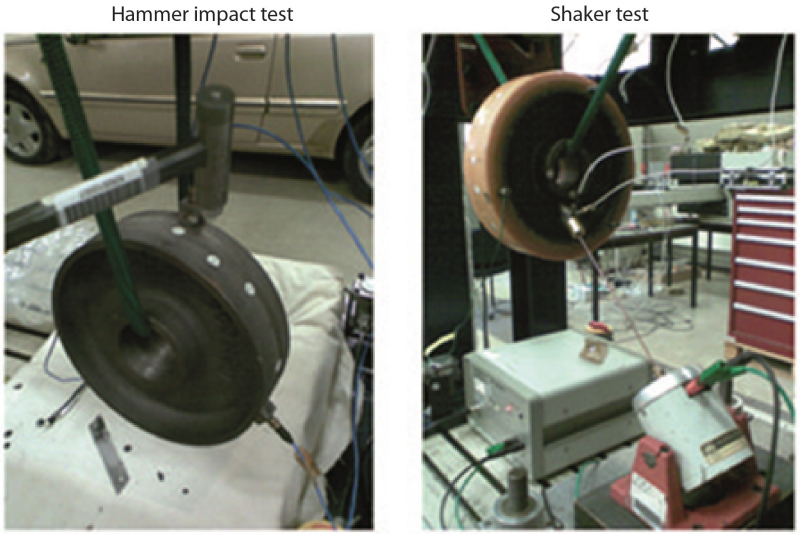

Figure 4.13: Experimental modal analysis setups

Table 4.4: Comparison between FEM and EMA natural frequencies for the Hub case.

Hub	1st [Hz]	2nd [Hz]	3rd [Hz]
Model	1500	2340	3200
EMA	1508	2369	3180

elastic wires. Three accelerometers have been positioned in different points of the structures while two different excitation instruments have been used, as shown in Figure 4.13. Roving hammer impact and shaker tests have been conducted, giving similar results. As highlighted in Figures 4.11 and 4.12 and resumed in Tables 4.4 and 4.5, the numerical results fit quite well with the experimental data.

Stage 5

The finite element model of the wheel in constrained condition (connected to the shaft and in contact with the drum) has been realized, as depicted in Figure

Table 4.5: Comparison between FEM and EMA natural frequencies for the heavy-duty wheel case

Heavy-duty wheel	1st [Hz]	2nd [Hz]	3rd [Hz]
Model	1100	2102	2939
EMA	1082	2162	3028

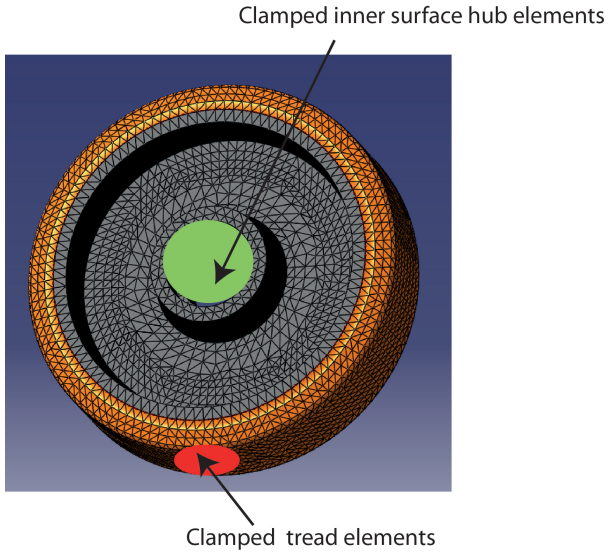

Figure 4.14: Finite element model of the wheel in constrained condition

4.14. Due to the material properties being unknown at the loading operational condition of 1000 kg forces, as first attempt, the same polyurethane properties of the free-free case, i.e. Young's modulus of 12.5 MPa and 0.49 Poisson coefficient. The obtained data are reported in Table 4.6.

In order to verify the level of imprecision given by the previous assumption, the finite element model results have been compared to experimental data. A different approach to the traditional OMA technique has been adopted.

Two different wheels have been considered: a first wheel, namely "yellow wheel", i.e. the wheel analyzed in chapter 3 and whose static and dynamic material properties are known from the previous analysis (Figure 4.4 and Figure 4.6) and a second wheel, namely "green wheel", made of a different polyurethane material but with the same mass.

The signal coming from an accelerometer positioned on the wheel supports has been taken as reference. The two wheels have been tested on the same test set-up and at the same operational conditions of 4km/h and 100kg. Moreover, a cleat obstacle has been fixed on the drum surface, giving a strong excitation, when impacting against the wheel. A comparison of the acceleration spectra at two different frequency ranges is depicted in Figure 4.15. It can be noted that the spectra are almost similar up to 200 Hz, showing peaks at the same frequencies. On the contrary around 800-900 Hz, the spectra appear to be shifted with approximately 50 Hz. The "yellow wheel" shows a spectrum peak around 850 Hz while the green wheel around 900 Hz. Since the unique system difference is related to the tread material, it is possible to consider the two shifted peaks in the spectra as the corresponding wheel natural frequencies.

Consequently, the finite element model of the wheel has been updated in order to obtain a first natural frequency around 850 Hz. The Young's modulus value that enables to fit numerical and experimental data is 18 MPa, as summarised in Table 4.7. This approach will be verified in the future realizing a traditional OMA, after having experimentally verified the material linearity at higher loads.

In conclusion, the numerical and experimental results gave significant infor-

mation about the absence of wheel dynamic effect in the frequency range of interest, i.e. the frequency range up to 100 Hz, as it clearly appears in Figure 4.15. This is confirmed by the two acceleration signals of the different tested wheels that show the same frequency contents up to 100 Hz in case of impact against a cleat obstacle.

Table 4.6: FEM results for the heavy-duty wheel case in constrained condition considering a Young's modulus of 12.5 MPa

Clamped heavy-duty wheel	1st [Hz]	2nd [Hz]	3rd [Hz]
Model	660	760	765

Table 4.7: FEM results for the heavy-duty wheel case in constrained condition considering a Young's modulus of 18 MPa

Clamped heavy-duty wheel	1st [Hz]	2nd [Hz]	3rd [Hz]
Model	850	1120	1280

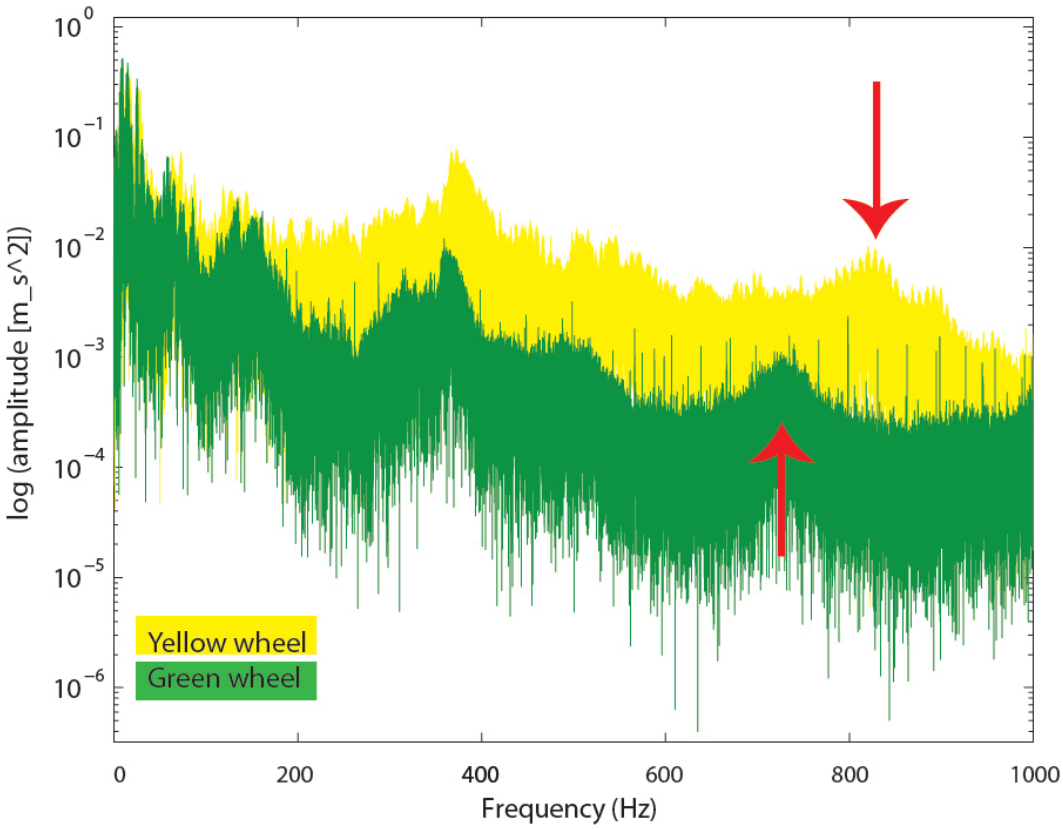

Figure 4.15: Spectrum comparison of the yellow and green wheel impacting against a cleat obstacle at the test conditions of 4km/h and 1000kg

4.5 Intermediate results

In this chapter, the heavy-duty wheel was dynamically studied. First of all, a procedure for dynamically characterizing a component made of viscoelastic material is reported, highlighting the main problems that can be encountered. Concerning the heavy-duty wheel, its dynamic response was analyzed in different stages:

- analysis of a material tread sample through static and dynamic tests: determination of material characteristics (material characterization matrix) such as Young's modulus and damping, at limited preloads and deformation amplitudes;
- in the case of limited deformations and static loads, the material shows a slight dependency on frequency, preload and deformation amplitudes: in these conditions the polyurethane material behavior can be represented as a linear isotropic material model;
- the linear isotropic material properties were inserted in a finite element model, representing the wheel in free-free condition;
- the model results were compared with the data obtained by experimental modal analysis conducted on the hub and on the complete wheel: good correspondence between numerical and experimental results were registered;
- the material characteristics in real operational conditions were obtained updating the finite element model with data coming from the experimental data. Two wheels with the same mass but different tread material were tested in the same set up and test conditions. The acceleration spectrum due to the impact against a cleat obstacle highlights a first peak approximately around 850 Hz, corresponding to the first wheel natural frequency.

- The wheel can be considered as a rigid body up to around 800 Hz. In fact, the peaks that are presented in the spectrum up to 200 Hz are not to the flexible modes of the wheels, but they are due to the rigid modes of the testing machine components to which the wheel is mounted. These latter modes will be shown in the following chapter by using a rigid multibody model.

Chapter 5

Heavy-duty wheel multibody model

5.1 What is the chapter about?

This chapter aims at describing the effect of a missing adherence anomaly via analytical and multibody approaches.

The questions that have to be solved are:

- is it possible to give a physical explanation of the vibratory level measured in the case of a missing adherence defect?
- is the measured signal influenced by operational conditions and defect size?
- is it possible to reproduce the missing adherence signal through a multibody rigid model?
- does the model enable understanding of the experimental monitoring and diagnostics results?

5.2 Introduction

A simplified representation of the contact patch section is proposed, in the cases of both healthy and faulty components, based on the “Brush model” developed by “Pacejka” [61].

Subsequently, a multibody model of the heavy-duty wheel is presented: this model considers the tread as rigid and the yielding part is focused in the contact patch. The value of stiffness and damping are experimentally investigated through static tests conducted on the wheel. The model is validated, comparing numerical and experimental signals in the case of wheel impact against a cleat obstacle. Then the effect of a missing adherence defect is evaluated.

In section 5.3 a preliminary description of the phenomena that are presented in the tyre contact patch are described. Subsequently, in section 5.4 and 5.5 this modelling approach is applied to the heavy-duty wheel in both cases of healthy and faulty components.

In sections 5.6 and 5.7, considerations about operational condition effects (speed and load) and defect size on the measured signal in both time and frequency domains are reported.

Subsequently in sections 5.8 and 5.9, a multibody model, representing the heavy-duty wheel rotating on a circular drum, is described such as the main multibody modelling basis. Simulated acceleration and experimental signals are compared to highlight the adequacy of the diagnostics model.

Finally, considerations about possible developments needed to improve the model's potential are reported.

5.3 The "Brush model"

The "brush model" or "elastic foundation model", proposed by Pacejka in [61], describes the forces and relative displacements between tread/carcass surfaces in the contact patch. The tread deforms due to the normal load and makes contact on the ground over a non-zero footprint area, namely the "contact patch". The tread has been considered as composed of different elements modelled as a series of independent springs that undergo longitudinal deformations and resist with a constant longitudinal stiffness.

In the following the case of the tyre rotating on a moving drum under a certain applied load is explained in detail.

Figure 5.1 depicts the tyre structure and in particular the positions of points A (part of the tread in contact with the ground) and point B (part of the tread in contact with the carcass).

When the tyre rolls on the ground, the portion of the tread that passes in correspondence of the contact patch is subjected to a deformation. In this area, normal and tangential forces are generated, as simplified in Figure 5.2.

Pacejka analyzes each single tread element behaviour. In order to simplify the comprehension, Figure 5.3 and Figure 5.4 depict simplified sketches of an element i at the two instants before and during the insertion in the contact patch.

When point A (point of the i -element on the tread surface) comes in the contact patch area, the presence of a contact patch region can be supposed where the tread elements do not slide with respect to the drum (called “static region”). As the wheel rotates and the tread element enters the contact patch, its tip (Point A) in contact with the ground must have V_x velocity (the velocity of the drum), as described by the equation:

$$V_A = V_x = R_A \cdot \Omega \tag{5.1}$$

In the mean time, the i -element tip in contact with the carcass surface (B point) has V_B velocity defined as:

$$V_B = R_B \cdot \Omega \tag{5.2}$$

Assuming that the brush element i comes in contact with the drum at time t=0, point A and B positions can be defined either by the element upper point (X_B, attached to the carcass) or by its lower point (X_A, the contact to the road), as clearly shown in Figure 5.4 :

$$x_A = a - \int_0^t \Omega R_B dt \tag{5.3}$$

$$x_B = a - \int_0^t V_x dt \tag{5.4}$$

Due to the different velocities of points A and B, a deformation of the element is expected, defined as (5.5):

$$\delta_i = x_A - x_B = \int_0^t V_x - \Omega R_B dt = \int_0^t V_{sx} dt \tag{5.5}$$

If constant velocities are assumed, equation (5.5) together with equations (5.3) or (5.4) give:

$$\delta_i = \frac{V_{sx}}{\Omega R_B}(a - x_B) = \frac{V_{sx}}{V_x}(a - x_A) \tag{5.6}$$

where V_{sx}/Ω is the longitudinal slip denoted σ_x.
Rubber does not necessarily deform linearly, but if approximated in that way, the force needed to achieve the amount of deformation given in (5.5) is then:

$$F_t = k_t \delta_i \tag{5.7}$$

where k_t represents the "material longitudinal stiffness".
The element deformation is limited by the friction between tyre and road. As a result, the maximum force acting on the brush element is given by:

$$F_{t,\max} = \mu F_{zi} \tag{5.8}$$

where μ can be further defined as

$$\mu = \frac{b}{R} \tag{5.9}$$

and where b is the distance of the reaction normal force from the centre of the contact patch while R is the rolling radius, as depicted in Figure 5.2.
Considering equation (5.7) and (5.8) together, the maximal deformation $\delta_{i,\max}$

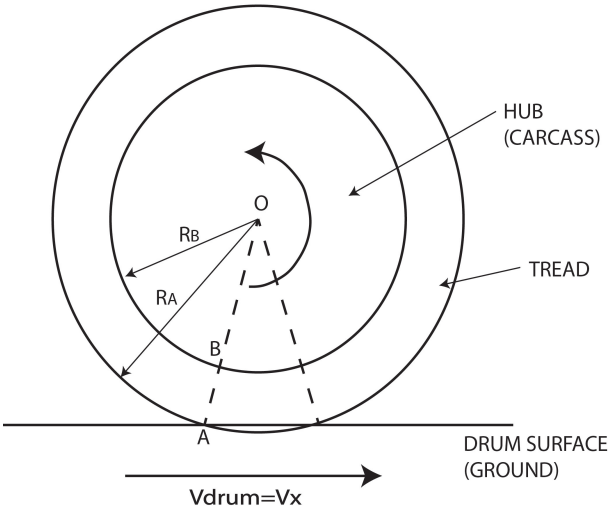

Figure 5.1: Tyre elements

can be expressed as:

$$\delta_{i,\max} = \frac{\mu F_{zi}}{k_t} \tag{5.10}$$

The same formulation can be obtained starting from the concept of "rolling resistance moment". In order to maintain the tyre in rotation, it is necessary to overcome a moment, called "rolling resistance moment", defined as:

$$M_R = F_t \cdot R_A \tag{5.11}$$

Some fore and aft deformations occur in the tyre tread because of the presence of hysteresis in the tyre that generates a rolling resistance moment M_R. Through this, a rolling resistance force arises $F_t = M_R/R_A$ which necessarily is accompanied by tangential deformations.

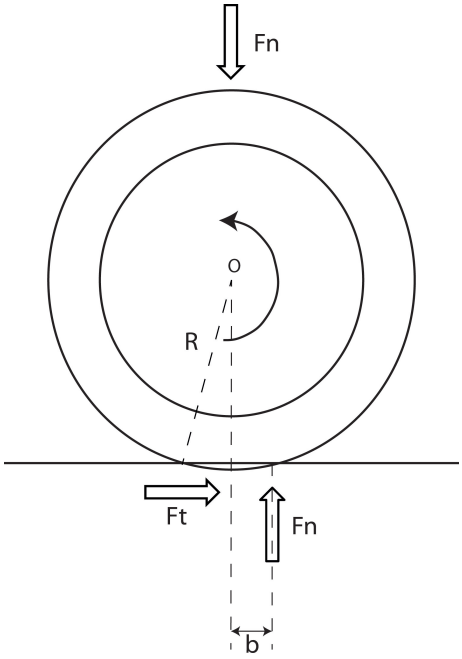

Figure 5.2: Normal and tangential forces acting on the tyre

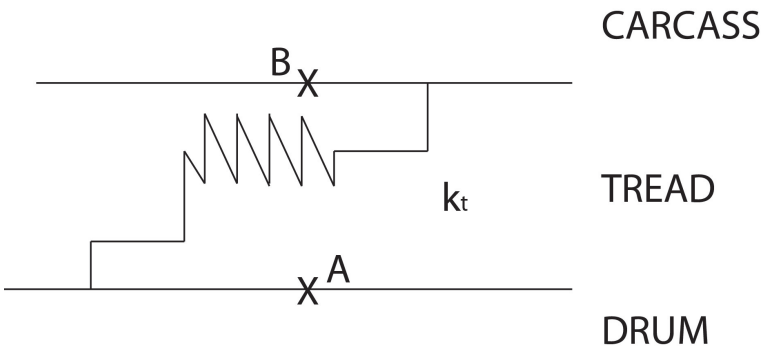

Figure 5.3: Sketch of the brush element

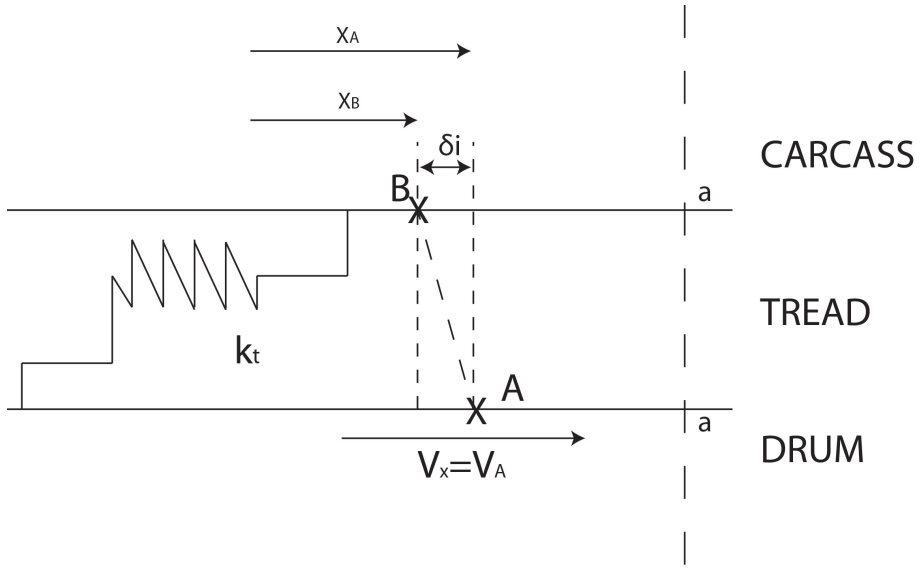

Figure 5.4: Sketch of the brush elements in the contact patch

5.4 "Modified brush model" in case of healthy heavy-duty wheel

An approach, similar to the brush model description, has been adopted in order to describe phenomena that occur in the heavy-duty wheel contact patch, named as "Modified brush model".

With respect to the tyre case, an additional stiffness has been considered: namely "gluing stiffness". This acts in series with "material longitudinal stiffness", obtaining an equivalent stiffness, defined as:

$$k_{eq} = \frac{1}{\frac{1}{k_t} + \frac{1}{k_g}} \tag{5.12}$$

Generally, k_g assumes really high value, representing the strong adhesion interface between the tread and the hub given by the glue presence. As consequence, the point B_t of the tread is rigidly connected with the hub at B_h point: the two

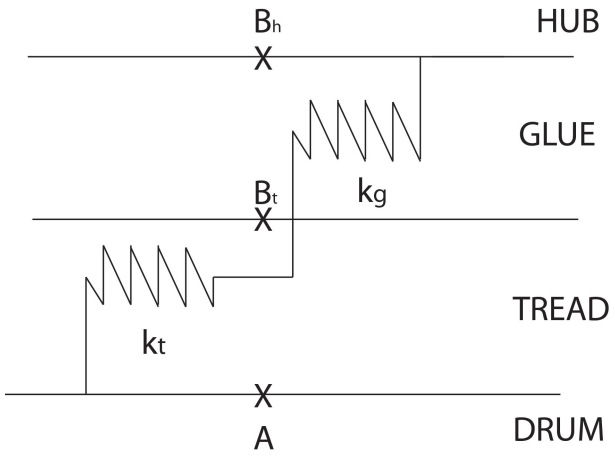

Figure 5.5: Sketch of the "modified" brush element

points can be considered as a common point B, whose position is mainly governed by "material longitudinal stiffness". A representation of k_g and k_t stiffnesses is depicted in Figure 5.6.

5.5 "Modified brush model" in case of faulty heavy-duty wheel

The missing adherence defect, located in the interface between tread and hub, can be represented as a "gluing stiffness" variation, or generally as an "equivalent stiffness" variation. It is due to the fact that points B_t and B_h are not rigidly connected anymore: point B_t is delayed by a distance δ, as depicted in Figure 5.6.
It has been measured experimentally that the delay δ between hub and tread causes a vibratory effect mainly in the horizontal and in the vertical directions, as depicted in Figure 5.7.

In case of missing adherence connection or more in general of an anomaly connection, the "equivalent stiffness" is expected to vary over time with a well defined trend, as depicted in Figures 5.8.

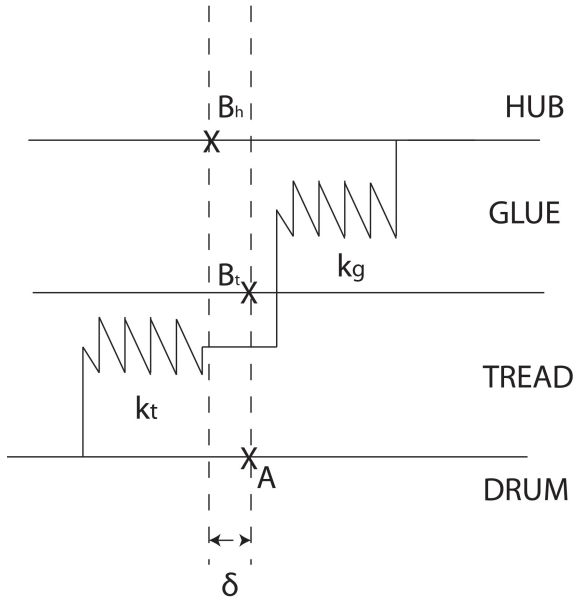

Figure 5.6: Sketch of the "modified" brush model in the contact patch in case of missing adherence defect

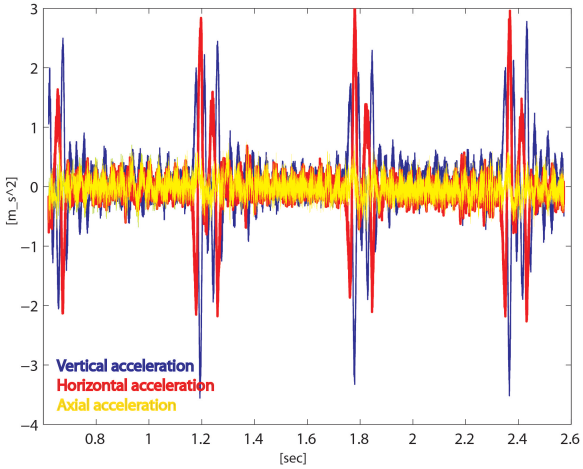

Figure 5.7: Acceleration in the case of a missing adherence defect in the three directions

k_{eq} reaches the lowest value when the defect is completely entered in the contact patch, giving a maximum delay δ_{max} of the hub with respect to the wheel rotation. δ_{max} is maintained constant when the defect passes in the contact patch (the delay between hub and tread is not modified). Eventually it increases when the defect starts to leave the contact patch up to the initial value when the defect completely comes out from the contact patch .

As depicted, the time extension and the peakedness of these three phases can vary, depending on the defect types and on the operational conditions.

The two k_{eq} variation stages generate two separate excitations. After the first excitation, the system response tends to decrease exponentially depending on the system damping. However, this damping phase is interrupted by a new excitation of opposite amplitude.
Experimentally, system responses give rise to signals as depicted in Figures 3.3, 3.4, 3.5, 3.6, in case of missing adherence defects.

In order to better understand this phenomenon, the response of a 1 DOF damped system has been analytically reproduced. The system, characterized by a natural frequency at 40 Hz, has been modelled as excited by two impulses of opposite amplitudes and shifted over a certain Δt time. Figure 5.9 and Figure 5.10 depicts the cases of excitations separated by two different Δt, respectively of 0.025 and 0.05 seconds. The resulting signals, in both time and frequency domain, appear quite different. In particular it is interesting to note the different spectra modulations. This modulation effect can be associated with what generally happen in case of accidental double-tap during EMA analysis evaluated with an instrumented hummer. The double impulses give rise to a double system excitation that is characterized by a spectrum modulated in frequency by the reciprocal of the delay between impulses. Indeed in the simulated case, the modulation frequencies are respectively of 40 Hz and 20 Hz, i.e. the reciprocal of 0.025 and 0.05 seconds.

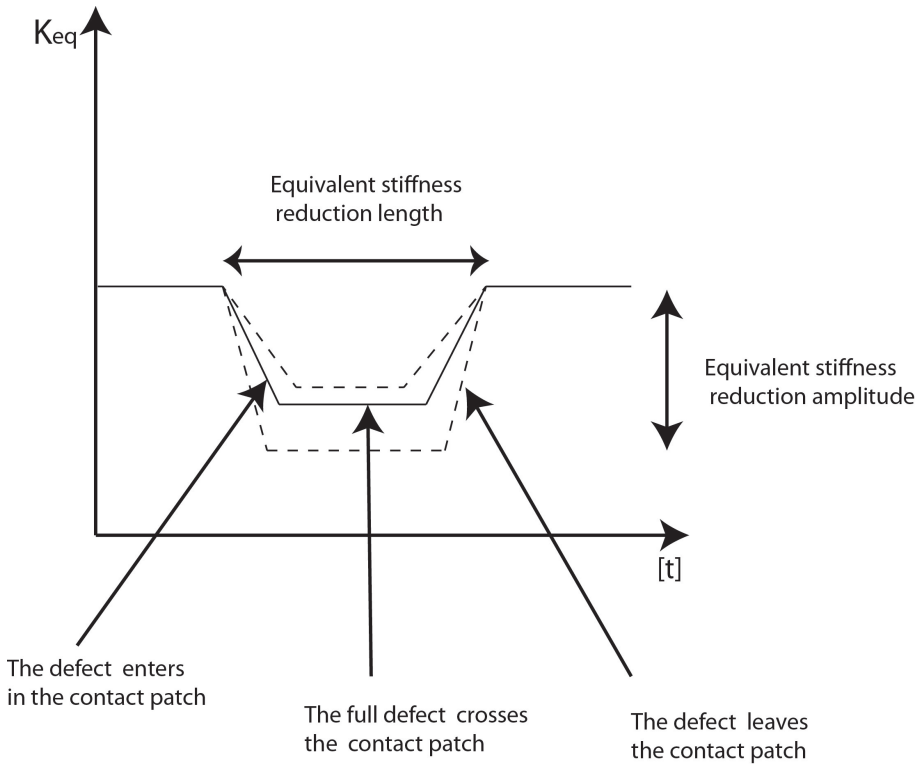

Figure 5.8: Representation of the equivalent stiffness variation trend in case of missing adherence defect

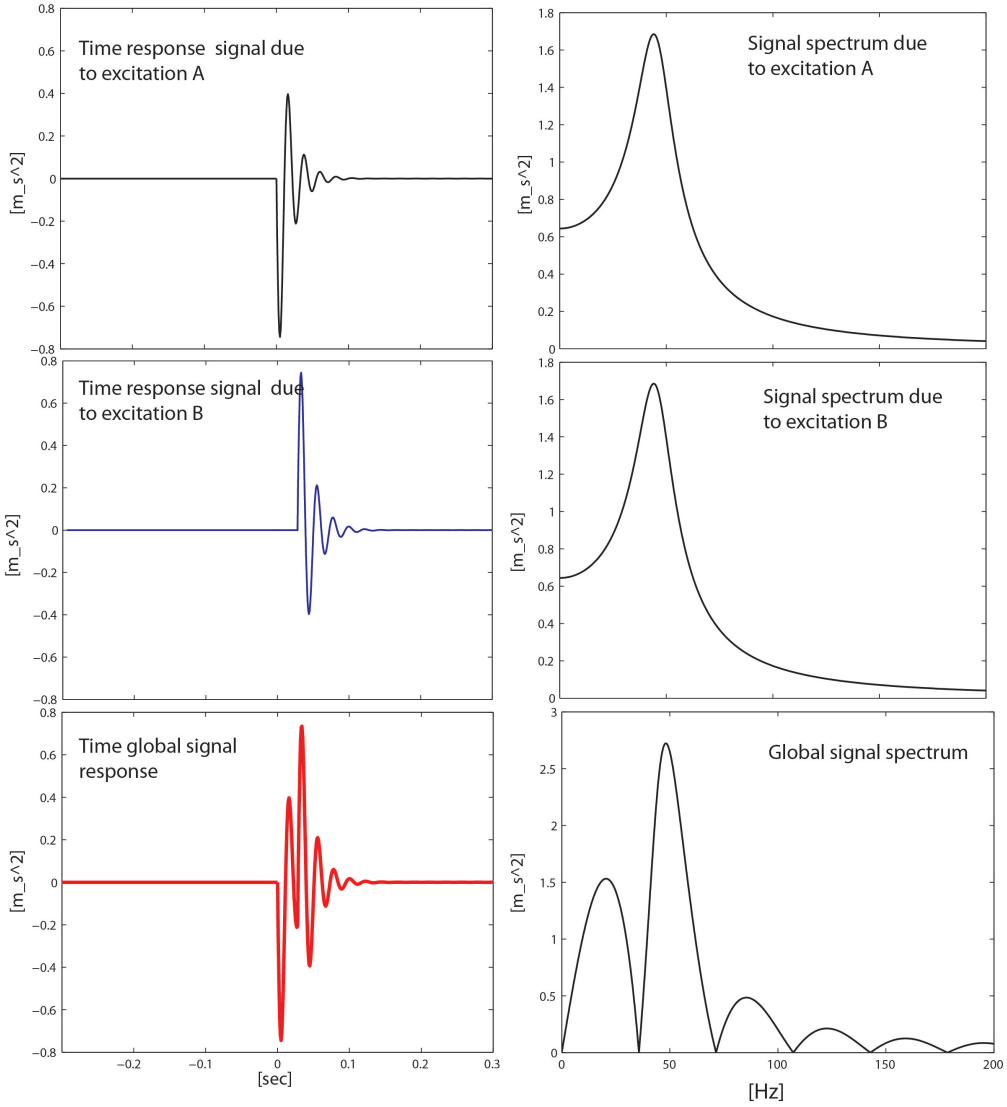

Figure 5.9: Simulated response signal in case of two impulses shifted of a distance time Δt in both time and frequency domain

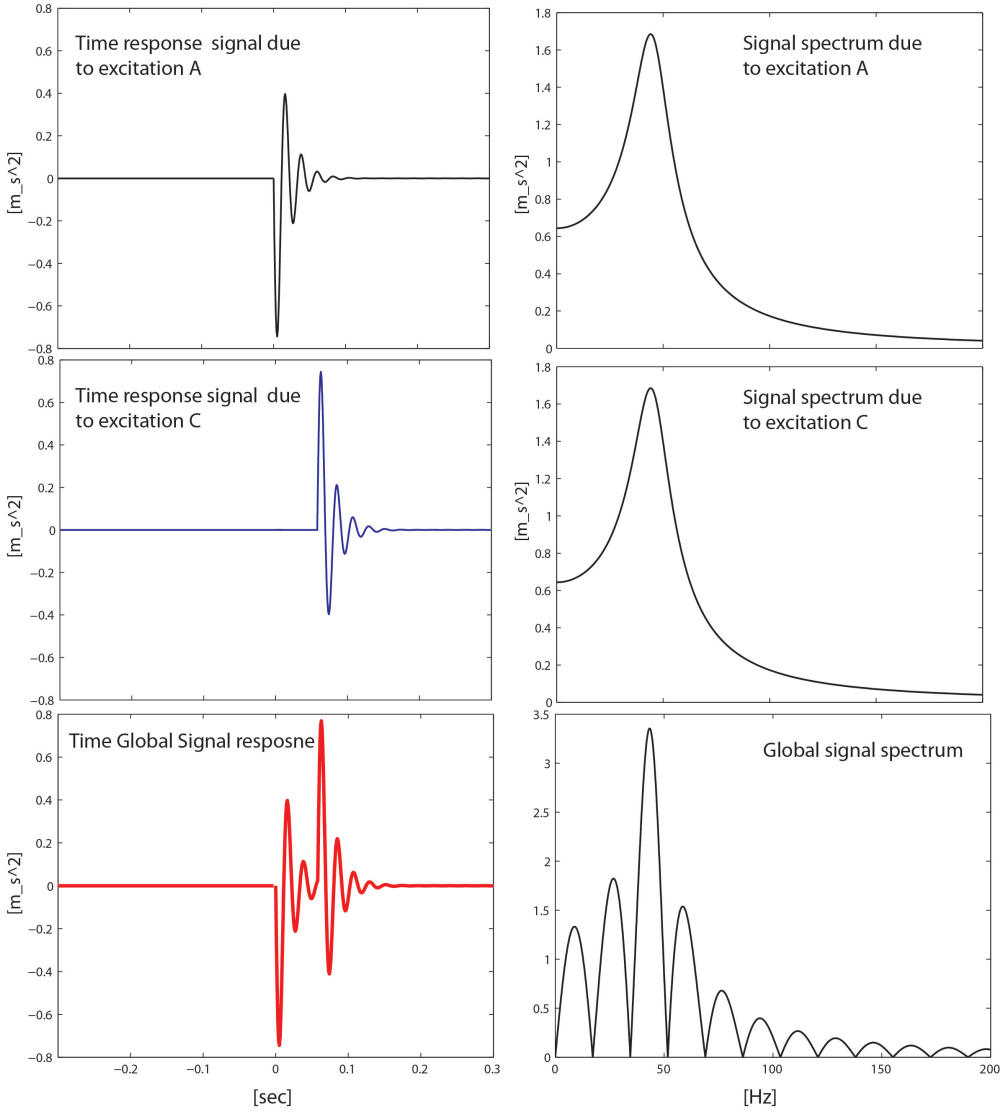

Figure 5.10: Simulated response signal in case of two impulses shifted of a greater distance time Δt in both time and frequency domain

5.6 Operational condition and defect size influences on time signal signature

As introduced in the foregoing section, the “equivalent stiffness” variation is dependent on various factors such as:

- operational speed;
- operational load;
- defect size.

Heavy-duty wheels under operational condition are normally characterized by variable loads and speeds: loads can vary between 350-1000 kg while speeds between 4km/h and 10 km/h. In the following, a physical explanation of the measured vibratory signal in the case of different localized missing adherence defects at various operational conditions has been proposed. The vertical acceleration will be analyzed in detail.

5.6.1 Speed effect

The vibration signal is highly influenced by test speed. In particular, if the wheel rotates at higher speed, it is clear that the time needed by the defect to enter in the contact patch is reduced, giving a sharper k_{eq} variation, and consequently, a higher system excitation. Figure 5.11 reports the SAw in case of an A1 defect at two different speeds (4km/h and 10 km/h) and 1000 kg. The system appears to be significantly more excited at higher velocity.

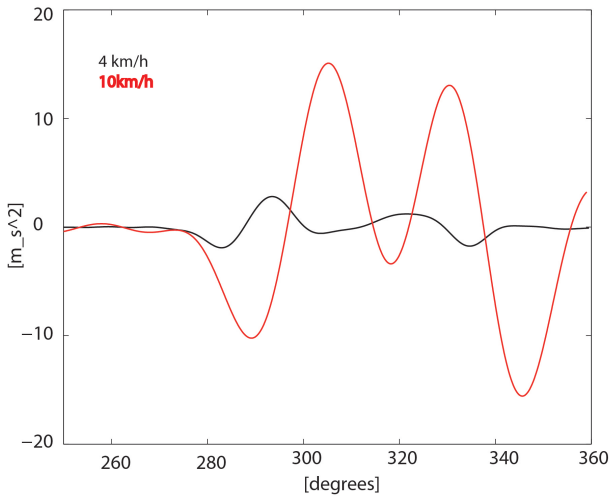

Figure 5.11: Speed effect on the Synchronous average signature in case of A1 defect at 4 km/h and 10 km/h and 1000 kg of load

5.6.2 Load effect

Load conditions produce a different influence on signal behaviour. Figure 5.12 sketches the variation of the contact area between wheel and drum at different load conditions, giving rise to different peak extensions in term of angle range. Points A, B and C highlight the variation of the contact point at different loads. In particular, point A represents the test at low load for which less contact surface and wheel angle is involved in the contact.

On the other hand, point C represents the high load condition that determines larger contact area and larger wheel angle involved. Figure 5.13 shows the vibration signal obtained for defects A2 at three different loads (350 kg, 700 kg and 1000 kg). It is clearly confirmed that peaks have a larger extension in the angle domain when the load increases. The first contact point between the wheel and the drum is advanced (k_{eq} starts to vary earlier) as the load increases while the last contact point is delayed (k_{eq} returns to the initial value later).

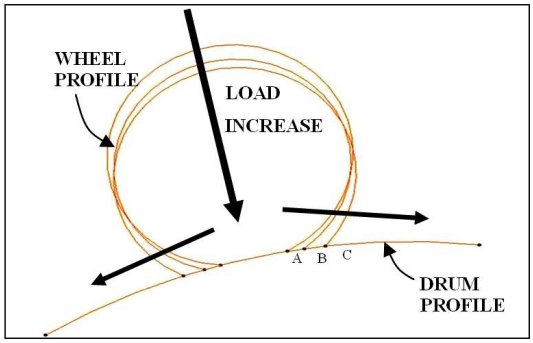

Figure 5.12: Changing of the contact patch extension at different applied loads

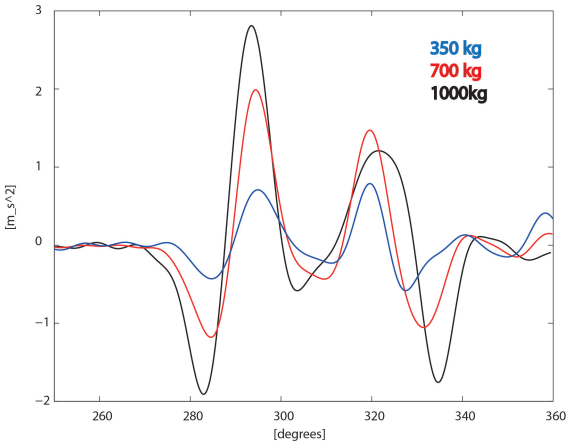

Figure 5.13: Load effect on the synchronous average signature

5.6.3 Defect size effect

Defect size influence can also be explained through the “modified Brush model”. Different considerations have to be made in the case of horizontal (L) and tangential (B) defect size influences.

- a missing adherence defect, not completely extended in the tread-hub interface width (L), gives rise to a reduced k_{eq} variation, and as consequence, to a reduced system excitation. The horizontal defect extension influences the k_{eq} variation amplitude.
- the different tangential length of the missing adherence defect influences the slope of the k_{eq} variation steps. The stiffness variation trend is similar to a square wave in case of small tangential extension. On the contrary, in case of defects with a greater tangential dimension, the stiffness variation trend appears smoother, as highlighted in Figure 5.8.

Hereafter, synchronous average (SAw) evaluated in the case of various missing adherence defect sizes have been compared, see Figure 5.14, at the same test condition. It can be noted that the horizontal dimension of the defect (L) strongly influences the acceleration signal. On the contrary, the defect dimension in the tangential direction slightly influences the response amplitude. The evaluation of a unique parameter (equivalent stiffness) able to represent the effect of different phenomena (defect dimension and operational conditions) represents a useful instrument for diagnostic purposes. In the following paragraphs, this skill is replied in a multibody model, referring to the rolling resistance variation instead of the equivalent stiffness variation.

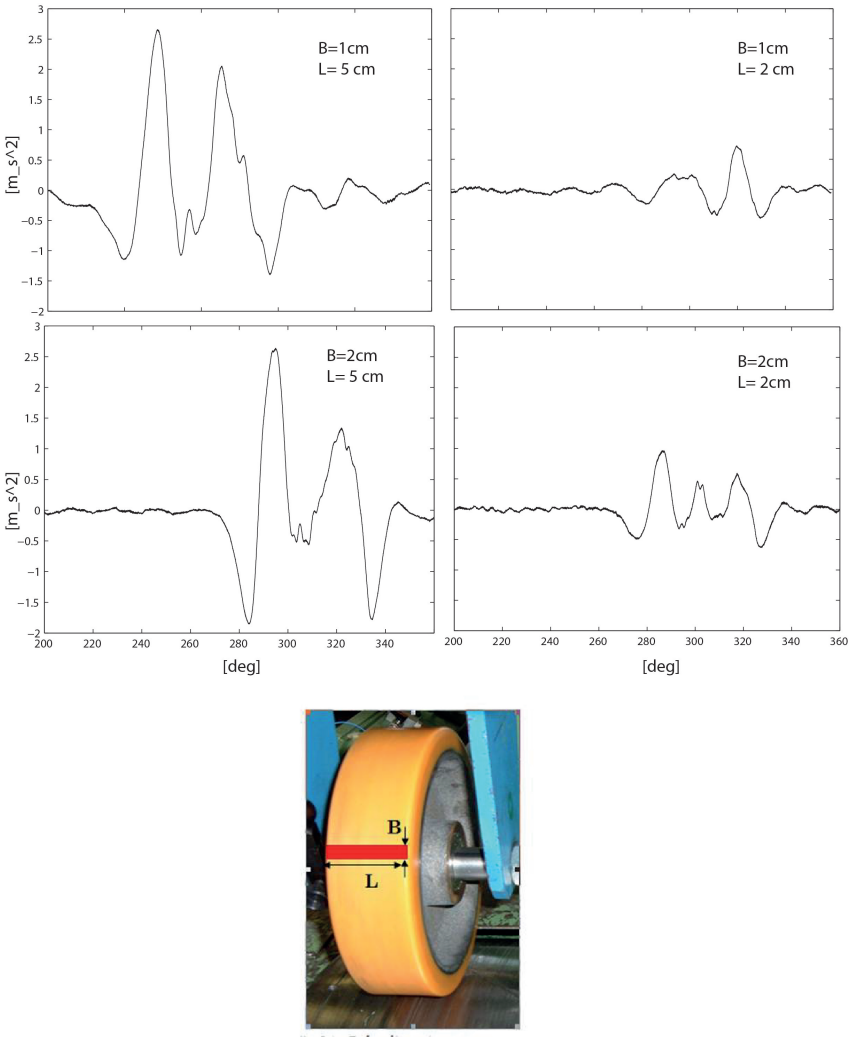

Figure 5.14: Defect dimension effect on the synchronous average signature

5.7 Operational condition and defect size influences on frequency signal signature

The influence of the operational conditions and defect size is clearly visible in the signal spectra. Figure 5.15 reports the spectrum for A1 and A2 defects at the same operational conditions of 4 km/h and 1000kg (a and b) and for A2 in case of 10 km/h and 1000 kg (c). This figure shows several peaks and valleys in the frequency range up to 100 Hz. This modulation of the spectrum is given by the particular system excitations, i.e. by the two consecutive impulses related to the entrance and exit of the defect from the contact patch.

It has been justified through the "modified Brush model" that the time occurring between the two system excitations depends on the operational conditions (load and speed) while the excitation level is due to the defect size.

The same "modulation effect" has been obtained by the numerical signal described here before and highlited in Figures 5.9 and 5.10. Figure 5.16 reports the analytical signal response of a 1 d.o.f system subjected to a periodic double excitation.

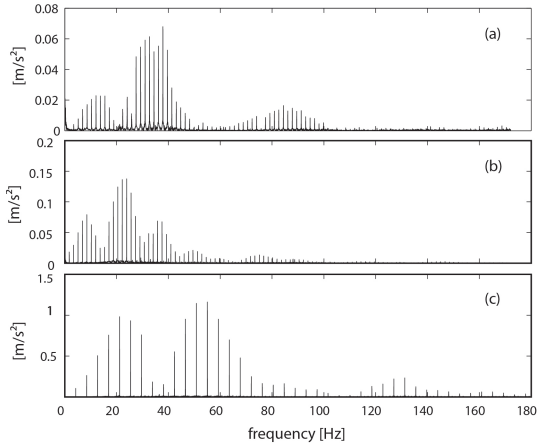

Figure 5.15: Effect of the defect dimension on the signal spectrum in case of a) A1 defect at 4km/h and 1000 kg, b) A2 defect at 4km/h and 1000 kg, c) A2 defect in case of 10km/h and 1000kg

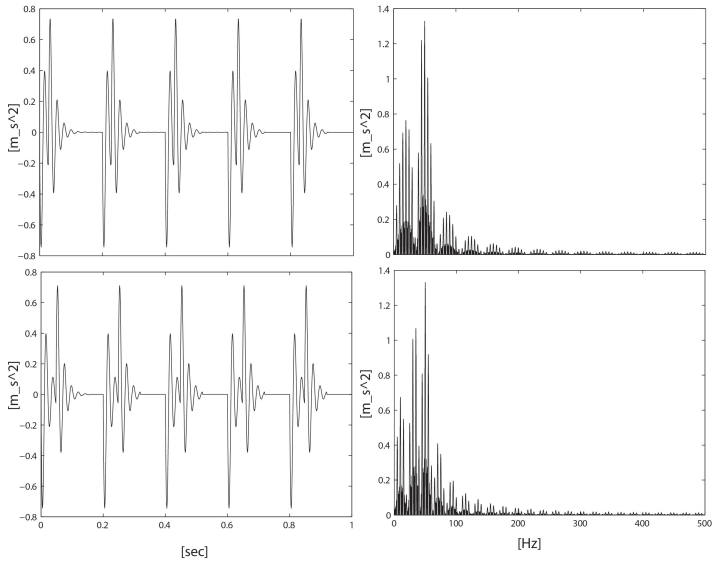

Figure 5.16: Simulated response signals in case of periodic impulses shifted of different distance times $\Delta(t)$ in both time and frequency domain

5.8 Multibody modelling: background

Before describing the heavy-duty wheel multibody model, a short introduction to multibody modelling is presented [22, 23, 62, 63].

Nowadays, the term multibody system is related to a large number of engineering fields of research, especially in robotics and vehicle dynamics. Basically, the motion of bodies is described by their kinematic behavior. The dynamic behavior results from the equilibrium of applied forces and the rate of change of momentum.

A body is usually considered to be a rigid or flexible part of a mechanical system. A link is the connection of two or more bodies, or a body with the ground. The link is defined by certain kinematic constraints that restrict the relative motion of the bodies. There are two important terms in multibody systems: degree of freedom and constraint condition.

The degrees of freedom denote the number of independent kinematic possibilities to move as the minimum number of variables required to define the position of an entity completely in a space.

A constraint condition implies a restriction in the kinematic degrees of freedom of one or more bodies. The classical constraint is usually an algebraic equation that defines the relative translation or rotation between two bodies.

The equations of motion are used to describe the dynamic behavior of a multibody system. Each multibody system formulation may lead to a different mathematical appearance of the equations of motion while the underlying physics is the same. The motion of the constrained bodies is described by means of equations that result basically from Newton's second law. The equations are written for general motion of the single bodies with the addition of constraint conditions. Usually the equations of motions are derived from the Newton-Euler equations or Lagrange's equations. The motion of rigid bodies is described by means of:

$$M\left(q\right)\ddot{q} - Q_v + C_q^T\lambda = F \tag{5.13}$$

$$C\left(q,\dot{q}\right) = 0 \tag{5.14}$$

This form of the equations of motion is based on so-called redundant coordinates, because the equations use more coordinates than degrees of freedom of the underlying system. The generalized coordinates are denoted by q, the mass matrix is represented by $M\left(q\right)$ which may depend on the generalized coordinates. C represents the constraint conditions and the matrix C_q (sometimes termed the Jacobian) is the derivation of the constraint conditions with respect to the coordinates. This matrix is used to apply constraint forces λ to the corresponding equations of the bodies. The components of the vector λ are also denoted as Lagrange multipliers. In a rigid body, possible coordinates could be split into two parts,

$$q = \left[u\ \psi\right]^T \tag{5.15}$$

where u represents translations and ψ describes the rotations.

5.9 Heavy-duty wheel multibody modelling

A multibody model of the heavy-duty wheel rotating on a moving drum is presented. The model is realized for diagnostics purposes in order to give a physical explanation of the defect effects. The worthiness of the " modified Pacejka's approach" is evaluated, verifying the effect of defect sizes and operational conditions on the numerical system response.

The wheel has been simplified as a rigid ring component. This assumption is supported by the results of the wheel dynamic characterization reported in Chapter 4, in which it has been attested that the acceleration response in the case of a missing adherence defect is not influenced by the wheel natural frequencies.

The yielding part has been focused in the contact patch, considering a nonlinear elastic contact algorithm: the contact force and the system responses are governed by a vertical stiffness and a damping value. This information has been experimentally obtained though static tests conducted on the wheel.

The model has been validated comparing the acceleration numerical results with the experimental data in the case of an impact against an obstacle.

Concerning the representation of the anomalous connection defects, an approach based on the 'modified brush model' has been adopted. The equivalent stiffness, i.e. the tangential material stiffness and the gluing stiffness, is not modelled. Consequently, the defect effect has been introduced in the model through a rolling resistance moment variation over time.

The effects of speed, load and defect size have been represented in the model modifying the rolling resistance moment over time. In the following only the vertical system response will be considered.

5.9.1 Non linear Hertzian force contact algorithm

In the multibody model, only the static material properties have been considered, due to the rigid assumption.

System responses and transmitted forces have been evaluated through a non-linear Hertzian contact algorithm, since the following assumptions were fulfilled:

- the material deforms only elastically;
- the load points normally to the contacting surfaces;
- the dimensions of the contact area are small compared to the radii of curvature of the contacting bodies;
- the deformations of the contacting bodies are small compared to the dimensions of the contact area.

The adopted contact model is called “polygonal contact model” (PCM). [63–66]. This technique is based on the representation of the body surfaces by polygon meshes and contact force determination by the elastic foundation model. The contact is examined using an areal discretization of the contact patch. It can be regarded as a compromise between the simple contact approach and the costly FEA.

Polygonal surfaces consist of vertices and faces. A vertex is defined by its position coordinates in the Euclidean space. A face is defined by pointers to the vertices of a polygon. The totality of its faces represents the topology of a polygonal surface.

The PCM task consists of three steps. First a collision detection algorithm determines if the contact pair is in touch. If no collision is detected, the program returns zero force and torque and the analysis is finished. Otherwise PCM constructs the intersecting areas of the surfaces and discretises the corresponding contact patches in the second step. Finally the contact force of each contact element is determined and the contact force and torque resulting of all contact

elements are calculated. This technique has been used by the author in a further activity related to the modelling of a deep groove ball bearing, reported in Appendix 1, where it is compared to other contact algorithms.

PCM appears to be an efficient contact tool and its computational cost depends on the discretization level of the surfaces.
A simplified representation of the parameters involved in the PCM algorithm is reported in Figure 5.17.
The force can be expressed as:

$$F_{tot} = \sum_{i=1}^{N} F_i \tag{5.16}$$

where n is the number of embedded vertices. The force due to embedded vertices i is applied in equal and opposite directions to both the face and the embedded vertex:

$$F_i = \begin{bmatrix} F_i^{vertex} \\ \hline F_i^{face} \end{bmatrix} = \begin{bmatrix} F_i^{contact} \\ \hline -F_i^{contact} \end{bmatrix} \tag{5.17}$$

The contact force generated by vertex i has normal and tangential components:

$$F_i^{contact} = F_{n,i} + F_{t,i} \tag{5.18}$$

The normal component of contact force arises from stiffness and damping and is given by:

$$F_{n,i} = \max\left[kg^e + c\left(D_{MAX}\right)\dot{g}\right] \tag{5.19}$$

where

- n is the normal to the triangle,
- k is the user-specified stiffness,
- g is the current amount of penetration of the vertex into the triangle

- e is a user-specified exponent,
- c is the user-specified damping constant.
- $\dot{g}$ is the current relative penetration velocity,
- D_{MAX} is the penetration at which the damping force is scaled to $c\dot{g}$ with a cubic step function.

The normal force is limited so that it does not exhibit adhesive properties while the damping factor smoothly increases by a cubic function from zero to the user-specified value c as penetration increases from 0 to the depth D_{MAX}. As D_{MAX} approaches zero, this transition becomes more abrupt which can cause simulation efficiency to suffer. As D_{MAX} is increased, the effect of damping may be lessened. The tangential component of the contact force (the friction force) is given by:

$$F_{t,i} = [f_n \mu]\, n_{\perp} \tag{5.20}$$

where:

- f_n is the magnitude of the normal force, given by 5.19;
- μ is the friction coefficient function of sliding velocity;
- $n_{\perp}$is a unit vector along the direction of the sliding velocity.

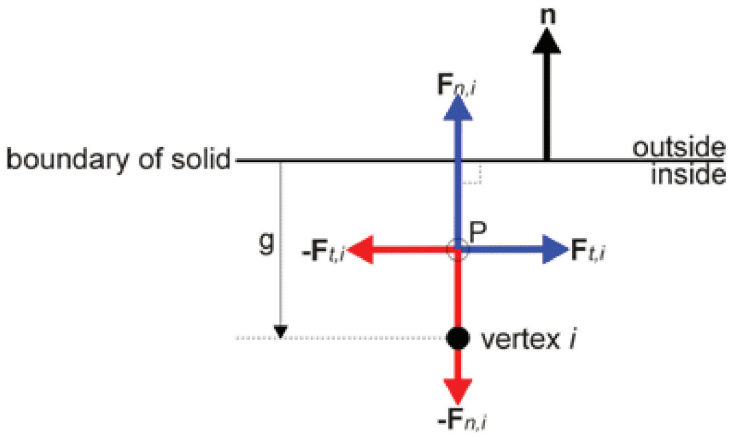

Figure 5.17: Simplified representation of the contact between vertex and triangle

5.9.2 Main model components and joints

Different components are represented in the multibody model, as depicted in Figure 5.18. In particular:

- fixed traverse;
- moving traverse at which a force given by a pneumatic actuator is applied;
- wheel support;
- shaft;
- hub;
- tread;
- drum.

have been sketched, inserting the respective material densities. The LMS Virtual Lab program provides the component inertia properties. Eventually, the different components are connected adopting the following joints:

- Bracket joint between hub and tread
- Bracket joint between hub and shaft
- Revolute joint between support and shaft
- Bracket joint between moving traverse and support
- Revolute joint between moving traverse and fix traverse.

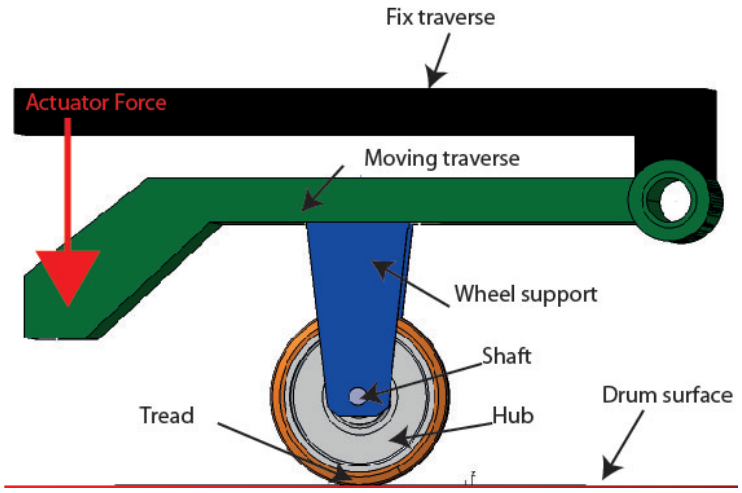

Figure 5.18: Multibody model: main components

A force is applied between the fixed and the moving traverse, representing the pneumatic actuator force.

5.9.3 Experimental evaluation of stiffness and structural damping

The stiffness inserted in the contact modelling has been evaluated through static tests conducted on the heavy-duty wheel, obtaining a loading-unloading

curve cycle, see Figure 5.19. Only the loading curve has been considered for the stiffness evaluation, due to the slight difference between loading and unloading curve. This curve has been fitted considering a constant stiffness value and a well-adapt exponent:

- $k = 4000N/(mm^e)$
- $e = 1.58$

The hysteric damping ratio has been evaluated, measuring the area between the loading and unloading curves, obtaining a 3.4 $\%$ damping value. However, since the model requires the knowledge of the a damping constant c, this value has been obtained as:

$$c = 2\xi\sqrt{km} \tag{5.21}$$

where:

- m is the system mass (wheel, support, moving traverse);
- k is the mean value of the wheel vertical stiffness, see Equation 5.19;
- ξ is the damping ratio

obtaining a damping coefficient of 800 kg/s.

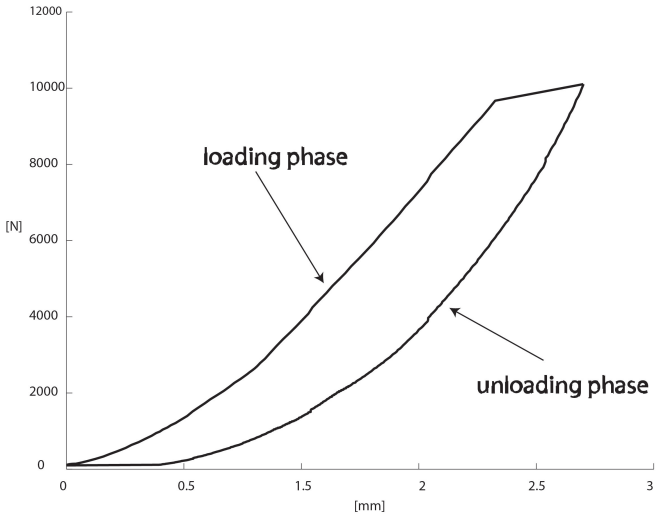

Figure 5.19: Static load-strain curve of the heavy-duty wheel

5.10 Model results in case of cleat impact and localized defect

5.10.1 Cleat impact modelling

First of all, the model has been validated comparing simulated and experimental acceleration signals in the case of a wheel impact against a cleat positioned on the hub surface.

Figure 5.20 shows the acceleration spectrum of the wheel support in case of wheel impacting against a cleat obstacle at the two different speeds of 2km/h and 4km/h. At higher speed, the impact excites a broader spectrum range, including the frequencies related to the wheel dynamics. Since the model considers the wheel as rigid, a test has been conducted at a limited speed of 2 km/h.

A good correspondence between experimental and acceleration data has been found, as highlighted in Figure 5.21 and 5.22 in both time and frequency domain.

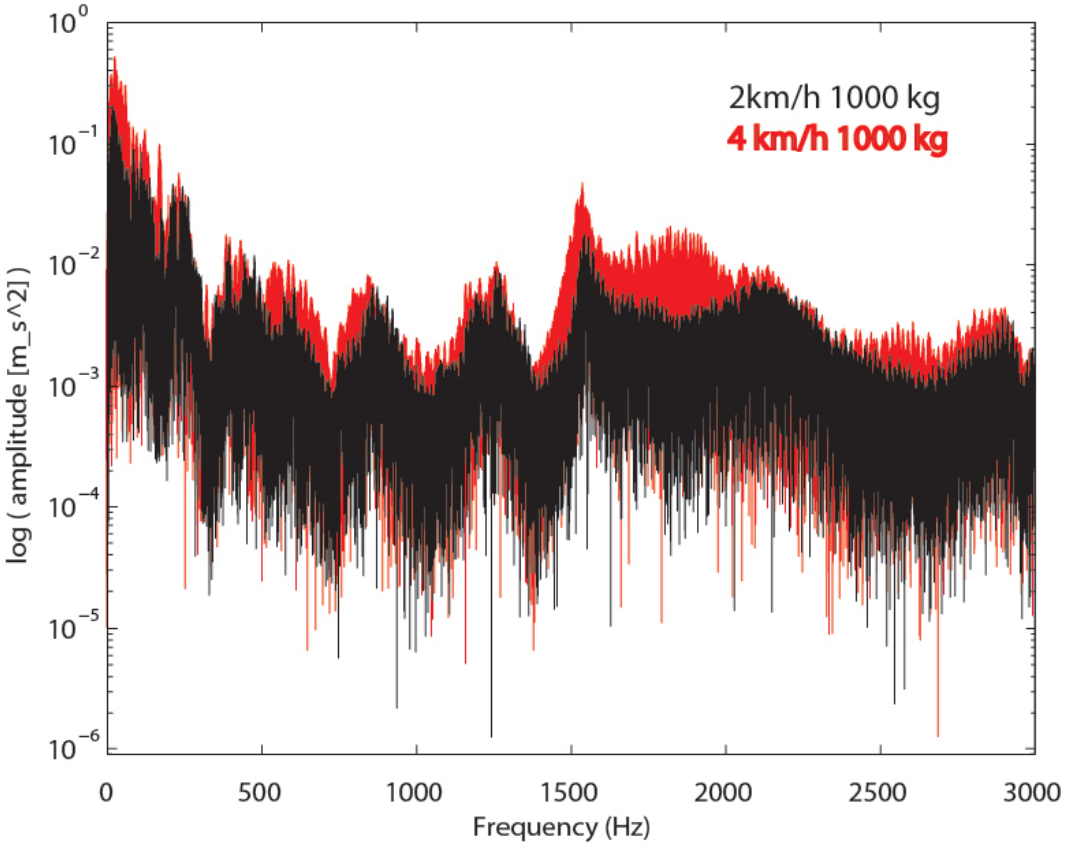

Figure 5.20: Experimental acceleration spectrum in the case of a cleat impact at two different speeds

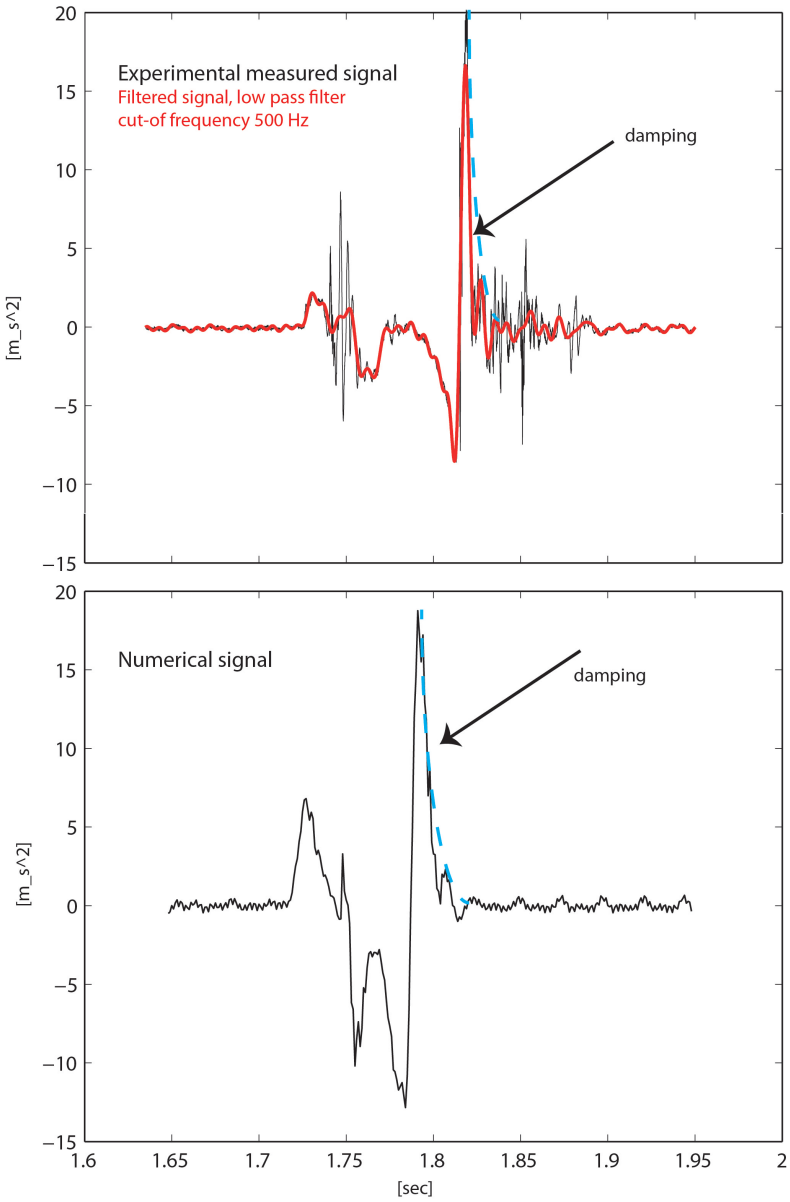

Figure 5.21: Experimental and numerical acceleration in the case of a cleat impact

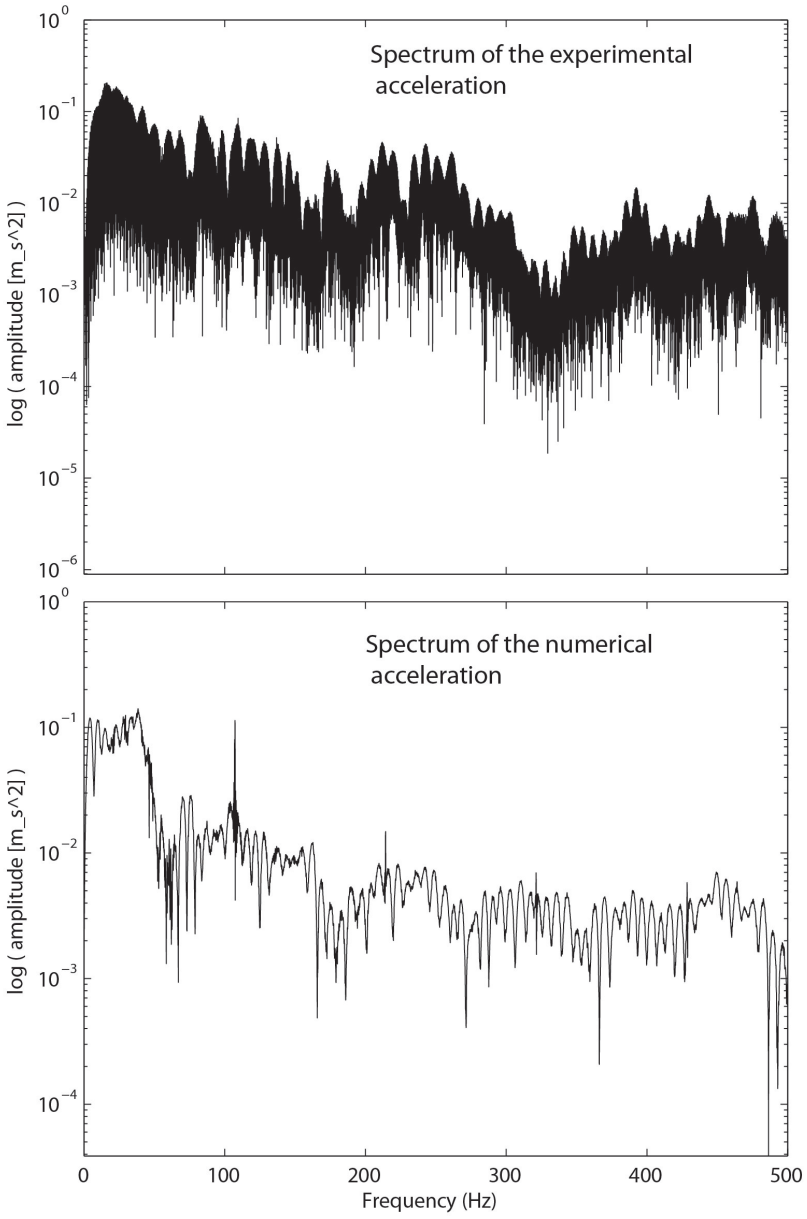

Figure 5.22: Experimental and numerical acceleration spectrum in case of cleat impact

5.10.2 Missing adherence defect modelling

Having verified the model capability on simulating the response in the case of a obstacle assuming:

- rigid bodies and yielding contact patch;
- non linear elastic material behavior;

the effect of a missing adherence defect has been simulated in the model. The defect presence has been introduced by modifying the "rolling resistance moment" instead of tangential and gluing stiffness (that are not present in the model). This modelling assumption is justified by Equations 5.7 and 5.11, that can be rewritten as:

$$\delta_i = \frac{F_t}{k_{eq}} = \frac{{}^{M_R}\!/_{R_A}}{k_{eq}} \tag{5.22}$$

The M_R variation follows the over time trend of $1/k_{eq}$, i.e. the reciprocal amplitude trend of the one depicted in Figure 5.8, i.e.:

- M_R reaches the highest value when the defect is completely entered in the contact patch, giving a maximum delay δ_{max} of the hub respect to the wheel rotation;
- δ_{max} is maintained constant when the defect passes in the contact patch (the delay between hub and tread is not modified);
- M_R decreases when the defect starts to leave the contact patch up to the initial value when the defect completely comes out from the contact patch.

Different M_R over time variation signals have been introduced in the model, Figure 5.23. In particular three different "rolling resistance moment" variations are proposed (indicated with A, B and C letters), obtaining different wheel support acceleration responses, depicted in Figure 5.24. The double system excitations, originated in the M_R variation steps, gives rise to a response signal

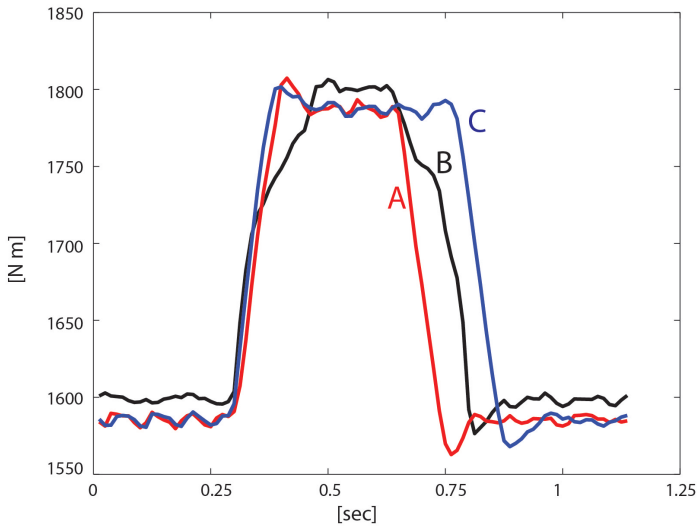

Figure 5.23: Different numerical rolling resistance moment variations

similar to the ones experimentally detected, as depicted in Figures 3.3, 3.4, 3.5, 3.6. The "rolling resistance moment" over time variations confirms the same assumptions of the "brush modal approach" about the defect and operational condition influences:

- the step related to the M_R increment gives rise to a first system excitation;
- the step related to the M_R decrement gives rise to a second system excitation;
- it is possible to represent the operational conditions and the defect size by varying the slope and the distance of the M_R over time variation.

5.11 Future development

Further model developments will regard:

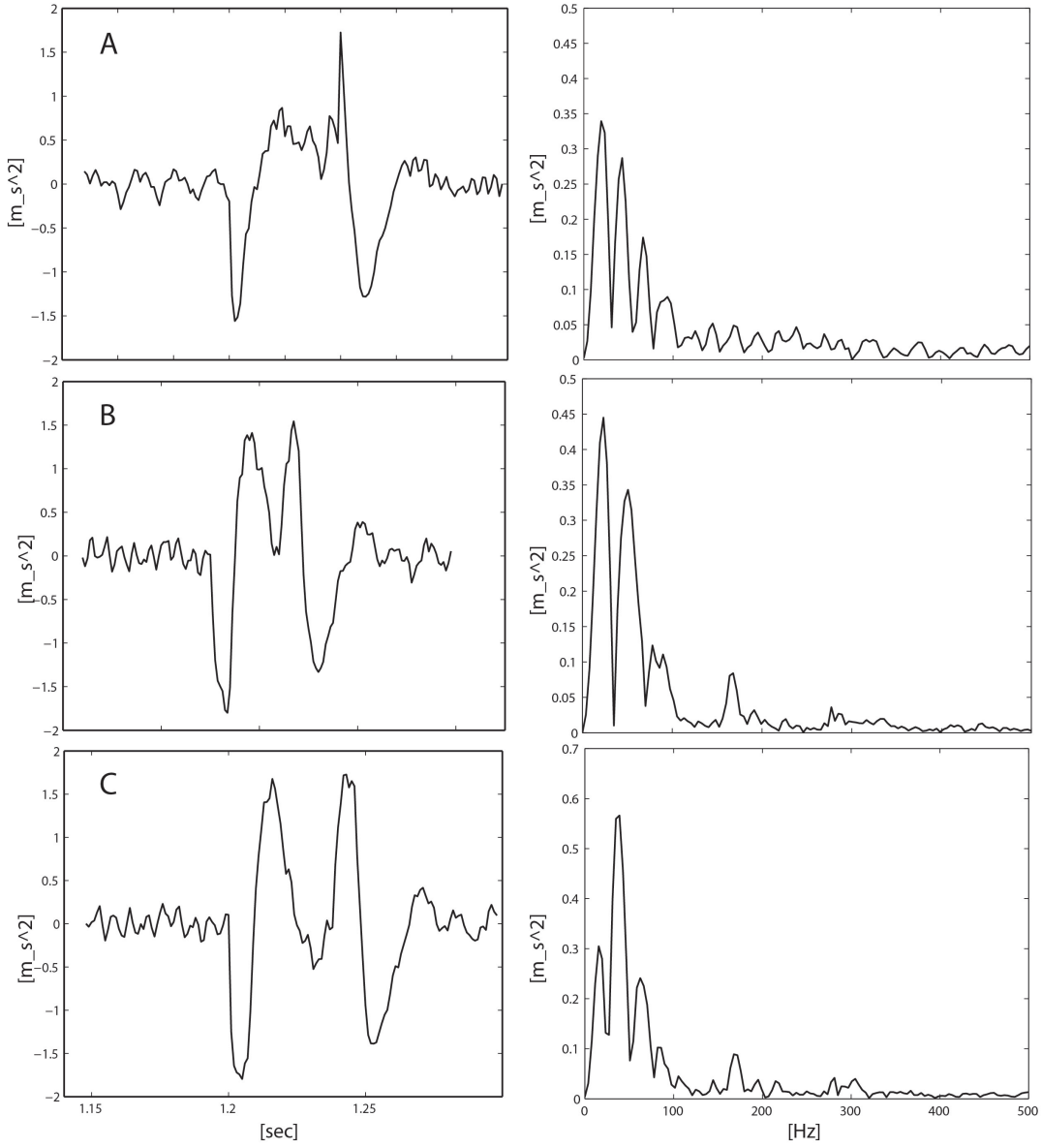

Figure 5.24: Numerical acceleration response in the case of three different torque variation trends

- insertion in the model of a longitudinal tread stiffness;
- insertion in the model of a gluing stiffness, variable with the rotation and the component width;

in order to obtain the real vibratory signal, in terms of amplitude and angular extension.

5.12 Intermediate results

In this chapter a simplified approach to understanding the phenomena related to the missing adherence defect was proposed, based on the “modified brush model”.
In particular it was found that:

- a connection anomaly located between the hub-tread interface causes a variation of the “equivalent stiffness”;
- the “equivalent stiffness” varies over time depending on the operational conditions and on the defect size;
- the particular signal signature in the case of a localized missing adherence defect was characterized by two double peaks. These system responses are due to excitation given by the defect upon entering and leaving the contact patch;
- the multibody model represents the defect through a variation of the “rolling resistance moment”. The obtained results confirm the worthiness of the “modified brush model” assumptions.

Chapter 6

Model-based discussion of monitoring and diagnostics results

6.1 What is the chapter about?

The monitoring and diagnostics campaign, described in Chapter 3, gave indication concerning the different fault detection capabilities of the adopted processing techniques.
Subsequently, Chapter 5 reported the application of the “modified brush model” on the multibody wheel model, giving an explanation of different signal signatures.
This chapter aims at answering the following question:

- What is the reason for the differing level of technique efficiencies?

6.2 Comprehension of the different experimental technique efficiencies

In Chapter 5, an anomaly in the tread-hub connection has been represented as a variation of the so called “equivalent stiffness ” while in the multibody model as a variation of the so called “rolling resistance moment”. This over time variation can be subdivided in three main stages, as sketched in Figures 5.8 and 5.23:

1) the defect enters in the contact patch;

2) the entire defect crosses the contact area;

3) the defect leaves the contact patch.

The incoming and leaving phases generate a variation of the relative displacement between tread and hub. The result is a double system excitation, shifted by a time Δt and of opposite amplitudes. It has been shown that amplitude and distance between the two excitations depend on the operational conditions and on the defect sizes.

6.2.1 Localized missing adherence defect

In the case of a localized missing adherence defect, the measured signal is expected to be composed of two parts: one deterministic and one non-deterministic:

- a deterministic part, related to all the phenomena periodic with the wheel rotation, i.e. the periodic "equivalent stiffness" variation that gives rise when the defect enters and exits form the contact patch;
- a non-deterministic part, found to be second order cyclostationary, due to the inevitable presence of slip phenomena originated in the contact between the polyurethane tread and drum.

If tests are conducted at constant speed and load, the "equivalent stiffness " variation becomes periodic with the wheel rotation, giving rise to a deterministic signal. The periodic system excitation turns out to be quite significant in case of localized missing adherence defects with a horizontal extension in the full or in the half wheel width, namely A1, A2, A3 and A4. As a consequence, a synchronous average evaluated on the wheel rotation (SAw) is able to emphasize the fault presence as depicted in Figures 3.3, 3.4, 3.5 and 3.6 and Kurtosis and RMS coefficients assume high values, see Tables 3.1, 3.2, 3.3.

However, in the case of a more localized missing adherence defect, namely MA, the defect evaluation is not straightforward. The stiffness variation entity is considerably smaller as is the resulting excitation. Synchronous averaging hardly shows the defect presence and consequently the statistical coefficients are quite inefficient, as reported in Tables 3.5, 3.6 and in Figure 6.1.
A further technique, based on the evaluation of the cyclostationary level of the measured signal, was applied. The first order ciclostationary level of the signal has been expressed through the first order cumulant, i.e. the Discrete Fourier Transform (DFT) of the sampled purified signal synchronized with the wheel rotation. In the case of a missing adherence defect, the first order cumulant appears significantly different respect to the healthy case. This is largely expected due to the fact that the "equivalent stiffness" variation happens every wheel rotation, giving to the signal a high deterministic content. Nevertheless the ICS_{1x}, as defined in Equation 3.3, was not able to detect all the tested faulty wheels, as resumed in Figure 3.12. Indeed, it happened that some healthy wheels, characterized by a non perfect round surface or a tread deformation originated in the mounting phase, were presenting an high ICS_{1x} values. As a result, the threshold pass-fail ICS_{1x} value was increased.
Analyzing the second order cyclostationary content of the signal, it has been found that the MA wheel was presenting a slightly superior contribution with respect to the healthy wheel case, due to the inevitable presence of slip effects. This is clear comparing second order cumulants of Figures 3.8 and 3.9. Since the healthy wheels present irrelevant ICS_{2x} values, the respective threshold appears really low, Table 3.8. Moreover the ICS_{2x} values do not present the same dispersion effect of ICS_{1x}.The ICS_{2x} is able to detect all the missing adherence faulty wheels as possible anomalies, Figure 6.2.

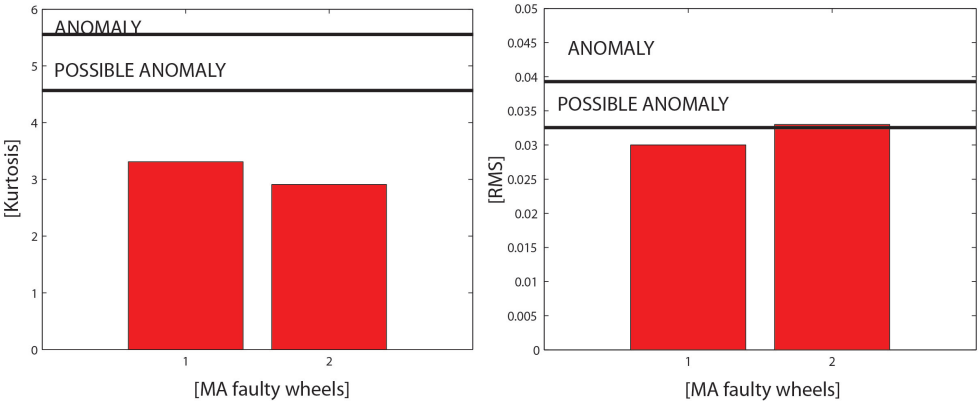

Figure 6.1: Kurtosis and RMS pass-fail distributions in case of MA defects

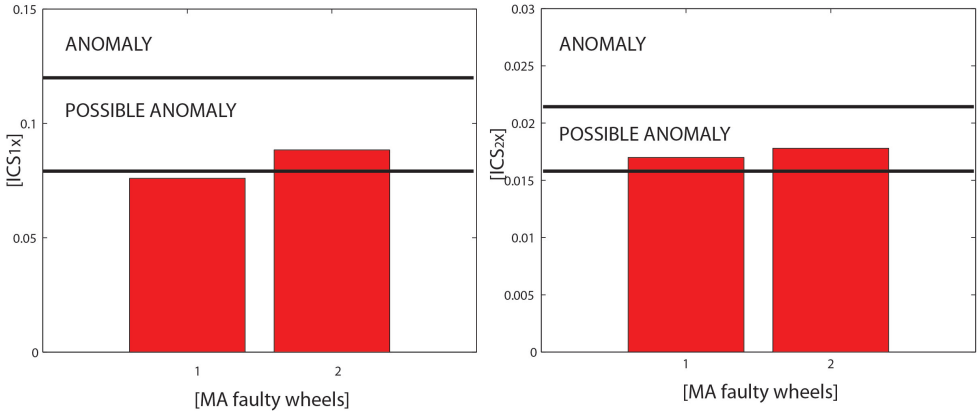

Figure 6.2: $\hat{C}^{\alpha}_{1x}$ and $\hat{C}^{\alpha}_{2x}$ pass-fail distributions in case of MA defects

6.2.2 Rust defect

Wheels presenting localized or distributed rust defects gave different response signals, as reported in Chapter 3.
Hereafter, an explanation of the high variability related to the rust defect manifestation is given, based on the “equivalent stiffness” approach.
With respect to the missing adherence defect, rust defects do not cause abrupt “equivalent stiffness” variations. The two stages related to the incoming and the exit of the defect from the contact patch can be expected,however the “equivalent stiffness” variation over time can be considered as characterized by a high randomness.
The measured signal can be considered as composed of:

- a deterministic part, due to the periodic incoming and exit of the defect from the contact patch;

- a higher non-deterministic part; indeed, when rust enters in the contact patch, the “equivalent stiffness” exhibits highly casual variations, giving rise to random system excitations and producing a high second order cyclostationary level in the vibration response.

Kurtosis, applied to the SAw, shows a low detecting capacity. The resulting SAw is not characterized by significant localized peaks.
On the contrary, the RMS coefficient is able to detect most of the rusty wheels. This is due to the high signal irregularities given by the unpredictable “equivalent stiffness” variations
Figures 6.3 and 6.4 highlight these different monitoring capacities in both cases of localized (LR) and distributed (DR) rust.
Cyclostationary analysis has been applied to the LR and DR wheels. First and second order cumulant appears considerably different with respect to the healthy wheel ones, as clearly visible by comparing Figure 3.8 with Figures 3.10 and 3.11. This is due to the fact that the instants related to the entrance and

the exit of the rust from the contact patch are periodic with the wheel rotation. However, the high randomness linked to the "equivalent stiffness" variation contributes to increasing the second order cyclostationary content of the signal. As a consequence, the second order cyclostionary indicators ICS_{2x} are able to detect all the rusty wheels, as highlighted in Figures 6.5 and 6.6.

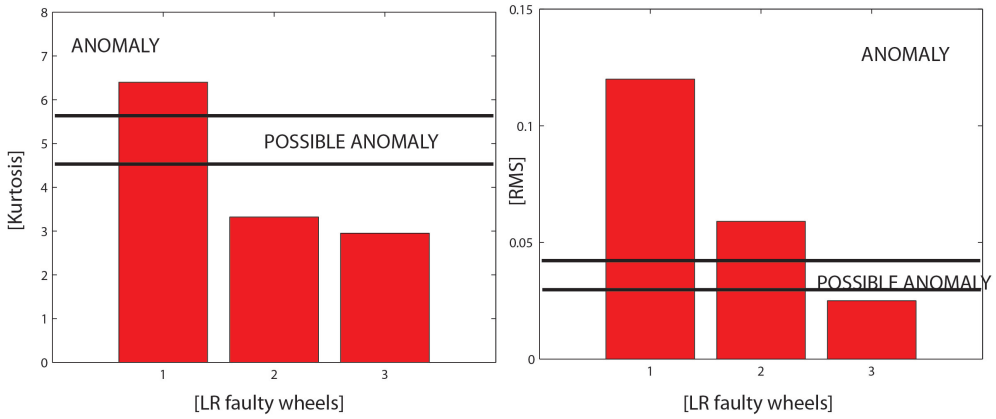

Figure 6.3: Kurtosis and RMS pass-fail distributions in case of LR defects

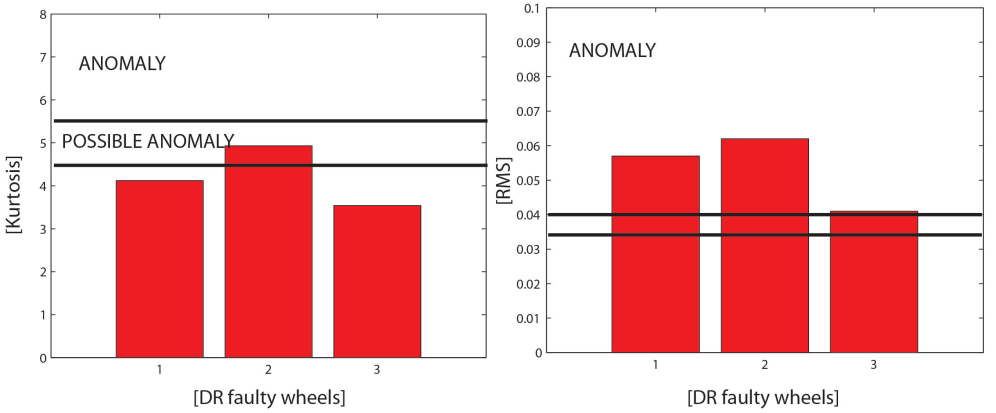

Figure 6.4: Kurtosis and RMS pass-fail distributions in case of DR defects

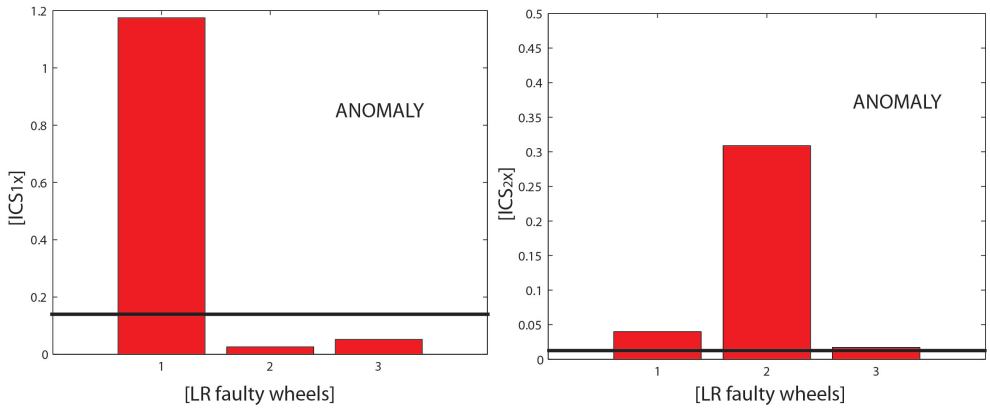

Figure 6.5: $\hat{C}^{\alpha}_{1x}$ and $\hat{C}^{\alpha}_{2x}$ pass-fail distributions in case of LR defects

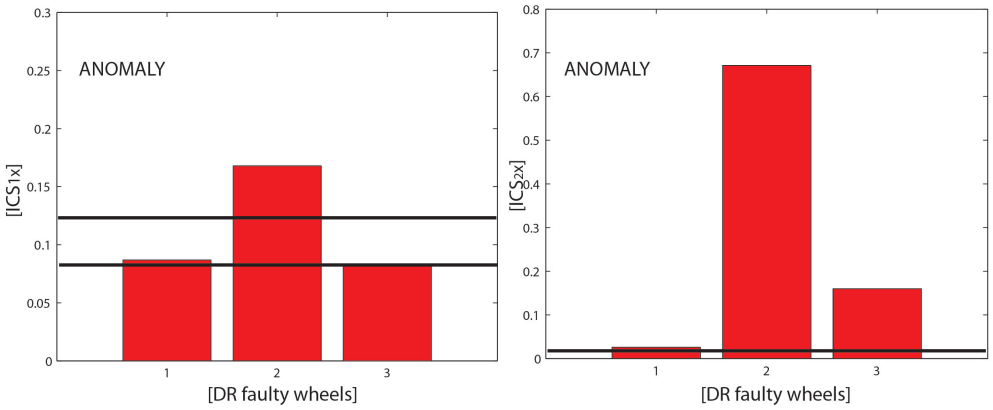

Figure 6.6: $\hat{C}^{\alpha}_{1x}$ and $\hat{C}^{\alpha}_{2x}$ pass-fail distributions in case of DR defects

Chapter 7

Conclusions

This thesis addresses a methodology and a procedure for the condition monitoring and diagnostics of heavy-duty wheels based on vibration measurements and multibody modelling. As the author is aware, it is the first time this component is considered from a monitoring or diagnosis standpoint.

After a brief introduction in Chapter 1, a general overview of the signal processing techniques adopted in this thesis is presented in Chapter 2.

In Chapter 3, a number of different processing techniques are developed and applied in order to recognize faults in heavy-duty wheels. Defects of different dimensions reproducing missing adherence between the polyurethane tread and the hub are artificially created (Figure 3.1). In these defects, the adhesive was not correctly applied due to the local absence of adhesive or due to the presence of rust in the hub, as can happen during the manufacturing process. These defects cause incorrect wheel rotations and fast failure. Firstly, the experimental apparatus and the operational test conditions (peripheral speed of the drum and load applied on the wheel) are presented (Figure 3.2), highlighting the pros and cons of different measurement transducers for monitoring and diagnosis purpose, and determining the test condition that best shows the presence of the faults. The synchronous average (SAw) has been evaluated and statistical parameters for fault detection (Kurtosis and RMS) have been used. Furthermore, the cyclostationary nature of the signal has been investigated through

the first and second order cumulants and relative indicators. A non statistical approach (Tukey's method) has been used in order to calculate threshold values for the sound/fault discrimination (Figures 3.7 and 3.12). The Continuous Wavelet Transform has been applied to the SAw and used for the identification of the defect type (Figure 3.13). A monitoring-diagnostic procedure has been suggested suitable for a large scale control at the end of the production line (Figure 3.14). This activity has enabled the following conclusions to be drawn:

- the acceleration signal is the most appropriate for the detection of anomalies localized in the tread-hub interface;
- the operational test condition of 4 km/h (low speed) and 1000 kg (high load) highlights at the best the fault presence;
- the Kurtosis and RMS coefficients estimated on the SAw, in cooperation with ICS1x and ICS2x indicators applied to the residual signal, are useful metrics for the definition of the state of health of the wheel, i.e. detection of missing adherence and localized/distributed rust defects;
- the Continuous Wavelet Transform makes it possible to identify common order contents for similar defect types.

In Chapter 4, a procedure for the dynamic characterization of the heavy-duty wheel has been reported. The main objective was the evaluation of the wheel dynamic effect on the experimental signal in case of tread-hub anomaly connections. First of all, an overview of the main background required to dynamically study viscoelastic components has been described (Figure 4.2). Subsequently, this procedure has been applied to the heavy-duty wheel, emphasizing the main limitations that can be encountered in practice.

The heavy-duty wheel dynamics were analyzed in the following stages.

- Analysis of a tread material sample through static and dynamic tests (Figures 4.4 and 4.6): determination of material characteristics such as Young modulus and damping, at limited preloads and deformation amplitudes.

In case of limited deformations and static loads, the material shows a slight dependency on frequency, preload and deformation amplitudes: in these conditions the polyurethane material behavior can be represented through a linear isotropic material model.

- The linear isotropic material properties were inserted in a finite element model, representing the wheel in free-free condition. The model results were compared with the data obtained by experimental modal analysis conducted on the hub and on the complete wheel: good correspondence between numerical and experimental results were registered.

- Tests in real operational conditions were carried out on two wheels with the same mass but different tread material in the same set up and test conditions. The acceleration spectrum due to the impact against a cleat obstacle highlights a first peak shift approximately around 850 Hz, corresponding to the first wheel natural frequency. Thus, the wheel can be considered as a rigid body up to around 800 Hz. The material characteristics in real operational conditions were obtained updating the finite element model using data coming from this experimental test.

In Chapter 5, a comprehension of the physical phenomena that cause the particular signal signature is given. First of all, a simplified approach aimed at the comprehension of the phenomena related to the missing adherence defect is proposed, based on the 'Pacejka brush model'. This approach, namely the "modified brush model" represents the connection between tread and hub via an " equivalent stiffness " (Figure 5.6). An anomaly in the connection is expressed by an "equivalent stiffness" variation. In the case of a localized fault of a missing adherence, the "equivalent stiffness" is considered to vary over time with a well defined trend, as depicted in Figures 5.8. "Equivalent stiffness" k_{eq} reaches the lowest value when the defect is completely entered in the contact patch, giving a maximum delay δ_{max} of the hub with respect to the wheel rotation. δ_{max} is maintained constant when the defect passes in the contact patch. Eventually, k_{eq} increases when the defect starts to leave the contact patch up to the initial

value when the defect completely comes out from the contact patch. These two sudden stiffness variations produce two impulsive excitations of opposite amplitude, shifted of a time Δt related to the defect passing time through the contact patch. In order to explain the signal signature dependency on defect size and on operational conditions, these excitations are applied to a 1 d.o.f damped system, analytically reproducing the vibration response. Figure 5.9 and Figure 5.10 depicts the results obtained using different Δt: the resulting signals, in both time and frequency domain, appear quite different, in terms of signal signature and spectra modulations.

Finally, the "modified brush model" approach has been verified via a multibody model of the heavy-duty wheel (Figure 5.18). Based on Chapter 4 results, the model considers the tread as rigid. The yielding part has been focused in the contact patch, considering a non linear-elastic contact algorithm, namely PCM, using the vertical stiffness and the damping value experimentally obtained through static tests conducted on the wheel. The contact forces and the vibration responses are extracted.

The model has been validated comparing the acceleration numerical results with the experimental data in case of impact against an obstacle. Eventually, missing adherence defects have been represented in the model. Since the equivalent stiffness, given by the tangential material stiffness and the gluing stiffness, is not modelled, the defect effect has been qualitatively introduced though a "rolling resistance moment" variation over time. The model is able to reproduce the effect of anomalous connections between tread and hub, representing an instrument for the interpretation of the experimental results.

In Chapter 6, the different effectiveness of the monitoring and diagnostics techniques used in the experimental campaign have been explained, based on the model suggestions.

In fact, in the case of a localized fault of a missing adherence,the measured signal can be considered as composed of:

- a deterministic part, related to all the phenomena periodic with the wheel rotation, i.e. the periodic "equivalent stiffness" variation that appears

when the defect enters and exits form the contact patch;

- a non-deterministic part, found to be second order cyclostationary, due to the inevitable presence of slip phenomena originating in the contact between polyurethane tread and drum.

In the case of rust defect, the measured signal can be considered as composed of:

- a deterministic part; due to the periodic incoming and exit of the defect from the contact patch;
- an higher non deterministic part; indeed, when rust enters in the contact patch, the “equivalent stiffness” exhibits highly casual variations, giving rise to random system excitations and producing a high second order cyclostationary level in the vibration response.

As a consequence, Synchronous average and respective statistical coefficients, such as Kurtosis and RMS, present a low fault detecting capacity in case of modest or random “equivalent stiffness” variation, i.e. really localized missing adherence defect (MA) or rust (LR and DR). In order to detect all the possible fault types, it is necessary to analyze the residual part of the signal through the second order cyclostationary technique. The ICS_{2x} of the residual signal represents a very useful indicators of tread/hub connection anomalies, in both case of missing glue or rust (Figures 6.5, 6.6, 6.2). Thus, ICS_{2x} can be considered as the key parameter to be adopted in a monitoring test station at the end of the production line.

Considering the presented research activity, the main original contributions concern:

- the application of advanced vibration processing techniques to monitoring and diagnostics of heavy-duty wheels ;
- the assessment of the different technique effectiveness, supported by the explanation of vibration sources and characteristics via analytical and multibody modelling;

- the definition of a monitoring/diagnostics procedure suitable for a large-scale quality control at the end of the production line.

Bibliography

[1] Tellure rota spa web site: http://www.tellurerota.com.

[2] A. Rivola G. Dalpiaz. Condition monitoring and diagnostics in automatic machines: comparison of vibration analysis techniques. *Mechanical Systems and Signal Processing*, 11(1):53–73, 1997.

[3] O.Niculita A.Rivola S.Delvecchio, G.Dalpiaz. Condition monitoring in diesel engines for cold test applications. part i: vibration analysis for pass/fail decision. part i: vibration for pass/fail decision. *Ana C V Veira et oth. editors*, pages 197–206, 2007.

[4] J. Antoni R.B. Randall. Rolling element bearing diagnostics – a tutorial. *Mechanical Systems and Signal Processing*, 25:485–520, 2011.

[5] J.Antoni. Cyclic spectral analysis in practice. *Mechanical Systems and Signal Processing*, 21:597–630, 2007.

[6] J.Antoni. Cyclostationary by examples. *Mechanical Systems and Signal Processing*, 23:987–1036, 2012.

[7] L. Gelman F. Combet. An authomated methodology for performing time synchronous averaging of a gearbox without speed sensor. *Mechanical system and Signal Processing*, 21:2590–2606, 2007.

[8] M.M. Toozhy P.D.McFadden. Application of synchronous averaging to vibration monitoring of rolling element bearings. *Mechanical Systems and Signal Processing*, 14 (6):891–906, 2000.

[9] M.Sidahmed A.Raad, J.Antoni. Indicators of cyclostationarity: Theory and application to gear fault monitoring. *Mechanical System and Signal Processing*, 22:574–587, 2008.

[10] F.L. Chu Z.K. Peng. Application of the wavelet transform in machine condition monitoring and fault diagnostics: a review with bibliography. *Mechanical System and Signal Processing*, 18:199–221, 2004.

[11] P.D. McFadden W.J. Wang. Application of wavelets to gearbox vibration signals for fault detection. *Journal of Sound and Vibration*, 192:927–939, 1996.

[12] C.K. Chui. *Wavelet Analysis and its Application Vol.1: An Introduction to Wavelets*. 1992.

[13] A. Rivola E. Mucchi, G. Dalpiaz. Dynacmi behavior of gear pumps: effect of variations in operational and design parameters. *Meccanica*, 46 (6):1191–1212, 2011.

[14] A.Mikkola J.Sopanen. Dynamic model of a deep-groove ball bearing including localized and distributed defects. part 1: theory. *J. Multibody-Dynamics*, 217:201–211, .

[15] A.Mikkola J.Sopanen. Dynamic model of a deep-groove ball bearing including localized and distributed defects. part 2: Implementation and results. *J. Multibody-Dynamics*, 217:213–223, .

[16] R.B. Randall N. Sawhali. Simulating gear and bearing interactions in the presence of faults part. i. the combined gear bearing dynamic model and simulation of localized bearing faults. *Mechanical Systems and Signal Processing*, 22:1924–1951, 2008.

[17] R.B. Randall N.Sawhali. Simulating gear and bearing interactions in the presence of faults part ii: Simulation of the vibrations produced by extended bearing faults. *Mechanical Systems and Signal Processing*, 22: 1952–1966, 2008.

[18] C.M. Krousgrill D.S. Stutts and W.Soedel. Parametric excitation of tire wheel assemblies by a stiffness non uniformity. *Journal of Sound and Vibration*, 179 (3):499–512, 1995.

[19] W. Soedel D.S. Stutts. A simplified dynamic model of rolling resistance in pneumatic tires and the effect of internal damping. *Journal of Sound and Vibration*, 155, 1991.

[20] W. Desmet D. Vandepitte H. De Gersem, D. Moens. Dynamic interval analysis of fe models with uncertain substructures. *Proceedings of ISMA 2006*, pages 4077–4088, 2006.

[21] S. Petersen O. von Estorff M.Brinkmeier, U.Nackernhorst. A finite element approach for the simulation of tire rolling noise. *Journal of Sound and Vibration*, 309:20–39, 2008.

[22] Robert Seifried Werner Schiehlen, Nils guse. Multibody dynamics in computational mechanics and engineering applications. *Computer methods in applied mechanics and engineering*, 195:5509–5522, 2012.

[23] Ben Marrant Dirk Vandepitte wim desmet jan Helsen, Frederik Vanhollebeke. mutlibody modelling of varying complexity for modal behaviorr analysis of wind turbine gearboxes. *Renewable Energy*, 36:3098–3113, 2011.

[24] D.J Ewins. *Modal Testing: theory and practice*. Research Study, Press Ltd, 1984.

[25] P.Sas W.Heylen, S.lammens. *Modal Analysis theory and testing*. KUL Press, Leuven, Belgium, 2007.

[26] H. Van der Auweraer L. Hermans. Modal testing and analysis of structures under operational conditions industrial applications. *Mechanical Systems and Signal Processing*, 13(2):193–216, 1999.

[27] L.Soria A.Vecchio E. Pierro, E.Mucchi. On the vibro/acoustical operational modal analysis of a helicopter cabin. *Mechanical Systems and Signal Processing*, 23:1205–1217, 2009.

[28] Alexander F. Vakakis Jean Claude Golinval Gaetan Kerschen, Keith Worden. Past, present and future of nonlinear system in structural dynamics. *Mechanical Systems and Signal Processing*, 20:505–592, 2006.

[29] A.K. Mallik N.Chandra Shekhar, H. Hatwal. Response of non linear dissipative shock isolators. *Journal of Sound and Vibration*, 227:293–307, 1999.

[30] C.W. Wong Y.Q. Ni, J.M. Ko. Identification of non linear hysteretic isolators from periodic vibration tests. *Journal of sound and Vibration*, 217 (4):737–756, 1998.

[31] P.Vanherck J.Peters, Cl. De Meersman. *The measurement of the elastic and loss moduli of rubber and rubberlike materials*. Pro Manuscripto, Katholieke Universiteit Leuven.

[32] Christopher M. Richards Jie Zhang. Parameter identification of analytical and experimental rubber isolator represented by maxwell models. *Mechanical System and Signal Processing*, 21:2814–2832, 2007.

[33] D.H.Cooper. Method of applying the results of dynamic testing to rubber anti vibration systems. *Transactions of the Institution of the Rubber Industry*, 35 (959):166–177, 2012.

[34] Jie Pan Tian Ran Lin, Nabil H.Farag. Evaluation of frequency dependent rubber mount stiffness and damping by impact test. *Applied Acoustics*, 66: 829–844, 2005.

[35] R.Singh S. Kim. Multi-dimensional characterization of vibration isolators over a wide range of frequencies. *Journal of Sound and Vibration*, 245: 877–913, 2001.

[36] C.M. Richards J. Zhang. Dynamic analysis and parameter identification of a single mass elastomeric isolation system using maxwell voight model. *ASME Journal of Vibration and Acoustics*, 128:713–721, 2006.

[37] T. Pritz. Frequency dependences of complex moduli and complex poissonís ratio of real solid materials. *Journal of Sound and Vibration*, 214 (1):83–104, 1998.

[38] Y. Champoux S.Nadey. Application of the direct complex stiffness method to engine mounts. *Experimental techniques*, 24(3):343–351, 2000.

[39] S. Delvecchio. Advanced vibration processing techniques for condition monitoring and quality control in i.c. engines and harvesting machines. *PhD Thesis*, 2009.

[40] G. D Elia. Fault detection in rotating machines by vibration signal processing techniques. *PhD Thesis*, 2008.

[41] R.B.Randall. *Frequency analysis*. K.Larsen and Son, 1987.

[42] P.R. White J.K. Hammond. The analysis of non-stationary signals using time-frequency methods. *Journal of Sound and Vibration*, 190(3):419–447, 1996.

[43] J. Wismer. *Time Domain Averaging Combined with Order Tracking*. Bruel and Kjaer, Denmark, 2012.

[44] D. S. Munck K.R. Fyfe. Analysis of computed order tracking. *Mechanical System and Signal Processing*, 11(2):187–205.

[45] R. B. Randall. State of the art in monitoring rotating machinery. *Proceedings of ISMA2002*, pages 1457–1478, 2002.

[46] R.A. Braun. *Mechanical Signature Analysis*. Academic Press, London., 1986.

[47] H. Van der Auweraer et al. Spectral estimation of time-variant signal. *Proceedings od ISMA17*, pages 207–223, 1992.

[48] H. Van der Auweraer et al. Analysis of non stationary noise and vibration signals. *Proceedings of ISMA17*, pages 385–405, 1992.

[49] E. Newland. Wavelet analysis, part i: Theory. *Journal of Sound and Vibration*, 116:409–416, 1994.

[50] E. Newland. Wavelet analysis, part ii: Wavelet maps. *Journal of Sound and Vibration*, 116:417–425, 1994.

[51] Zamaraev R.U. Schukin L.I Schukin, E.L. The optimization of wavelet transform for the impulse analysis in vibration signals. *Mechanical Systems and Signal Processing*, 18:1315–1333, 2004.

[52] J.Tukey. *Exploratory Data Analysis*. Addison Wesley, 1977.

[53] B. Eftekharnejad D. Mba. Seeded fault detection on helical gears using acoustic emission. *Proceedings of the 21th International Congress and Exhibition*, pages 167–175, 2008.

[54] M. Elforjani D.Mba. Acoustic emission and natural degradation of a slow speed bearing. *Unknown Journal*, pages 187–197, 2008.

[55] LMS International. *LMS Test.Lab, Rev.7B*. 2007.

[56] Unknown Author. *Theory of Viscoelasticity*. Academic Press, New York, 1971.

[57] W. Flugge. *Viscoelasticity*. Springer, Heidelberg, 1975.

[58] J.D. Ferry. *Viscoelastic properties of Polymers*. John Wiley and Sons, New York, 1980.

[59] F.De Coninck P. Sas W. Desmet P. Kindt, D.Berckmans. Experimental analysis of the structure borne ture/road noise due to road discontinuities. *Mechanical Systems and Signal Processing*, 23:2557–2574, 2009.

[60] M. Sinapius G. Gloth. Analysis of swept sine runs during modal identification. *Mechanical system and Signal processing*, 18:1421–1441, 2004.

[61] Hans B. Pacejka. *Tyre and vehicle dynamics*. Elsevier, Amsterdam, 2006.

[62] Werner Schiehlen. Computational dynacmis: theory and applications of multibody systems. *Europena Journal of Mechanics A/Solids*, 25:566–594, 2006.

[63] E.Pennestri F.Cheli. *Cinematica e dinamica dei sistemi multibody*. Casa Editrice Ambrosiana, 2008.

[64] LMS International. *Virtual.Lab online help*.

[65] SKF. *SKF Bearing Handbook*. 1991.

[66] G.Hippmann. An algorithm for compliant contact between complexly shaped bodies. *Multibody System Dynamics*, 12:345–362, 2004.

[67] R.B. Randall N. Sawalhi. Simulation of the vibrations produced by extended bearing faults in gearboxes. 2006.

[68] A. Palmgren G. Lundberg. Dynamic capacity of rolling bearing. *Acta Polytechnic Mechanical Engineering Series*, 1 (3), 1947.

[69] R.Gohar M.Akturk, K.Gupta. The effects of number of balls and preload on vibrations associated with ball bearings. *J.Tribology*, 119:747–753, 1997.

[70] K.Gupta. On the geometrical imperfections in ball bearings. *J.Tribology*, 110:19–25, 1988.

[71] O.Prakash M.Tiwari, K.Gupta. Effect of radial internal clearance of ball bearing on the dynamics of a balanced horizontal rotor. *Journal of Sound and Vibration*, 238:723–756, 2000.

[72] G.C. Van Nijen Y.H. Wijnat, J.A. Wensing. The influence of lubrication on the dynamic behaviour of ball bearings. *Journal of Sound and Vibration*, 222 (4):579–596, 1999.

[73] T. Kondou T. Ayabe H. Tamura S. Fukata, E.H. Gad. On the vibration of ball bearings. *Bulletin of JSME*, 28 (239):899–904, 1985.

[74] R.B. Randall N.S. Feng, E.J. Hahn. Using transient analysis software to simulate vibration signals due to rolling element bearing defects. *Unknown Journal*, pages 689–694, 2002.

[75] H.Endo N.Sawalhi, R.B. Randall. The enhancement of fault detecton and diagnosis in rolling element bearings using minimum entropy deconvolution with spectral kurtosis. *Mechanical Systems and Signal Processing*, 21 (6):2616–2633, 2007.

[76] M.Dowling. Application of non-stationary analysis to machinery monitoring. *IEEE Paper*, 0-7803-0946-4/93:159–162, 1993.

[77] H. McCallion I.K. Epps. An investigation into the characteristics of vibration excited by discrete faults in rolling element bearings. *Unknown Journal*, 1994.

[78] R.B.Randall N.Sawalhi. Vibration response of spalled rolling element bearings: Observations, simulations and signal processing techniques to track the spall size. *Mechanical Systems and Signal Processing*, 25 (3):846–870, 2011.

[79] H.Hertz. On the contact of rigid elastic solids and on hardness. *Miscellaneous Papers*, pages 163–183, 1896.

[80] R.Budynas G. W. C. Young. *Roark's Formula for Stress and Strain*. Seventh Edition, McGraw Hill, 2002.

[81] F.J.Harris. *Rolling Bearing Analysis I*. Wiley, 1966.

Appendix A
Multibody model of spalled rolling bearings: effectiveness of different contact algorithms

A.1 Introduction

Rolling element bearings represent one of the most critical components in rotating machines. In the last decades bearings have been investigated in different experimental campaigns conducted on various kinds of test- rig realized ”ad hoc” to emphasize the main dynamic behaviour phenomena [16, 67]. In the mean time several simulation models have been developed in order to describe the influence of physical characteristics and operational conditions through an analytical approach.

The first modelling activities on rolling element bearing were conducted by Lundberg and Palmgren [68] with the assumptions of non-linear stiffness and time-invariant system describing radial and axial deflections. Akturk [69] and Gupta[70] investigated the complete field of non-linearity and time-varying characteristics describing the main non-linearity causes: Hertzian force/deformation factors, compliance effect, clearance between rolling element and bearing races and the effect of lubricant.

Tiwari [71] investigated the effect of ball bearing clearance on the dynamic response of a rigid rotor. Elasto-hydrodynamic lubrication (EHL) was introduced into the modelling in the mid-1960s by Wijnat [72] discovering that the effect of the EHL compared to the dry contact situation was moderate for medium loads and low rotational speeds. Fukata [73], Feng [74] (without EHL) and

most recently Sopanen and Mikkola [14, 15] realized different models taking into account the non-linearities, the time variant-characteristics, the EHL and furthermore the effect of localized defects in the inner and outer surfaces.

Concerning the defects modelling, different activities have been conducted in order to extract the main bearing defect frequencies from the simulated signals [15, 16] and also to physically explain the vibration signal signature originating from the passage of a rolling element over a spalled area [75–77]. For this purpose the vibration signal of a localized defect has been described in literature as composed of two main parts: the first originating from the entry of the rolling element into the fault while the second resulting from the exit of the rolling element while it strikes the trailing edge of the fault. The two response signals are separated by a certain time distance called time to impact: this value has been considered as a useful tool to extract the fault size from the measured signal. Nevertheless in the experimental campaign conducted recently by Randall and Sawhali [78] some results obtained at different shaft speeds put in doubt this approach.

In this paper, which is based on a work activity conducted at the Production engineering, Machine design and Automation (PMA) Department of Katholieke Universiteit of Leuven, a deep groove single row ball bearing (SKF 6302) has been modelled as a multibody system using the commercial software LMS Virtual Lab Motion [64] in order to simulate the dynamic behaviour of a bearing inserted in a test set up under construction in the same department.

The bearing model aims to analyze the influence of the operational conditions on the simulated vibration signals using a contact algorithm based on the non linear Hertzian theory (also called elliptical contact conjunction ECC) already implemented in the multibody program utilized. Furthermore the model intends to extract bearing defect frequencies from the simulated signals and to simulate the real vibration signature in case of localized faults. However due to the particular contact algorithm utilized the last objective is not fully reached by the bearing model since the presence of localized discontinuities contributes to move away from the main Hertzian assumptions. In order to overcome this

limitation a different contact algorithm is considered, called polygonal contact method (PCM). This algorithm can be regarded as a compromise between the simple contact approach and the costly FEA: it is more adapt to represent localized physical phenomena even if it requires higher computation time.

For this reason a simplified model is realized trying to simulate the same physical and operational conditions present in the bearing using the PCM algorithm. The paper contributes to knowledge by explaining the vibration signature variations in case of faulty bearing at different shaft speeds. The article is organized as follows: in Section 2 a brief description of the bearing model is presented, explaining the main assumptions and the contact algorithm utilised. Consequently kinematics and dynamics results are compared with the analytical values found in literature. Section 3 reports initially the problematic correlated with the experimental fault size. Afterwards a simplified model is analyzed describing the influence of the shaft speed on the simulated vibration signature in case of localized defects. The paper is concluded in Section 4.

A.2 Deep groove single row ball bearing

A.2.1 Multibody model description and assumptions

A deep groove single row ball bearing (SKF 6302) is modeled as a multibody system using the commercial software LMS Virtual Lab Motion [64] in order to simulate the dynamic behaviour of a bearing inserted in a test set-up realized in the Mechanical Department of Katholieke Universiteit of Leuven. The model aims to analyze the influence of different operational conditions on the vibration signals.

A further objective consists in the extraction of localized defect effects from the vibration signal (main bearing defect frequencies) and in the simulation of the real vibration signature. First of all a short description of the model is necessary. The bearing model is composed of different bodies of well known geometry dimensions as shown in Fig.A.1: outer and inner rings, seven spheres and a shaft. Initially the different bodies are considered rigid in order to obtain

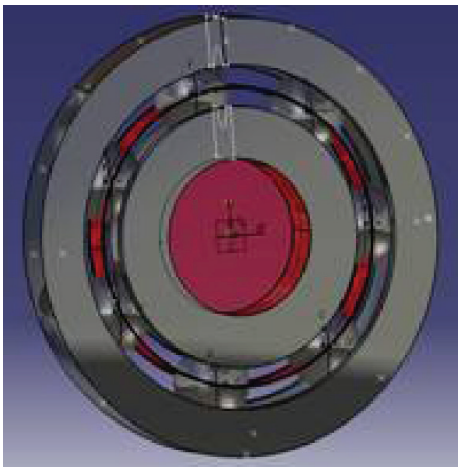

Figure A.1: Deep groove single row ball bearing multibody model

detailed information about the dynamic behaviour of the components at low and medium frequencies. This assumption however limits the correctness of the observations at high frequencies. Therefore, in the future the model will be improved by considering these bodies flexible. Furthermore, the following assumptions are made:

- the contact stiffness between rings and rolling elements is fully determined using the non-linear Hertzian contact deformation theory;

- outer and inner rings, spheres and shaft are rigid. The bending deformation is assumed to be negligible and only local deformation occurs in the contact area;

- the cage is assumed to be ideal as it maintains the balls at a fixed relative distance through distance constrains;

- the movement of the cage is influenced by the slipping occurring between spheres and rings;

- the centrifugal forces acting on the rolling element are negligible;

- the damping caused by the elasto-hydrodynamic lubrication is assumed to be negligible for the considered operational conditions.

The contact stiffness is calculated using the non-linear Hertzian contact deformation theory [79] since the following assumptions are fulfilled:

- the material deforms only elastically;

- the load points normally to the contacting surfaces;

- the dimensions of the contact area are small compared to the radii of curvature of the contacting bodies;

- the deformations of the contacting bodies are small compared to the dimensions of the contact area.

If the roller bearings are running at high speed, the lubrication must be taken into account. This kind of contact is called elasto-hydrodynamic (EHD) contact [72]. Experimentally the lubrication has been found to be important at operating conditions of low load and high speed referred to the nominal operating bearing values: the lubricant behavior in the low pressure zones results in a contact pressure which is significantly different from the one described by the Hertzian theory. In this work the damping caused by EHD contacts is neglected since the simulations are conducted at relatively low speeds.

The different bodies are subjected to several constraints [63] in order to represent the real behaviour of the component inserted in the test setup and to reduce the computation time using some well-advised simplifications as:

- distance contraints between spheres;

- revolute joint between shaft and inner ring;

- bracket joint between outer ring and shaft allowing only $2dof_s$ (axial and vertical motion of the outer ring).

The non-linear Hertzian contact deformation algorithm also called elliptical contact conjunction (ECC) [64, 80] is adopted in the model to represent the contact between spheres and inner/outer rings. This contact tool allows to represent contact and friction forces of the elements rolling around the two raceways through the following inputs:

- geometry (radius of curvatures);

- friction coefficient;

- material properties;

- damping coefficient;

and giving the following outputs:

- the displacements, velocities and accelerations of the different components;

- the resultant forces and torque.

Moreover the contact area is defined as elliptical when the solids are pressed together by a force F considering both the minimum and the maximum curvatures at the point of contact on each body. The contact force expression for the elliptical contact conjunction can be described as follows:

$$F = |\delta|^{1.5} K_{st} \cdot sgn(\delta) \tag{A.1}$$

Where:

$$K_{st} = \frac{\sqrt{K_D}}{\lambda^{1.5} \cdot C_e} \tag{A.2}$$

$$K_D = \frac{1.5}{\frac{1}{R_1} + \frac{1}{R_2} + \frac{1}{R_{1`}} + \frac{1}{R_{2`}}} \tag{A.3}$$

$$\lambda = fz\,(cos(\theta)) \tag{A.4}$$

$$\cos(\theta) = fz\left(K_D, \frac{1}{R_1}, \frac{1}{R_1`}, \frac{1}{R_2}, \frac{1}{R_2`}, \cos(2\phi)\right) \tag{A.5}$$

$$C_e = \frac{1-(\upsilon_1)^2}{E_1} + \frac{1-(\upsilon_2)^2}{E_2} \tag{A.6}$$

And:
$R_1^`$,$R_2^`$ = maximum radius of body curvatures;
R_1,R_2 = minimum radius of body curvatures;
$1/R_1$,$1/R_1^`$=principale curvatures of body 1;
$1/R_2$,$1/R_2^`$=principale curvatures of body 2;
ν_1,ν_2= poisson ratio body 1,2;
ϕ=angle between the plane containing curvature $1/R_1$ in body 1 and the plane containing curvature $1/R_2$ in body 2.

A.2.2 Kinematic validation

Initially the cage speeds obtained from the model is compared with the analytical formulas founded in literature [81]. The cage analytical speed is calculated starting from the assumptions of no-gross slip at the rolling element-raceway contact and considering the velocities as the mean of the inner and outer raceway velocities:

$$\Omega_c = \frac{\Omega_i}{2}(1 - \lambda\cos\alpha) \tag{A.7}$$

In the particular case of the SKF 6302 deep groove ball bearing:

$$\lambda = \frac{d}{D_p} = \frac{7.94}{29.54} = 0.2782 \tag{A.8}$$

Where:
Ω_i=inner ring velocity;

Table A.1: Cage analytical and simulate values

Ω_i [rpm]	Ω_c analytical [rpm]	Ω_c model [rpm]	Differences [%]
994.2	358.8	358.14	-0.1859
1800.7	649.8	648	-0.2854
2504.1	903.7	900.2	-0.3906
3504.7	1264.8	1256.8	-0.6325
4270.5	1541.2	1549.2	0.5191
4971	1794	1800.7	0.3735

Ω_c=cage velocity;
d= ball diameter;
D_p=bearing pitch diameter;
α = contact angle between sphere and raceway [65].

Table A.1 highlights the good correspondence between analytical and simulated cage in case of different inner ring velocities and a radial force of 2000 N applied on the outer ring.

A.2.3 Dynamic validation in case of pure static radial load

After the kinematics validation of the model, the subsequent model analyses are focused on:

- Distribution of internal loading;

- Load zone: effect of clearance and preload;

- Effect of the axial load on the bearing loading and speeds.

The maximum load acting on a sphere during the rotation around the raceways is compared with the analytical formulation of Strijbeck [**?**] as reported in Eqn.A.9 in case of seven rolling elements and 2000 N of radial force applied

on top of the outer ring:

$$Q_{max} = \frac{4,37 \cdot F_r}{Z \cdot \cos\alpha} = \frac{4,37 \cdot 2000N}{7} = 1248N \tag{A.9}$$

where:
Q_{max}=maximum load applied on the sphere;
Z=number of spheres;
F_r=radial force applied on the component;
α=contact angle.
Fig.A.2 represents the simulated load distribution confirming the maximum value found analitically in Eqn.A.9. Furthermore it gives informations about the bearing loaded zone. Theoretically three different possibilities can be evaluated:

- zero clearance;

- postive clearance;

- negative clearance or interference.

The load distribution of Fig.A.2 represents a typical case of no clearance and no preload with a load angle of 96.5 degrees. Different possibilities are taken into account in the model in order to increase the load angle as normally done in practice:

- considering an interference between the inner ring and the shaft (radial preload);

- applying an axial load.

Regarding the interference[81], ball and roller bearings are usually mounted on shafts or in housing with interference fits. Press- or shrink-fitting of the inner ring on the shafts causes the inner ring to expand slightly. Similarly, the press-fitting of the outer ring in the housing causes the former member to shrink slightly. The result is that the bearing's diametral clearance tends

to decrease. Large amounts of interference in the fitting practice can cause the bearing clearance to vanish and even produce negative clearance or interference in the bearing. As result clearance significantly affects ball bearing contact angle. The radial interference is the sum of the radial deflection of each ring due to pressure p as described by Eqn.A.10 :

$$p = \frac{I/D}{\frac{1}{E_1} \cdot \left[\frac{(D_1/D)^2+1}{(D_1/D)^2-1} + \nu_1\right] + \frac{1}{E_2} \cdot \left[\frac{(D_2/D)^2+1}{(D_2/D)^2-1} + \nu_2\right]} \tag{A.10}$$

Where:
p=pressure;
I=diametral interference;
ν_1,ν_2=poisson ratio of body 1,2;
D=common diameter;
D_1,D_2= inside-outside inner and outer diameter;
E_1,E_2= Young modulus of bodies 1,2.
In Fig.A.3 a load distribution in case of a radial load of 2000N and 5 μm interference obtained increasing the inner ring diameter is graphed: the loaded zone increases from 91.5° to 101°.

The simultaneous application of a radial load in the central plane of the rollers and a centric thrust load on a deep groove ball bearing has two main effects [81]:

- variation of the contact angle between spheres and guides of the inner/outer ring and as consequence variation of the velocity of the cage/ spheres;

- variation of the loaded zone.

The application of the combined load on the model allows to reproduce these double effects. Considering an inner ring velocity of 1000 rpm, the axial load application causes a motion of the outer ring in the axial direction (contact angle > 0) increasing the cage speed from 360 rpm to 374 rpm. The results obtained with the model are confirmed analytically, considering a contact angle of 15 degrees. As said before the application of the axial load has the additional effect

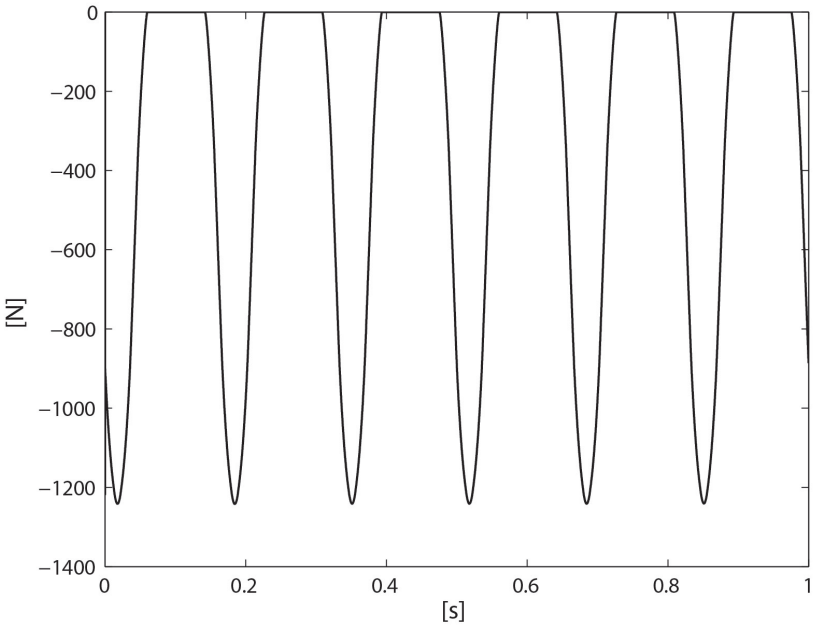

Figure A.2: Load distribution in the contact between sphere-raceway

of increasing significantly the loaded zone passing from a load angle of 91.5° to 156° as shown in Fig.A.4.

Eventually based on the obtained results it can be established that the described multibody bearing model is a powerful tool to represent the kinematics and dynamics behavior of a bearing subjected to different operational conditions.

A.3 Faulty bearing modelling

A.3.1 Simulated bearing defect frequencies

Defects of different sizes are inserted in the multibody model in order to obtain the main bearing defect frequencies and to extract the defect size directly from

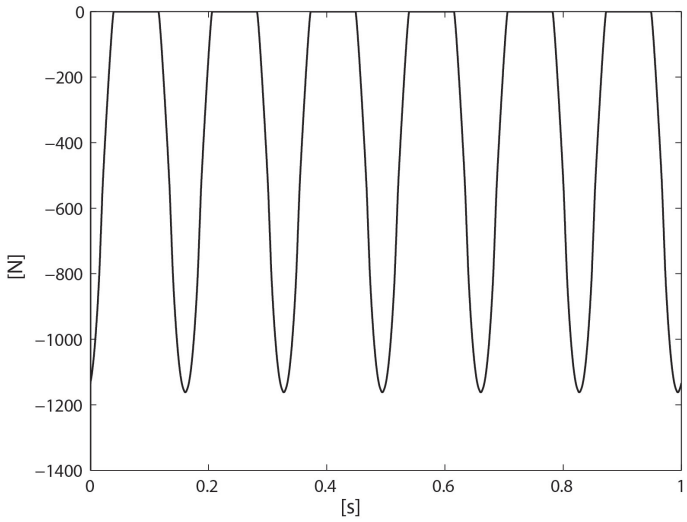

Figure A.3: Load distribution in case of $5\mu m$ of interface

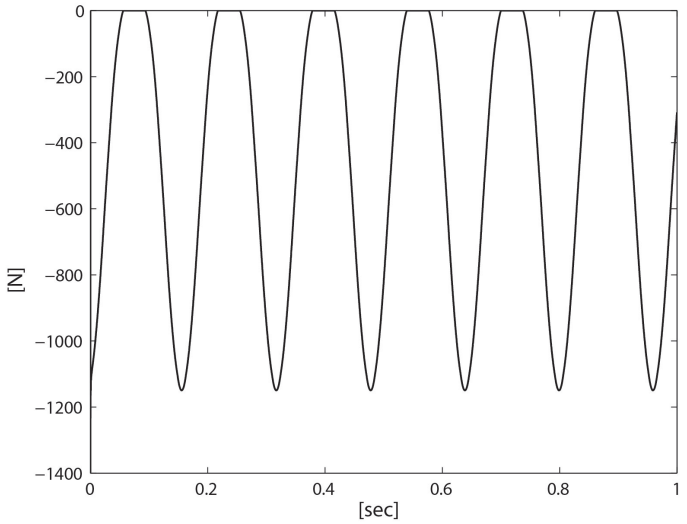

Figure A.4: Load distribution in case of combined radial and axial load(F_r=2000 N ans F_a =800 N)

the information given by the simulated time vibration signal. In this article only the outer ring case study is reported. Bearing non idealities as spall defects are realized in the model through a modification of the race surfaces obtaining a missing contact area of a well known dimension and position. Consequently the time/frequency domain signals are compared with healthy bearing signals, validating the results with the analytical formulations. As reported in literature [69] the bearing signal contains always a contribution due to a particular frequency even in case of no anomalies or irregularities. The frequency is called $Ball\ Pass\ Frequency\ f_e$ and is correlated to the particular dynamic of the components: bearings carry load with discrete elements whose angular position, with respect to the line of action of the load, continuosly changes with time. This mere change of position causes the inner and outer raceways to undergo periodic relative motion even if the bearing is geometrically perfect: this frequency of vibration is therefore equal to the cage rotational frequency multiplied by the number of balls as described in Eqn.A.11:

$$f_e = \frac{z \cdot \Omega_i}{120} (1 - \lambda \cos \alpha) \tag{A.11}$$

The time domain coming from a faulty outer ring presents the same frequency f_e but with higher harmonic contents. Fig.A.5 and Fig.A.6 reports the time and frequency domain signals of the outer ring displacement evaluated in case of healthy component and 1 degree circumferential extension outer ring defect. As clearly visible the characteristic frequency f_e is around 42 Hz in case of inner ring speed of 1000 rpm, seven spheres and λ described by Eqn.A.8.

A.3.2 Spall signal signature

In a number of studies [75–77] the vibration signal originating from the passage of the rolling element over the spalled area has been considered as composed of two parts:

- The first originating from the entry of the rolling element into the fault (destress): step response with mainly low frequency content;

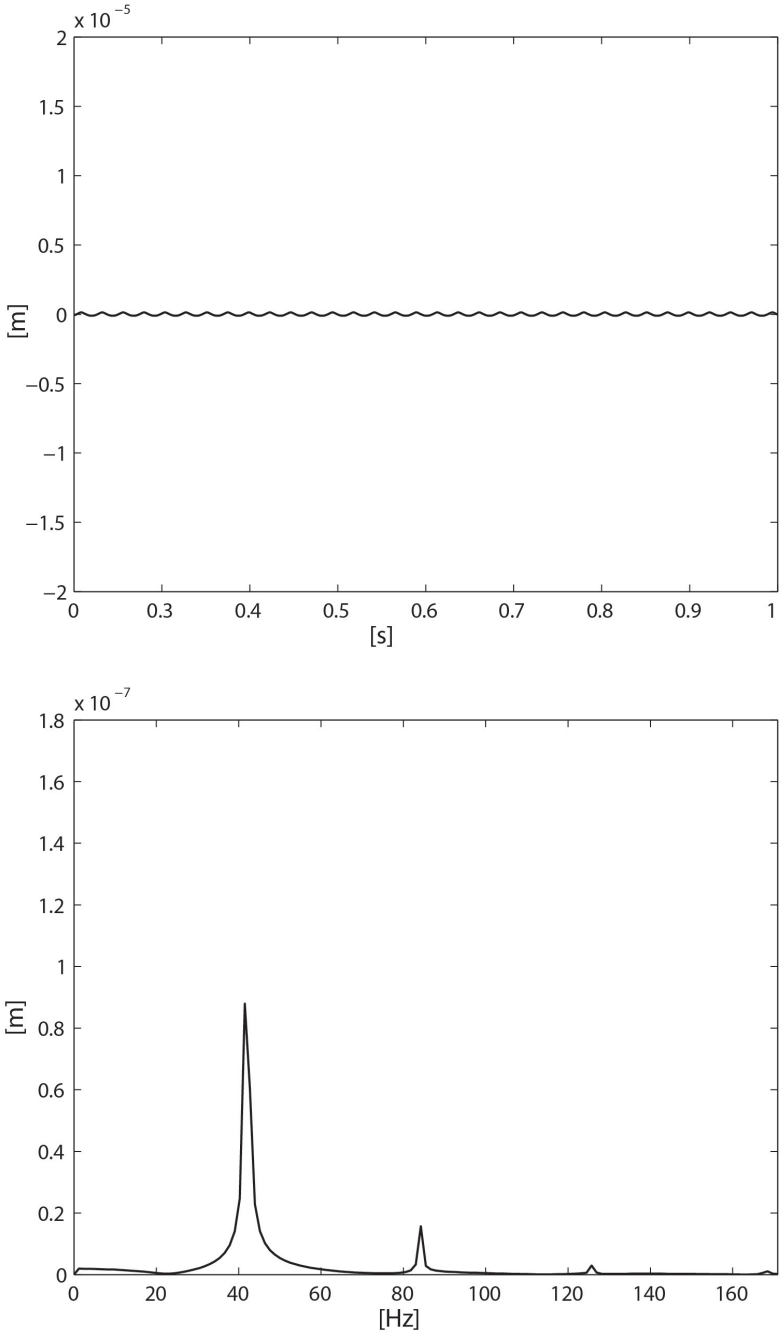

Figure A.5: Time [a] and frequency domain [b] of the outer ring displacement in case of healthy bearing

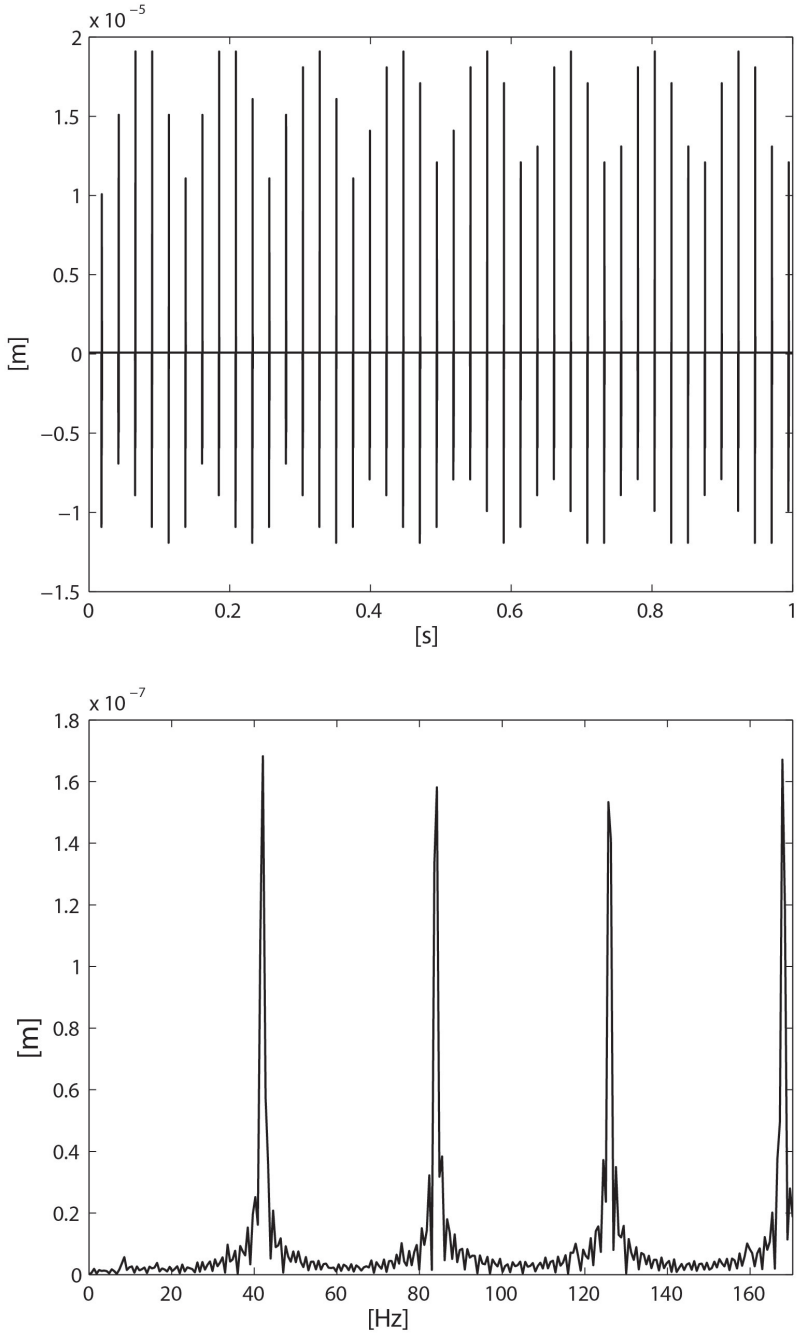

Figure A.6: Time[a] and frequency domain [b] of the outer ring displacement in case of 1° outer ring spall defect

- The second due to the departure of the rolling element from the fault as it strikes the trailing edge of the fault(re-stress): impulse response with a much broader frequency content;

Step and impulse responses have been explained by the travel path of the rolling element. In particular it has been hypothesized that the path of the rolling element bearing centre initially follows a circle of the same radius as the rolling element, thus giving a step change in acceleration. As the rolling element strikes the end of the spall (the center of the ball has moved half way through the spall), the direction of its path changes instantaneously, giving a step change in velocity and thus an impulse in acceleration.

Furthermore the correspondence of the fault size with the separation time has been shown (entry and exit event): an increased fault size means an increased separation time. As consequence the size of the fault can be estimated if the entry and exit event can be successfully extracted from the vibration signal.

A.3.3 Experimental spall size estimation uncertainties

In order to experimentally validate these phenomena Sawhali and Randall [78] conducted an experimental campaign on four self-aligning ball bearing inserted in a fan test rig finding nevertheless some unexpected results: two sizes of inner race faults (0.6 mm ad 1.1 mm) and two sizes of outer race faults (0.6 mm and 1.2 mm) were tested . Hereafter the obtained relationship between the width of the fault $l(mm)$ and the time to impact T_i (samples) is reported with the main assumption that the impact event happens when the centre of the rolling element moves half the spall width. Consequently the averaged time to impact obtained in samples (T_i) is considered as half the actual width of the spall.

More in detail $t(s)$ is defined as the time that the sphere needs to pass the spall of width l_0 on the outer race:

$$t = \frac{l_0}{\pi D_0} \frac{1}{f_c} \tag{A.12}$$

Where:

$$f_c = \frac{f_r}{2}\left(1 - \frac{d}{D_p}\cos(\alpha)\right) \tag{A.13}$$

$$D_0 = D_p + d \tag{A.14}$$

Substituting Eqn.A.13 (considering the load angle α equal to zero) and Eqn.A.14 on Eqn.A.12, time $t(s)$ can be rewritten as:

$$t = \frac{2l_0 D_p}{\pi f_r (D_p^2 - d^2)} \tag{A.15}$$

In case of acquisition sampling rate $fs(Hz)$, the number of samples (sp) during the time t can be expressed as:

$$s_p = \frac{2l_0 D_p f_s}{\pi f_r (D_p^2 - d^2)} \tag{A.16}$$

The spall width (sp) is considered as a function of the time to impact $T_i(samples)$ using the following equality:

$$s_p = 2T_i \tag{A.17}$$

since the impact event has been assumed happening when the centre of the rolling element has moved half the spall width.

Finally substituting Eqn.A.17 into Eqn.A.16 the spall length $l_0(mm)$ is defined as function of the time to impact $T_i(samples)$:

$$l_0 = \frac{T_i \pi f_r (D_p^2 - d^2)}{D_p f_s} \tag{A.18}$$

Where $f_c(Hz)$ is the rotational speed of the cage, $f_r(Hz)$ is the rotational speed of the shaft, f_s is the sampling frequency (Hz), D_0 is the outside diameter (mm), D_p is the pitch diameter (mm) and d is the ball diameter (mm). Table A.2 reports the experimental results obtained by Randall and Sawhali for different spall defect sizes created in the outer rings.

Table A.2: Outer ring size estimation for different speed

Ω_i	CALCULATED SMALL DEFECT	DEVIATION FROM THE NOMINAL SIZE (0.6 mm)
$[rpm]$	$[mm]$	$[\%]$
800	0.5113	-14.78
1200	0.5113	-14.78
1600	0.7389	+23.152
2400	0.6818	+13.33
Ω_i	CALCULATED LARGE DEFECT	DEVIATION FROM THE NOMINAL SIZE (1.2 mm)
$[rpm]$	$[mm]$	$[\%]$
800	1.050	-12.41
1200	1.193	-0.58
1600	1.25	+4.16
2400	1.193	-0.58

These results clearly show that the estimated fault size given by the time to impact information changes considerably increasing the shaft speed as highlighted by the values of the right columns in Table A.2.

A.3.4 Spall modelling

The multibody model described in Section 2 can be only partially useful to simulate the real vibration signal signature originated from the passage of a rolling element over a spalled area due to the ECC algorithm inability of representing the real force exchanged between sphere and raceway in case of localized defects. In particular when the center of the sphere comes on top of the fault incoming edge the force exchanged between the two bodies becomes zero and returns to the original values only when the sphere center goes on top of the trailing edge. This is not what happens in reality. A simple sketch to simplify the description is reported Fig.A.7.

Due to the described ECC algorithm limitation on reproducing the real com-

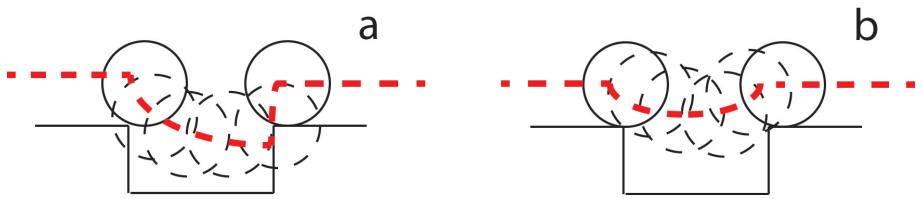

Figure A.7: Sphere trajectory in case of defect: a) Model trajectory using sphere ECC algorithm, b) Real trajectory

ponent behavior in case of localized defect a simple model case is analyzed using a different contact algorithm. Three spheres separated with two distance constrains in contact with a faulty lower fix surface and a upper healthy surface are represented in the Multibody model of Fig.A.7, applying a particular contact technique, called polygonal contact model (PCM), already implemented in Virtual Lab environment [63–66]. This technique is based on the representation of the body surfaces by polygon meshes and contact force determination by the elastic foundation model. The contact is examined using an areal discretisation of the contact patch. It can be regarded as a compromise between the simple contact approach and the costly FEA.

The PCM task consists of three steps. First a collision detection algorithm determines if the contact pair is in touch. If no collision is detected, the program returns zero force and torque and the analysis is finished. Otherwise PCM constructs the intersecting areas of the surfaces and discretises the corresponding contact patches in the second step. Finally the contact force of each contact element is determined and the contact force and torque resulting of all contact elements are calculated.

Two different macro-defect sizes are considered ($5.8mm$ and $1.3mm$) in case of $6mm$ sphere radius. The simplified model is processed at different cage speeds $(0.2m/s, 1m/s, 2m/s, 3m/s, 4m/s)$ and the different sphere center trajectories are reported in Fig.A.9 and Fig.A.10 for both fault sizes. In the Y axis is reported the vertical displacement of the sphere center point while in X axis the horizontal displacement.

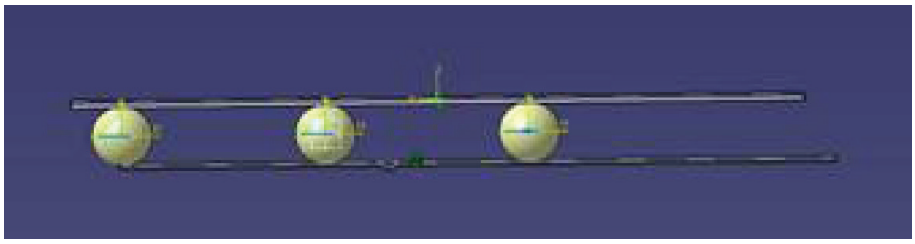

Figure A.8: Simplified sphere-raceway contact model

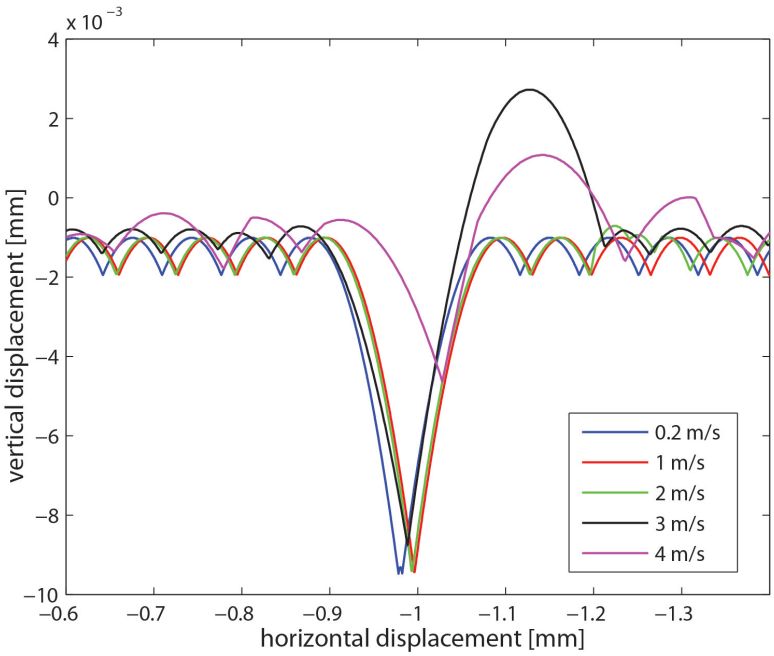

Figure A.9: Comparison of the sphere trajectory for different cage speeds in case of small defect size

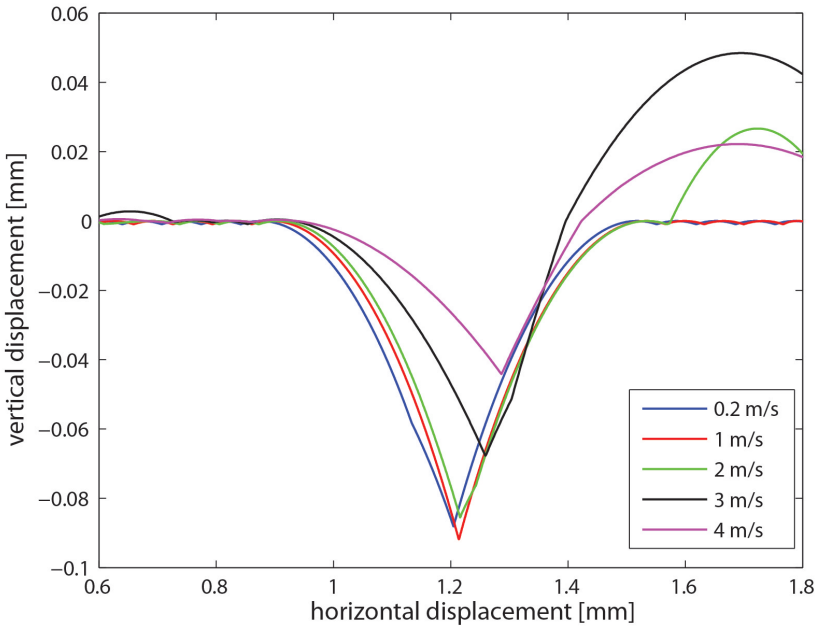

Figure A.10: Comparison of the sphere trajectory for different cage speeds in case of big defect size

Table A.3: Sphere center coordinate of the minimum trajectory point for a small defect

SPHERE SPEED $[m/s]$	DEFECT CENTER $[mm]$	PERCENTAGE (1.004 mm) [%]	DIFFERENCE
0.2	0.9781	-2.5797	
1	0.9965	-0.7470	
2	0.993	-1.0956	
3	0.9885	-1.5438	
4	1.028	+2.3904	

Table A.4: Sphere center coordinate of the minimum trajectory point for a big defect

SPHERE SPEED	DEFECT CENTER	PERCENTAGE DIFFERENCE (1.2095 mm)
$[m/s]$	$[mm]$	$[\%]$
0.2	1.205	-0.3721
1	1.214	+0.3721
2	1.216	+0.5374
3	1.259	+4.0926
4	1.286	+6.3249

The most important information characterizing the sphere motion is the horizontal coordinate that the sphere center assumes in the lowest trajectory point as reported in the Table A.3 and Table A.4 in case of small and big defects respectively. This values represents the sphere center position as the rolling element impacts the spall trailing edge.

It can be noticed that the sphere trajectory changes considerably with the speed variation since the motion path is mostly influenced by the tangential velocity given by the cage. As consequence the time to impact T_i cannot be considered as half the actual width of the spall for every cage speeds: Eqn.A.17 is valid without any modifications only up to a certain shaft speed in which the cage speed allows a trajectory similar to the one predicted theoretically. This threshold value is not simply computable since it is affected by different factors as the bearing type, the operating condition (applied force, lubrication) and the spall size: it can be concluded that the size estimation error increases as the distance of the lowest trajectory point from the spall half width increases.

Eventually it has to be highlighted that the objective of this phase activity is not the numerical comparison of the experimental/simulated percentage divergences in absolute terms since the operational and physical conditions are completely different in the two cases. The focus is rather on the physical

explanation of the divergence causes.

A.3.5 Comparison of different contact algorithms

In conclusion the two contact tools (ECC and PCM algorithms) are compared in the simplified model in order to emphasize advantages and drawbacks of both techniques. Resuming, the PCM algorithm is characterized by the following properties:

- the contact is examined using an areal discretisation of the contact patch;
- a collision detection algorithm determines if the contact pair is in touch;
- the contact force of each contact element is determined using the elastic foundation model [77, 78];
- possibility of measuring the contact between sphere and localized raceway fault;
- - high computation time.

On the contrary in the ECC algorithm:

- the rigid contact bodies are not discretized;
- the contact force is based on the non linear Hertzian theory;
- small computational time.

The strong reduction of the computation time effectiveness prevent the application of the PCM contact algorithm in the complete bearing model making the ECC algorithm the most suitable contact technique avaialable. Applying both techniques on the simplified model as reported in Fig.A.11 it has been found that the ECC algorithm gives the same sphere trajectory of the most accurate contact approach except for the signal phase corresponding the contact between sphere and missing surface. In that case the sphere center follows an unreal

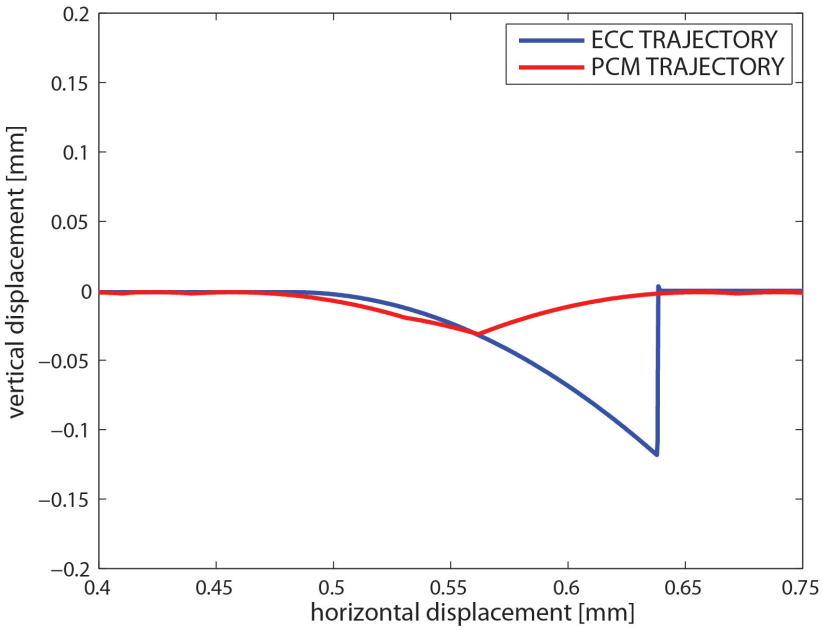

Figure A.11: Comparison of the sphere center trajectory in case of two different contact algorithms

trajectory since the missing contact is recognized only when the sphere center is on top of the incoming/trailing edges. However the ECC algorithm can be considered a powerful and efficient technique to represent the faulty signal since the extracted characteristic defect frequencies depend only on the impulse periodicity and not on the effective sphere trajectory.

A.4 Conclusions

The described multibody bearing model is a powerful tool to represent the kinematic and dynamic behavior of a geometric well-known bearing subjected to different operational conditions. The rigid multibody model is mainly based on the localized contact area deformations neglecting the elasto-hydrodinamic lubrication. Moreover the contact stiffness between rings and rolling elements is fully determined using the non-linear Hertzian contact deformation theory. Furthermore the model is able to simulate the defect frequencies in faulty signals without however reproducing the real sphere trajectory in case of localized defects. At this purpose a different contact algorithm, called polygonal contact method, is considered in order to thoroughly study the effect of spall defect on the vibration signal. The low computation efficiency of this latter technique forced to analyze the sphere trajectory on a simplified model anyhow comparable to the bearing model regarding the operational and constraint characteristics. The obtained results allow to explain the influence of the cage speed on the spall size estimation giving an innovative contribution on bearing diagnostics.

** Appendix A has been extracted from an article presented at ASME2011 International Design Engineering Technical Conferences and Computers and Information in Engineering Conference, August 28-31. 2011 , Washington, DC*
Multibody Modelling of Spalled Rolling Bearings: Effectiveness of Different Contact Algorithms
Technical Publication. DETC2011-48218
Marco Malago', Universita' degli Studi di Ferrara, Ferrara, Italy,
David Moens, Department of Mechanical Engineering - K.U.Leuven, Leuven, Belgium, William Jacobs, Paul Sas, Department of Mechanical Engineering - K.U.Leuven, Heverlee, Belgium

*** This work has been realized through the contribution of the IWT SBO-project no. 090045 Prognostics for optimal Maintenance.*

Acknowledgements

I would like to give a special and sincere thanks to Prof. Ing. Giorgio Dalpiaz, my supervisor, for all his guidance, knowledge, and for the opportunity he gave me. I wish to thank TellureRota S.p.A (Formigine, Modena, Italy) for active co-operation during the course of this research and in particular Dott. Pierluigi Borghi for his great courtesy and helpfulness .

This work has been mainly developed within the Advanced Mechanics Laboratory (MechLav) of Ferrara Technopole, realized through the contribution of Regione Emilia-Romagna - Assessorato Attivita' Produttive, Sviluppo Economico, Piano telematico - POR-FESR 2007-2013, Attivit‡ I.1.1..

I am sincerely thankful to Prof. Dr. Ir. David Moens and. Prof. Dr. Ir. Paul Sas for theirs support during my research period in Leuven (Belgium).

I am deeply grateful to all people I met during last three years and to my Italian and International colleagues who enriched my experience.

Friends, more than colleagues.

Marco,
Ferrara, April 2012.